Modelling of Dual Frequency Capacitively Coupled Plasma Devices.

Paul C. Boyle

September 6, 2004

Modelling of Dual frequency Capacitively Coupled Plasma Devices.

A thesis for the degree of

PHILOSOPHIAE DOCTOR

Presented to

DUBLIN CITY UNIVERSITY

By

PAUL C. BOYLE, B.Sc
School of Physical Sciences
Dublin City University

Research Supervisor:
Prof. Miles M. Turner

September 2004

Declaration

I hereby certify that this material which I now submit for assessment on the programme of study leading to the award of Philosophiae Doctor is entirely my own work and has not been taken from the work of others save and to the extent that such work has been cited and acknowledged within the text of this work.

Paul Boyle.

Signed: Paul C. Boyle, 6th September 2004

Abstract

Dual frequency capacitive discharges are designed to offer independent control of the flux and energy of ions impacting on an object immersed in the plasma. We investigate the operation of dual frequency discharges under a variety of geometries and operating conditions using, firstly, the electrostatic Particle-In-Cell (PIC) simulation method. We show that under certain conditions it is possible to obtain the desired independent control of both the flux and ion energy onto the electrodes. We find thought that within these discharges, the electron heating mechanisms are substantially different than their single frequency counterparts; under certain conditions the electron temperature becomes directly dependent on the voltage amplitude of the lower frequency power source.

An analytical sheath model for a capacitively coupled radio-frequency plasma discharge operated with two frequencies is then proposed and studied under the assumptions of a time-independent, collisionless ion motion. Expressions are obtained for the time average electric potential within the sheath, nonlinear motion of the electron sheath boundary and nonlinear instantaneous sheath voltage. The derived model is valid under the condition that the low frequency (lf) electric field E_{lf} in the sheath is much higher than the high frequency (hf) electric field E_{hf}. This condition is fulfilled within typical dual frequency conditions. It is shown, however, that the hf electric field modifies the sheath structure significantly as a result of the electron response to E_{hf}. This model has been compared to particle-in-cell plasma simulations, finding good quantitative agreement. We present the dependence of the maximum sheath width and the dc sheath voltage drop on the hf/lf current ratio and on the hf/lf frequency ratio.

Subsequently, this analytical model is modified to describe the collisional ion dynamics within the sheath at higher more realistic pressure regimes. To describe the different ion dynamics, we have used a variable mobility model for the ion motion through the sheath. The sheath dynamics and characteristics of the collisionless and collisional models are then compared finding significant differences between the two models.

A two dimensional PIC code is then developed to study the effect of operating plasma devices at greater frequencies than the normal industrial standard of 13.56 MHz. This PIC code is an Electromagnetic variant, meaning that the full set of Maxwells equations are solved for the fields, rather than simply Poissons equation. Using this PIC code it is found that the radial plasma density profile is increased significantly as the operating frequency is increased. This results in a greater uniformity of the ion bombardment profile onto the electrode.

Contents

List of Figures

continued from previous page

n	Particle number density (m^{-3}); n_e electron density; n_i Ion density; n_g Neutral gas density
P	Power (W)
p	Pressure (Torr)
q	Electric charge (C)
s	Sheath position (m)
t	Time (s)
T	Temperature (K or Volts)
u	Velocity (ms^{-1}); Average velocity; u_B Bohm velocity
v	Velocity (ms^{-1})
V	Electric potential (V)
$\mathcal{W}$	Super-particle weighting factor
x	Rectangular coordinate
Γ	Particle flux ($\mathrm{m}^{-2}\mathrm{s}^{-1}$)
Δ	Δt PIC timestep; Δx PIC cell size
ϵ_0	Vacuum permittivity ($\simeq 8.8 \times 10^{-12}$ Fm^{-1})
μ_0	Vacuum permeability ($4\ \pi\ 10^{-7}$ Hm^{-1})
λ	Mean free path (m); λ_i ion mean free path; λ_D electron Debye length (m)
ν	Collision frequency (Hz)
ρ	Charge density (Cm^{-3})
σ	Cross section (m^{-2}); Surface Charge Density (Cm^{-2})
Φ	Potential (V)
ω	Angular frequency (rad s^{-1}); ω_{pe} Electron plasma frequency; ω_{pi} Ion plasma frequency

continued on next page

continued from previous page

α	Frequency ratio
β	Current ratio
η	Power loss mechanism
ϕ	Phase
r	ADI time step
Ψ	Field vector

CHAPTER 1

Introduction

It is often quoted that 99% of the universe exists within a plasma state. This comment, although quite flattering to plasma physics in general, has the advantage for plasma physicist of being rather difficult to disprove. It should be noted though the prevalence of the plasma state and also the extreme importance plasma has within modern technology. Indeed, much of the technology that we now take for granted would not be possible without the use of the plasma state in one form or other [2, 3].

Plasma has become vital within many of the largest industries in the world, of particular importance is their use within the electronics and computer industries. Within these industries, plasmas are used, for example, in the surface treatment of silicon wafers; which is necessary for the manufacturing of integrated circuits.

1.1 Basic Theory

A Plasma can be defined as a quasi-neutral partially ionised gas in which the ions and electrons exhibit collective behaviour and was first identified in the nineteen twenties [4–6]. In a simple plasma there exists two types of charged particles, negatively charged electrons and positively charged ions. The densities of these particle species are on average equal, resulting in the plasma being in electrical quasi-neutrality. The types of plasmas which can exist vary enormously, from the plasmas in the Earth's ionosphere, having densities in the order of $\approx 10^{12}\ m^{-3}$ and temperatures of the order $\approx 10^{-2}\ eV$, to fusion plasmas, having densities of $\approx 10^{20}\ m^{-3}$ and temperatures of $\approx 10^{3}\ eV$. Although, the type of plasmas that are of interest here have densities approximately between these ranges and temperatures of a few eV.

In our definition of a plasma we said that the particles exhibit collective behaviour, although the behaviour of each of the particle species varies significantly. This is largely a result of each of the particle species within the plasma having its own plasma frequency, given by

$$\omega_{p(i,e)}^{2} = \frac{n_{i,e}e^{2}}{\epsilon_{o}m_{e,i}}, \tag{1.1}$$

where the subscripts e and i refer to electrons and ions respectively. The plasma frequency is possibly the single most important parameter for plasmas, with the possible exception of the particle charge, and simply determines how rapidly the particles can respond collectively to applied forces. For the range of densities of interest within glow discharges, the electron plasma frequency is normally within the gigahertz range, or at least substantially greater than the frequency of any externally applied force. The electrons can therefore be considered to respond instantaneously to the Electromagnetic fields within the plasma. The ion plasma frequency on the other hand is normally in the low MHz range making their response to the fields quite complicated at times.

Due to the low mass and high mobility of the electrons compared to the ions, the velocity of the electrons, u_e, is very much greater than that of the ions, u_i. Hence the flux of the electrons, Γ_e, is also very much greater than the ion flux, Γ_i. If an electrically isolated substrate is now introduced into the plasma, there will be an excess electron flux onto the substrate. This substrate will then immediately start to build a negative charge. As this negative charge increases, the substrate will begin to attract positive ions and repel electrons. As a consequence of this the ion flux onto the substrate is increased and the electron flux decreases; this continues until a state of equilibrium is achieved, that is $\Gamma_e = \Gamma_i$. The negative charge that has built up on the substrate and the space charge that develops in the vicinity of it produces an electric field. The potential of this field is referred to as the sheath potential, V_s [7].

The structure of the plasma sheath profile within a plasma device is shown in figure 1.1, where So is the position of the sheath - plasma interface, n_e and n_i are the electron and ion densities respectively. The sheath potential is just the solution of Poisson's equation, with appropriate boundary conditions, over the sheath region. From this the Electric field throughout the sheath is given by,

$$E(x,t) = \begin{cases} \frac{en-s(t)}{\epsilon_o} & \text{for} \quad x \geq s(t) \\ 0 & \text{otherwise} \end{cases} . \tag{1.2}$$

To a first order approximation the Electric field through the sheath can be assumed to vary linearly from the substrate to the maximum sheath extent.

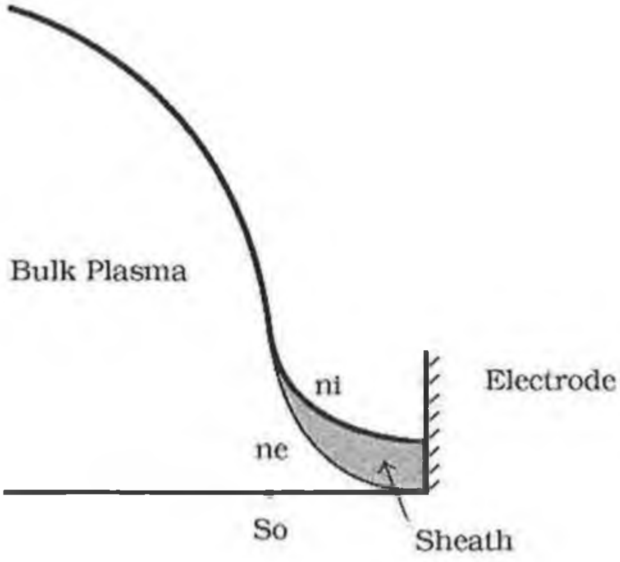

Figure 1.1: Density profile showing the plasma sheath interface

1.2 RF Discharges

Rf plasmas are far from being in thermodynamic equilibrium, the three major particle, ions, electrons and neutral gas particle all having different temperatures [8]. The electrons have temperatures of $2 \rightarrow 5\ eV$, the ions, $0.025 \rightarrow 0.2\ eV$ and the neutral gas is normally on the order of room temperature. Radio frequency discharges are normally operated at gas pressure ranges varying from milliTorr to Torr pressures. At these pressures the charged particle densities are in the order of $10^{15} - 10^{17}\ m^{-3}$. In plasma devices that are used in the semiconductor industry the plasma is confined in a chamber and energy is supplied to it through an external source. In the system described here, the power is supplied to a metal planar substrate in the form of an *rf* voltage or current source. These are referred to as Capacitive (or E-type) discharges. The background gas can be any of a large range of gases depending on the process for which the plasma is being used. For reasons explained later, all the results which are presented here are obtained for plasmas in which the background gas is pure argon.

A simple diagram of an *rf* plasma device is shown in figure 1.2, taken from [9]. The power is supplied by applying either a voltage or current wave form onto one of the electrodes, whereas the other electrode is grounded. Typical voltages applied to the electrode range from hundreds to several thousands of volts, whereas the frequency is in the MHz range, where $13.56\ MHz$ is the most commonly used industrial standard. This particular frequency being allocated by international convention for industrial use.

Within *rf* discharges the sheath cyclicly expands and contracts on both electrodes. The expansion and contraction of the sheath on the electrodes have a phase difference of π between them, this means that when one sheath is fully expanded, the other sheath is collapsed. Normally the electric potential that exists across the sheath is great enough to repel all the but the most energetic electrons. However for a brief period within the *rf* cycle, the potential decreases sufficiently to enable a large electron current to flow to the electrode. This is necessary in order to maintain an equal ion and electron current onto the electrode over the entire *rf* cycle, since there is a near continuous ion current onto the electrode.

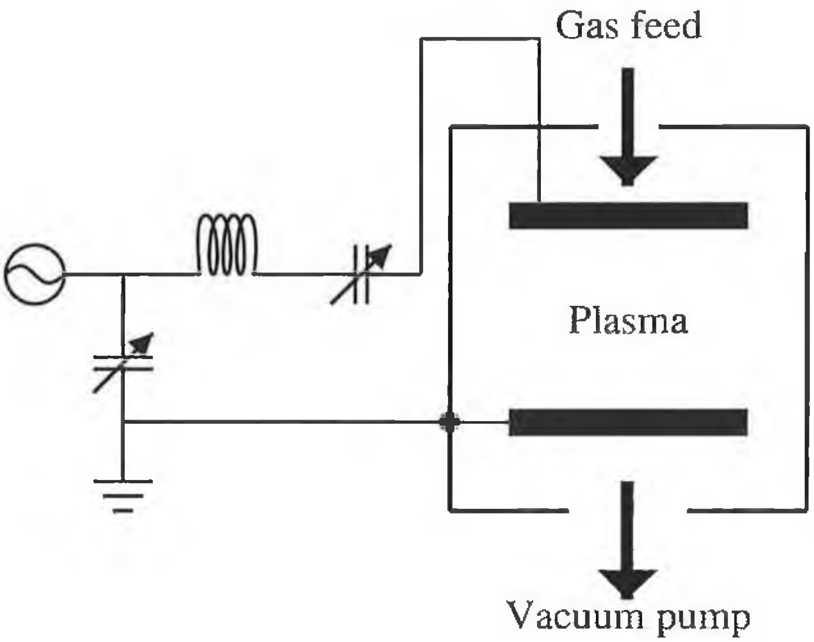

Figure 1.2: A simple schematic of a capacitive *rf* discharge

1.3 Why Dual frequencies Plasma discharges

Capacitively coupled radio-frequency (rf) plasma discharges operated at the traditional industrial frequency of 13.56 MHz have been used extensively within the micro-electronics industry for decades [10, 11]. Within these devices, the ion flux and the ion energy are known to play an important role for material processing applications such as thin film etching, deposition, sputtering and other surface treatments [12]. In order to improve the controllability of both ion flux and ion energy in semiconductor processing, dual frequency excitation plasma have been developed in recent years [13–19], dual frequency power sources also more recently been used in inductively coupled devices [20]. However, to date, very few fundamental investigations on these devices have been performed. In particular, the important sheath dynamics within this dual frequency configuration have been ignored. At low pressure, the ion flux J_i onto the substrate can be expressed, in principle, as

$$J_i = e n_o u_b, \tag{1.3}$$

where e, n_o and u_b are the elementary electronic charge, the plasma density at the plasma sheath boundary and the Bohm velocity [21–24] respectively. In low pressure *rf* discharges, the energy of the ions bombarding the substrate electrode is determined predominately by the time averaged sheath voltage. At the substrate surface, the sheath voltage is the difference between the time averaged plasma potential and the dc bias on the electrode. Thus, the mean energy of the ions bombarding the substrate surface is approximately given by

$$E_i = e(V_p - V_{dc}), \tag{1.4}$$

where V_p and V_{dc} are the time averaged plasma potential and the dc-bias. At higher pressures, the ion energy may be significantly lower than the sheath voltage. This is a result of ions losing some of their energy through collisions as they traverse the sheath. Even in this case, their mean energy can be controlled by the sheath voltage. Therefore, if the plasma density and sheath voltage can be controlled independently then both the ion flux and energy may be controlled independently of each other. The effect of varying frequency in single frequency devices is explained in detail elsewhere [25–29].

However, a drawback of conventional single frequency reactors is that the plasma density and ion bombardment energy can't be adjusted independently, because a variation in the frequency leads to a change in both sheath voltage and plasma density [30]. To obtain an additional degree of flexibility, capacitively coupled radio-frequency plasma discharges driven by a current oscillating at two different frequencies [31] have been proposed and operated. To a reasonable approximation the high frequency current controls the plasma density while the second lower frequency controls the discharge voltage, and consequently the peak ion bombardment energy.

1.4 Modelling of Plasma's

The kinetic Boltzmann equation is given by the following

$$\frac{\partial \mathfrak{F}}{\partial t} + v\frac{\partial \mathfrak{F}}{\partial x} + F\frac{\partial \mathfrak{F}}{\partial v} = \frac{\partial \mathfrak{F}}{\partial t}|_{c}, \tag{1.5}$$

where $\mathfrak{F}$ is a distribution function, F represents a force given by the Lorentz equation and the right hand side represents a collision operator. In principle the above equation completely describes a plasma, given appropriate boundary conditions. This first order differential equation is deceptively simple though, as $\mathfrak{F}$ can represent an arbitrary distribution function. Also, the force acting on the particles depends directly on the their velocity distribution function, $\mathfrak{F}$. This coupling between the particle dynamics and the forces results in equation 1.5 being horribly difficult to integrate and solve. The collision operator on the rhs or the equation also represents problems, since the exact form of the collision operator is in general not well known. An exact solution of the above equation would therefore require the solution of a full N body problem. Since the particle density within a plasma is of the order of $10^{15} \rightarrow 10^{18}$ this is a hopelessly impossible task.

Since it is impossible to solve the full N body problem, we are left with the necessity of simplifying the Boltzmann equation [32]; it is possible though to solve the Boltzmann equation directly under some conditions, see for example [33]. One possible approach to achieving this is to replace the arbitrary distribution function with a known distribution function, such as a Maxwellian or Druyvestian distribution function. This has the effect of changing the Boltzmann equation into a fluid equation. By this we mean that we loose the detailed kinetic information about the plasma. Then multiplying over increasing powers of the velocity and integrating the distribution function, it is possible to obtain moments of the Boltzmann equations, the first few of which are reproduced here.

$$\frac{\partial n}{\partial t} + \frac{\partial nu}{\partial x} = 0, \tag{1.6}$$

$$m\frac{\partial nu}{\partial t} + \frac{\partial}{\partial x}(nT + mnu^2) + Fn = 0. \tag{1.7}$$

These give equations for the particle density and particle flux respectively. An inspection of the above equations show that they have the form of conservation equations. The first being an equation for particle conservation and the second being the conservation equation for particle flux.

There are two significant problems in modelling a plasma in this way. The first of these problems is that the moments of the Boltzmann equation do not in themselves form a closed system of equations. Each equation depends on the next equation, found by integrating over a higher power of the velocity distribution function. For example, (1.6) gives an equation for the particle density, which is itself dependent on the particle flux, given by a separate equation. The moments of the Boltzmann equation always represents a system of N equations with $N+1$ unknowns. A method of closing the system of equations must therefore be found. However any method that is used to close the system of equations may in itself neglect some important physics. The second problem with modelling a plasma in this way, is that in a real plasma the velocity distribution function may vary significantly in space time and usually can not be accurately described by a simple distribution function, such as a Maxwellian. It can therefore be unrealistic to assume a known distribution.

What is required to realistically model plasmas is therefore an efficient method of solving the Boltzmann equation or an equivalent thereof. Luckily there is a method available which can achieve this. This is normally called the particle in cell (PIC) with Monte Carlo collisions (MCC) algorithm method [34–39]. Though this method has been available for decades it is only within the last decade or so that it has become widely used as a result of the vastly increasing computing power in recent times. Although there is a detailed description of an electromagnetic PIC in Chapter 5, a brief outline is presented here of the general algorithm.

The particle in cell method is based on a purely kinetic representation of the electron and ion particles within a plasma. It is equivalent to solving the Boltzmann equation through first principle methods and the fields are determined directly from the particle kinetics. PIC simulations vary greatly in their application and their complexity. They can be either one, two or full three dimensional simulations in a variety of geometries applied to different type of devices. Under some PIC's the fields are solved simply through the uses of Poisson's equation or they may involve the solution of the full set of Maxwell's equations.

The basic principle is to reduce the near infinite number of real particles within a plasma with a finite number of super particles. Each one of these super particles represents on the order of $10^4 \rightarrow 10^6$ real particles, with all physical values scaled appropriatly. The area between the electrodes is then divided up into a spatial grid. Initially the super particles are distributed randomly throughout this spatial grid. Within each spatial grid cell the total number of charged particles is determined and a charge is assigned to that cell representing the total charged particles within that cell; within Electromagnetic PIC's, it is also necessary to obtain the current at each cell point. Once the charge densities and current densities are known throughout the spatial grid, it is possible to obtain the electric and magnetic fields throughout the spatial grid.

Once the fields are known throughout the spatial grid it is necessary to include particles dynamics. This is obtained by using Newton's second law in its finite differenced form. The following equation is then solved to obtain the new velocity resulting from a given force,

$$F = ma \rightarrow m\frac{v_1 - v_0}{\Delta t}. \tag{1.8}$$

Where Δt is the time step, v is the particle velocity and the subscripts refer to the old and new values of the velocity. The force term on the lhs of the above equation is found from the solution of the finite differenced Lorentz equation. The particles are then moved into different spatial cells depending on their velocities. After moving the particles it may be desirable for the particles to experience collisions depending on their velocity and the density of particles and the collision cross sections. This is handled though the MCC algorithm after each time the particles are moved. The entire algorithm is then as is depicted in figure 1.3. This algorithm is then iterated forward in time until a steady state solution is obtained.

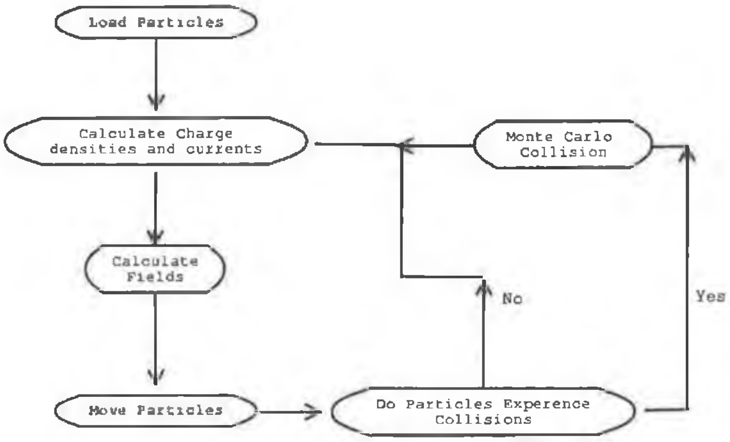

Figure 1.3: Basic PIC-MCC algorithm

For the work presented in this thesis, two different particle codes were used, a one dimensional electrostatic PIC code and a two dimensional Electromagnetic code.[1]

1.5 Thesis layout

The layout of this thesis is as follows. In Chapter 2 the general characteristics of dual frequency discharges are presented. This includes Electrostatic PIC simulations of dual frequency discharges and also a simple analytical model is presented which can explain many of the characteristics found in

---

[1] The Electrostatic PIC code used here was written by M. M. Turner, the Electromagnetic code was written by the Author.

these devices. In Chapter 3 an analytical sheath model is presented and compared to Electrostatic PIC simulations. This model is found to accurately describe the sheath characteristics of dual frequency plasma sheaths under many conditions. This model is then generalised for the situation in which the ion dynamics through the sheath are collisional in Chapter 4, which is more representative of a real plasma. In Chapter 5 we then describe the implementation of an electromagnetic particle-in-cell simulation. Using this electromagnetic PIC simulation we then investigate the validity of simulating a plasma by the assumption of the field being produced only by Poisson's equation and not the full solution of Maxwell's equations in Chapter 6. Finally in Chapter 7 we present our conclusions.

CHAPTER 2

Electrostatic dual frequency discharges

In this chapter we present the characteristics of dual frequency discharges under several different geometries and operating conditions. Methods of controlling the ion energy bombarding the electrodes and the ion current onto the electrodes are presented and discussed. It is found that there are two separate methods of obtaining this independence, depending on the geometry and operating conditions of the device. When the a device is operated with two separate frequencies, it is found that the electron temperature becomes dependent on the low frequency power source under certain important conditions. We then discuss the effect operating a device with two separate frequencies has on the shape of the ion energy distribution function, (IDF), at the electrodes . It is found that under certain conditions the IDF resembles the bimodal structure which is well known from single frequency devices [40]. We then present an analytical global model of dual frequency device which can be used to explain many of the characteristics observed in dual frequency capacitively coupled discharges. Finally we discuss limits on the frequency ratios which are necessary to obtain independent control of both the ion energy and flux.

2.1 General characteristics

In this section we present the general characteristics of dual frequency capacitive discharges for three different operating conditions where the discharge is driven with a voltage signal, a current signal and a constant high frequency power source respectively [41]. We show that it is in general not possible to obtain complete independence of the current and flux onto the electrodes. This independence is only possible within a small range of parameter space. All the results presented in this chapter were obtained through the use of the 1-d electrostatic particle-in-cell method.

2.1.1 Symmetric discharges

In figure 2.1 we show the plasma density, sheath width and ion flux onto the electrodes in a symmetric dual frequency discharge. The high frequency power is supplied through a sinusoidal voltage source whose amplitude is held constant at 100 V and at a frequency of 100 MHz. The second lower frequency is then driven at 1 MHz in which the power is supplied through a variable amplitude voltage source. Both power sources are supplied to the same electrode, whereas the second electrode is grounded. The total waveform supplied to the powered electrode then has the form $V_T(t) = V_{lf}\sin(\omega_{lf}t) + V_{hf}\sin(\omega_{hf}t)$. Where the subscripts hf and lf refer to the high and low frequencies respectively. The separation between the electrodes is

3 *cm* and the background pressure is held constant and uniform at 10 $mTorr$.

As can be seen there is no phase difference between the operating frequencies. It was found the found the the characteristics of the plasma is independent of the phase of each frequency.

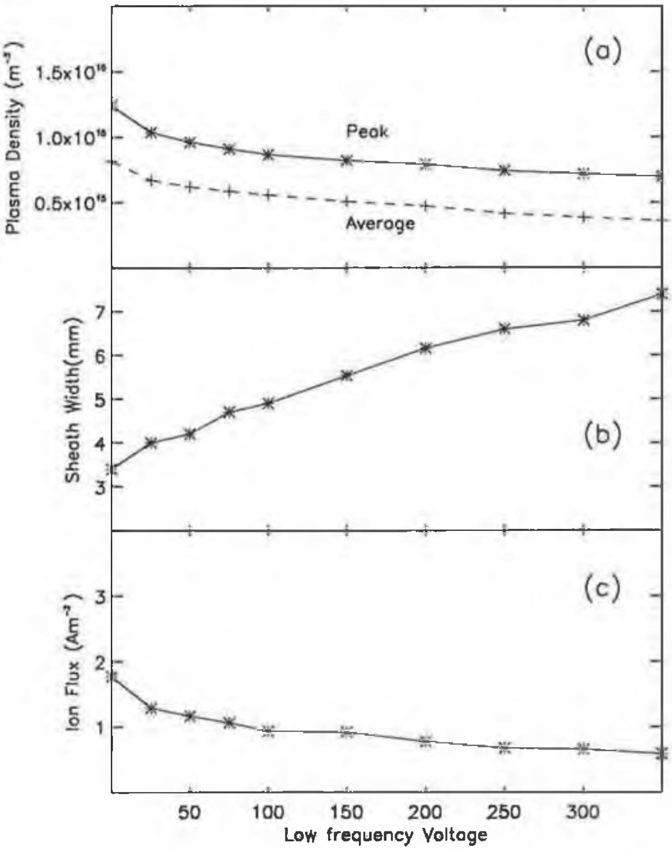

Figure 2.1: General plasma parameters for a dual frequency symmetric plasma discharge. ω_{hf} is driven with a constant voltage source, whose amplitude is 100 V. ω_{lf} is then driven with a variable amplitude voltage source. Electrode separation is 3 *cm* and background pressure is 10 $mTorr$

In figure 2.1(a) the plasma density spatially averaged over the plasma extent and the peak plasma density are plotted as functions of V_{lf}. The plasma density is observed to decrease continuously as V_{lf} is increased; the density decreases by approximately 60% as V_{lf} is increased from 0 through to 350 V. This occurs because, although the voltage is increasing, the discharge current decreases as is seen in figure 2.2. The decreases in the hf current can be attributed to the increase in the lf voltage. The increasing lf voltage results in the size of the sheath increasing and therefore the sheath capacitance decreases. Thus, at fixed hf voltage the hf current should decrease. The net result of this decrease in hf current is that the plasma density decreases as a result of the following mechanism. Under the conditions which are being simulated here, ionization is virtually entirely due to electron neutral collisions; ionization due to ions neutral collisions and other processes is negligible. Therefore, the plasma density is due exclusively to the electron ionization rate which is proportional to the ohmic power supplied to the electrons. The electron ohmic power is then given by

$$S_{omh} = \frac{1}{2} J^2 \frac{1}{\sigma_{dc}}, \tag{2.1}$$

Where σ_{dc} is the dc plasma conductivity. Thus, the reduction in the discharge current results in the decreased plasma density observed in figure 2.1(a). Therefore even at fixed power, these variations yield a decreased peak and average plasma density as the low frequency voltage increases. The above equation is for the ohmic power deposition only and neglects the power deposited by collisionless heating [42–44], however the argument remains the same as the current squared remains the dominant term; variation in J^2 is significantly greater than the variation in σ, which is itself a function of density.

In figure 2.1(b) we show the variation in the sheath width as a function of V_{lf}, where the sheath width is defined as the point at which time averaged

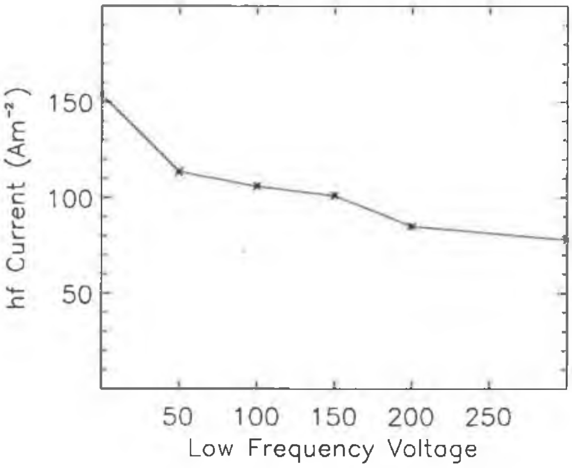

Figure 2.2: High frequency discharge current as a function of the low frequency voltage. Conditions are the same as those in figure 2.1.

quasi-neutrality is violated, that is

$$\frac{n_i - n_e}{n_i} > 0.02. \tag{2.2}$$

It is observed that the sheath width increases considerably. The width of the sheath increases from approximately $3 mm$ through to approximately $8\ mm$ when V_{lf} is increased from 0 to 350 V respectively. This increase in the sheath width is a direct result of the application of the second voltage source, resulting in an increased total voltage, the discharge voltage being simply the integral over the charge density in the sheath. Therefore, in order to support an increased voltage the sheath width must increase. Similar characteristics in the width of the sheath were observed in a dual frequency device which was studied experimentally by Kitajima *et al.* [13, 14]. Under conditions where the high and low frequency power sources were supplied to separate electrodes, it was observed that the sheath width on the electrode powered with the low frequency power source increased as V_{lf} was increased. In their device, the widths of the sheaths on the two electrodes were different. As the device which is being simulated in figure 2.1 is symmetric with power supplied to only one electrode, the width of the sheath on both the powered and grounded electrodes are equal. Similar characteristics of the sheath width have been predicted theoretically [16].

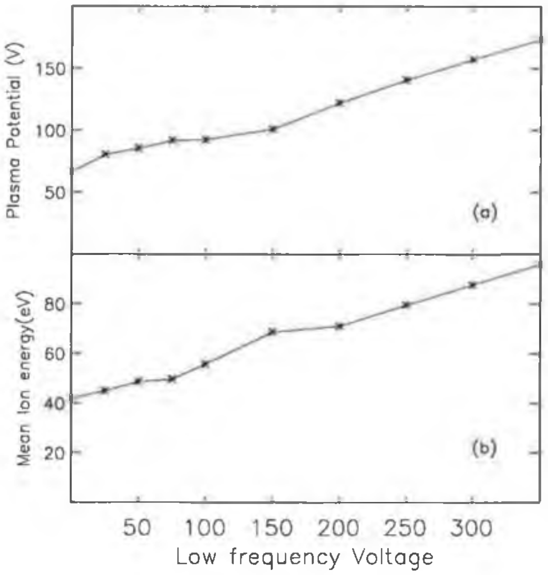

Figure 2.3: Plasma potential and mean energy of ions bombarding the electrodes for dual frequency discharge. Conditions as in figure 2.1.

In figure 2.1(c), the dependence of the ion current bombarding the electrodes, Γ_i, with respect to V_{lf} is shown. The dependence of the ion flux is similar to that of the plasma density, Γ_i decreases initially as V_{lf} is increased and then becomes approximately independent of V_{lf}. This is to be expected because of equation (1.3), which states that the ion flux onto the electrodes is proportional to the plasma density. Since the device which is being simulated is symmetric, the ion flux onto both the powered and grounded electrodes are equal.

We now examine the dependence of the potential within the given device. Shown in figure 2.3(a) is the dependence of the plasma potential on V_{lf}. It is observed that the plasma potential increases linearly as V_{lf} is increased. The plasma potential increases by approximately a factor of 3 as V_{lf} is increased from 0 to 350 V. The mean ion energy bombarding the electrodes for a collisionless sheath is then related to the time averaged voltage by

$$E_i = \bar{V_s} + \frac{1}{2}T_e. \tag{2.3}$$

Where $\bar{V_s}$ and T_e are the time averaged sheath voltage and the electron temperature expressed in electron volts respectively. The $\frac{1}{2}T_e$ term represents the energy that the ions have as they cross the Bohm point and enter the sheath. In collisional sheaths, the above equation is no longer valid, although the mean ion energy remains proportional to the sheath voltage. As the plasma potential increases linearly with respect to V_{lf}, so too does the mean ion energy at the electrodes increase linearly with respect to V_{lf}, as shown in figure 2.3(b), although, the mean ion energy does not increase as rapidly with respect to V_{lf} as the plasma potential does. The mean ion energy increases by a factor of two when V_{lf} is increased from 0 to 350 V, whereas the plasma potential increases by a factor of 3 over the same voltage range. This is believed to occur as a result of the increase in the sheath width, figure 2.1(b). When the sheath width increases, the ions must travel a greater distance to reach the electrodes and therefore experience a greater number of collisions as they traverse the sheath. This results in the ions losing a greater proportion of their energy as they traverse the sheath.

By comparing figure 2.1 and figure 2.3 it is evident that for a fixed high frequency voltage, and under the parameter regime that is considered here, it is not possible to obtain independence of both the ion energy and flux onto the electrodes. It is also evident that there is a strong coupling between the two operating frequencies. It should be noted, that a high frequency voltage source is not the usual control parameter in dual frequency plasma devices.

2.1.2 Symmetric current driven discharges

In the previous section we presented data in which the discharge was driven with a voltage source. When this was performed, the discharge current was observed to decrease as V_{lf} was increased. Since the ohmic electron power deposition is $\propto J^2$, see equation 2.1, this results in the plasma density decreasing as V_{lf} is increased. Therefore if one wishes to maintain a constant plasma density, and a constant ion current which results from it, the device should be operated under conditions where the discharge current is held constant. In a dual frequency plasma discharge the current is a combination of both high and low frequency components.

In figure 2.4(a), the peak and spatially averaged plasma densities are shown. It is found that the average plasma density is approximately independent of V_{lf}, although the peak plasma density increases slightly. This is compared to an approximately 60% drop in the plasma density over the same voltage range as in figure 2.1. This shows that if the total current is held constant, then the plasma density remains approximately constant. This is as expected, since the ionization rate is predominately dependent on the discharge current.

The dependence of the ion current onto the electrodes is shown in figure 2.4(b). The ion current is observed to be approximately independent of V_{lf} also. This is a direct result of the plasma density being independent of V_{lf}. This shows that when the discharge is driven with a constant current, the low frequency power source can then be manipulated independently of

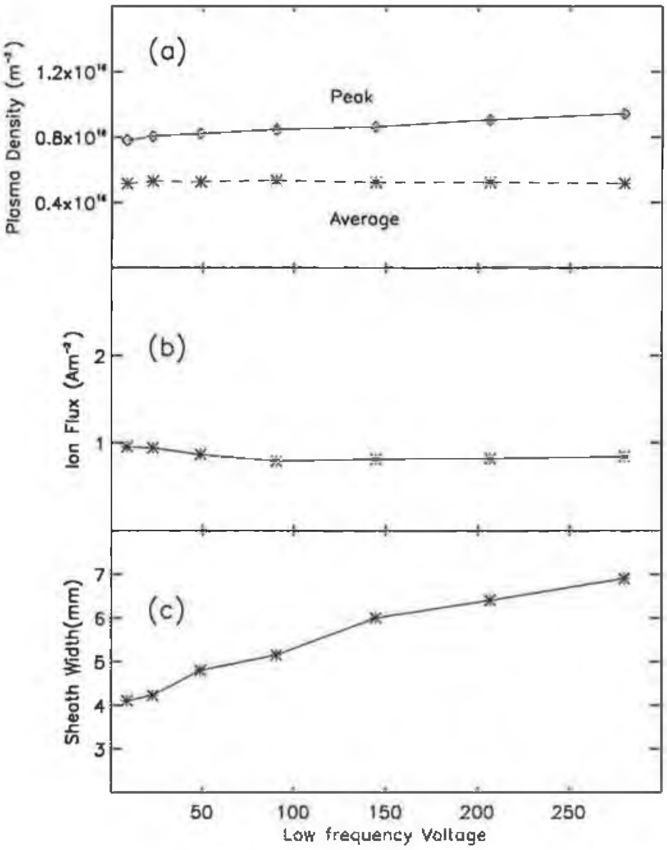

Figure 2.4: General plasma parameters for a symmetric discharge driven with constant total current of 100 Am^{-2}. All other parameters as in figure 2.1.

the ion current.

The characteristics of the sheath are shown in 2.4(c), the dependence of the sheath width is similar to that of a voltage driven discharge, see 2.1(c). The sheath width is observed to increase approximately linearly with increasing V_{lf}. The sheath width again increases from 4 *mm* to approximately 7 *mm* over the *lf* voltage range from 0 to 300 *V* respectively.

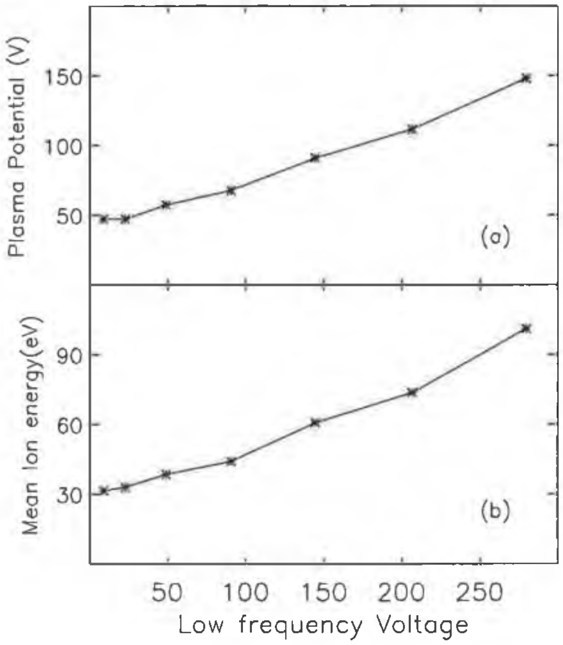

Figure 2.5: Plasma potential and mean ion energy for discharge driven with a constant total current, situation is the same as that depicted in figure 2.4.

We now present the dependence of the plasma potential as a function of V_{lf}, see figure 2.5(a). It is observed that the characteristics of the plasma potential are similar to that of a voltage driven device, see figure 2.3. The plasma potential increases linearly when V_{lf} is increased. We find that the plasma potential increases by approximately a factor of 3 for a V_{lf} range of

0 to 350 V. The mean ion bombardment energy to the electrodes is found to have a similar dependence on V_{lf} as the plasma potential, that is, E_i increases linearly with respect to V_{lf} also.

By comparing figure 2.4(b) and figure 2.5(b), It is evident that it is possible to obtain independent control of both the ion current and the bombarding ion energy. The total current can be used to control the plasma density. V_{lf} is then used to control the sheath voltage and the resulting ion bombardment energy.

2.1.3 Asymmetric discharges

In the previous sections we analysed a symmetric capacitively coupled dual frequency device in which the grounded electrode surface area, A_g is equal to the driven electrode surface area A_d. However, most capacitively coupled reactors are asymmetric ($A_g > A_d$) since more electrode surfaces are grounded rather than driven, also the discharge chamber is usually grounded which increases the asymmetry. In this case the smaller electrode must be biased negative with respect to the larger electrode to ensure zero net dc current. Also, in the previous sections the high frequency power source was driven with either constant voltage source or a constant current source. Here we analyse a device in which ω_{hf} is driven with a constant high frequency power source. We do this because plasma devices are often operated by supplying a given power source rather than a current or voltage source. The geometry of the device has now been changed to an asymmetric discharge in which $A_g/A_p = 2$ and the electrode separation has been reduced to 1.5 cm, the background pressure has also been increased to 50 $mTorr$. These operating parameters are chosen to be more representative of typical engineering conditions. The constant high frequency power source is achieved by varying the low frequency power source in order to produce a desired V_{lf} then manipulating J_{hf} in order to maintain a constant P_{hf}. The high frequency power source is then maintained at approximately 1200 Wm^{-2}. This results in the total power supplied to the device increasing, since the power being supplied to the device is a combination of both the high and low frequency components.

Figure 2.6 shows a similar graph to those in figure 2.1 and (2.4). Though the general trends are similar as those in the previous figures, there are small differences. The sheath width on the smaller powered electrode and the grounded electrode are slightly different, the sheath on the smaller powered electrode being the larger of the two.

The dependence of the ion flux bombarding the electrodes is of particular interest. Whereas in figure 2.1, Γ_i decreased continuously as V_{lf} was increased, in figure 2.6, Γ_i is essentially independent of V_{lf}. This is despite the observation that the plasma density decreases significantly. This is superficially surprising considering the observation that the plasma density decreases significantly under the same conditions. The precise reason for this is unclear, although it is tentatively believed to be due to a variation in the electron temperature, this is discussed in the next section. The different ion current density that is observed at each electrode is simply a result of there being an area difference between the two electrodes; the ion current onto both electrodes is the same. This balance of current onto the electrodes is required by the requirement for current continuity. There must be zero net dc current through the plasma.

In figure 2.7, we show the dependence of the plasma potential, self-bias voltage and mean ion energy at the electrodes on V_{lf}. In common with the symmetric discharge, shown in figure 2.3, the plasma potential is observed to

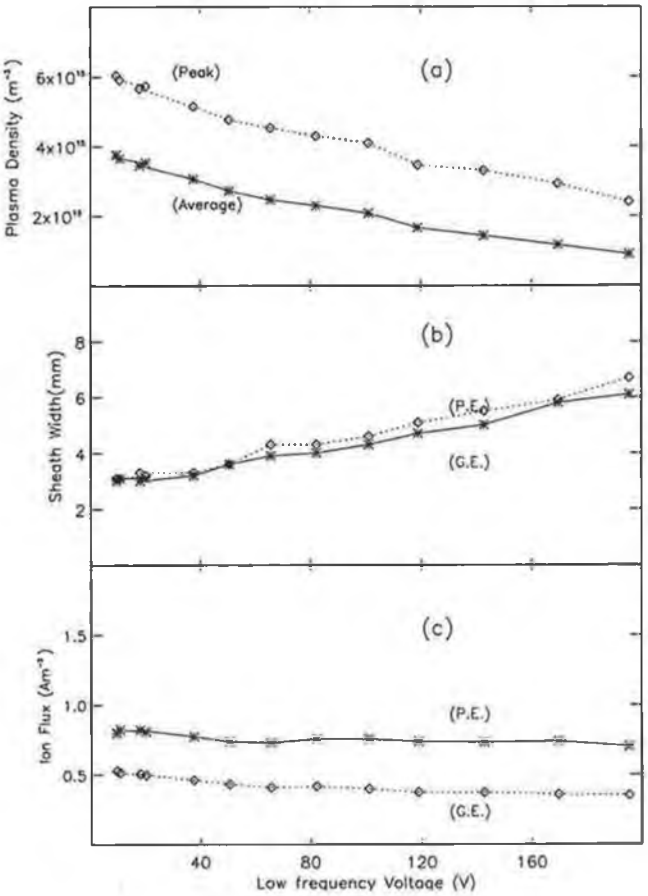

Figure 2.6: General plasma parameters for an asymmetric dual frequency plasma discharge, where there is an area ratio of two between the powered and grounded electrodes. ω_{hf} is driven with a constant power source, V_{lf} is then varied. Background pressure of $50mTorr$ and which the electrode separation is 1.5 cm.

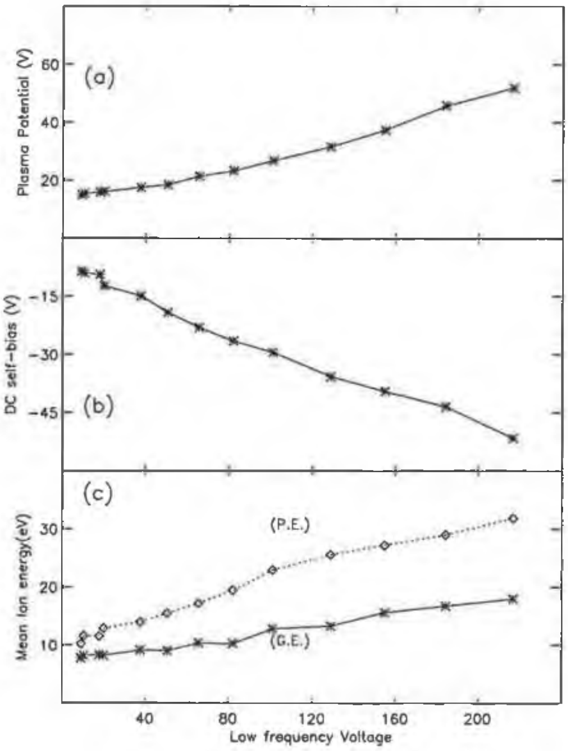

Figure 2.7: Plasma potential, self-bias voltage and mean ion energy for an asymmetric discharge. Operating conditions as in figure 2.6.

be linearly dependent on V_{lf}. Since the discharge which is being simulated is asymmetric, there develops on the smaller of the two electrodes a dc-self bias voltage [45–47], this is shown in figure 2.7(b). The dc-self bias voltage is observed to increase linearly with increasing V_{lf}. In an asymmetric discharge the ratio of the voltage across each sheath is given by the following [48]

$$(\frac{A_1}{A_2})^q = (\frac{V_2}{V_1}). \tag{2.4}$$

Where $V_{1,2}$, $S_{1,2}$ and $A_{1,2}$ are the sheath voltage, sheath width and area of each electrode, and q is a constant scaling exponent, which under the conditions here, is approximately equal to unity. This equation is found to be valid also for a dual frequency plasma device. Therefore, if the plasma potential increases linearly, then the self bias voltage must also increase in order for the ratio V_2/V_1 to remain constant; which is what we observed. The mean energy of the ions bombarding the electrodes is then shown in figure 2.7(c). The mean energy at both electrodes is observed to increase linearly with increasing V_{lf}, as is expected. The energy of the ions bombarding the powered electrode is larger as a result of the dc-self bias voltage on the powered electrode.

Thus, by comparing figure 2.6 and figure 2.7(c) it is evident that the ion flux onto the electrodes and the ion current can be controlled independently.

2.1.4 Electron Temperature

The electron temperature is of extreme importance within plasma discharges. This is due to the plasma chemistry being strongly dependent on the electron temperature. The ionization rate is exponentially dependent on the electron temperature. It is therefore of interest to know and understand what effect operating a plasma device with two separate frequencies has on the electron temperature.

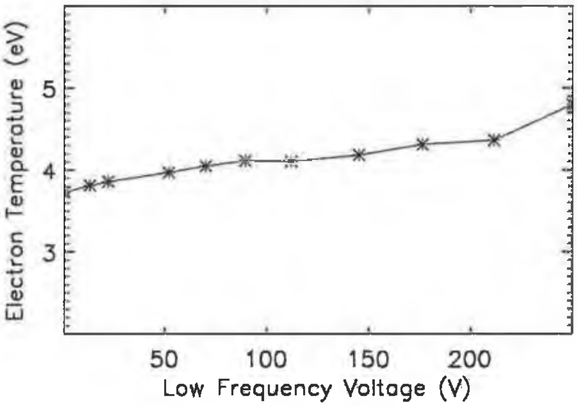

Figure 2.8: Average bulk electron temperature as a function of low frequency voltage. Background gas pressure of 50 $mTorr$ and an electrode separation of 1.5 cm. Parameters as in figure 2.6.

Shown in figure 2.8 is the variation in the electron temperature as a function of V_{lf}. The electron temperature presented here corresponds to the data shown in figure 2.6. It is observed that the bulk electron temperature increases approximately linearly with increasing V_{lf}. In calculating the electron temperature, the average temperature within the central two millimetres of the bulk plasma was determined.

The electron temperature within a gas discharge is determined by a particle balance equation. In the notation of [10], the electron temperature is given by

$$\frac{K_{iz}(T_e)}{u_b(T_e)} = \frac{1}{pd_{eff}}. \tag{2.5}$$

Where K_{iz} and p are respectively the ionization rate and the neutral gas pressure. d_{eff} is then the effective size of the plasma and u_b is the Bohm velocity. This equation if found by equating the rate of particle production with the rate of particle loss to the walls. The above equation can not be inverted to give an analytical expression for the electron temperature, but the general dependence is of the form $T_e \approx \ln(pd_{eff})$.

By examining the above equation we see that the electron temperature is independent of the power supplied, and is determined for a given gas only by the parameter pd_{eff}, although it is observed that the electron temperature increases with increasing V_{lf} in figure 2.8. The electron temperature increase is a result of the sheath width increasing, thus causing the parameter pd_{eff} to decrease resulting in the increased electron temperature. It should be noted that equation(2.5) is valid only for a Maxwellian electron energy distribution function (EEDF), but the general argument remains valid for any distribution function.

The EEDF corresponding to two separate points within figure 2.8 is shown in figure 2.9. The EEDF also corresponds to the electrons within the central two millimetres of the bulk plasma. The shape of the EEDF is found to be strongly non-Maxwellian. It is observed that the EEDF changes considerably with the addition of the second low frequency power source; the number of high energy electrons increases considerably when V_{lf} increases. This results in the average electron temperature increasing, as seen in figure 2.8.

At larger electrode separations, where the two combined sheath widths are only a small fraction of the electrode separation. The electron temperature remains approximately constant. This is a result of the electron temperature being only weakly dependent on the parameter pd_{eff} at large values; because of the near logarithmic dependence of the temperature on

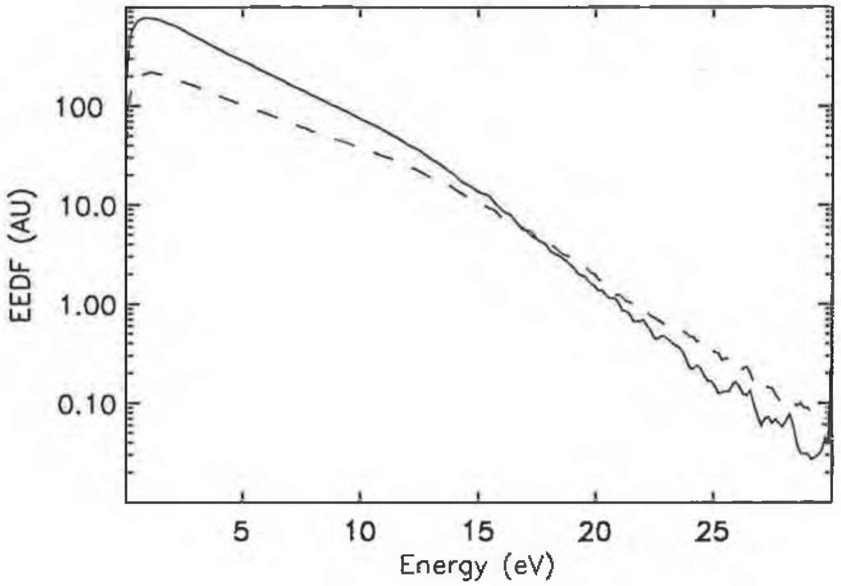

Figure 2.9: Normalised EEDF, solid line represents single frequency device, dashed line $V_{lf} = 200V$. The gas pressure is 50 $mTorr$.

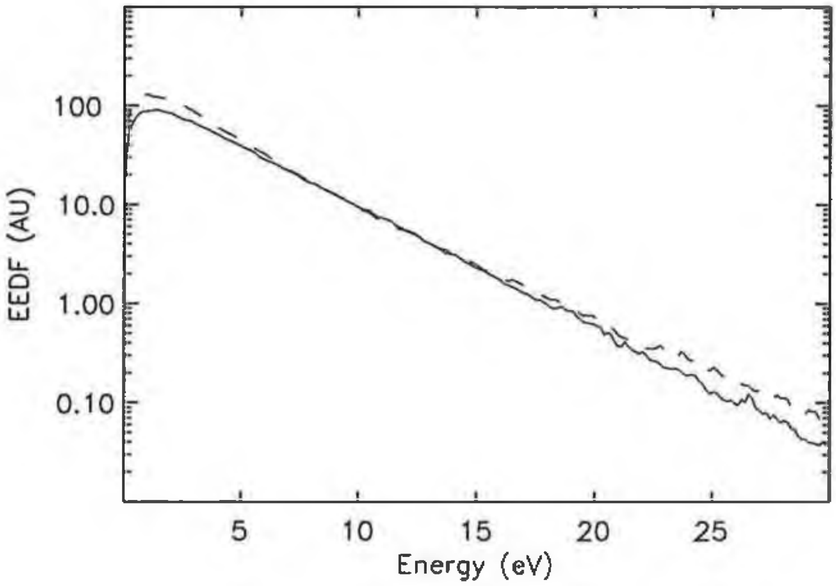

Figure 2.10: Electron energy distribution function for the case where the device is operated with a constant total current, conditions same as in figure 2.4. Dashed line represents case where $V_{lf} = 0V$, solid line $V_{lf} = 280V$.

pd_{eff}. This is illustrated in figure 2.10, where it is observed that the shape of the EEDF changes only slightly when the amplitude of the amplitude of V_{lf} is increased from zero to $280V$. It is only the temperature of the high energy electrons that changes. Though it is these electrons that is of most importance for the plasma chemistry. It is noteworthy that under these conditions the shape of the EEDF is nearly Maxwellian. The data presented in figure 2.10 corresponds to data in figure 2.4.

2.1.5 Discussion

There are, tentatively, two mechanisms responsible for the ion current onto the electrodes remaining constant in figure 2.6(c) even though the electron density is decreasing, as seen in figure 2.6(a). The first mechanism is the increase in the electron temperature. Since the ionization rate is exponentially dependent on the electron temperature, the ionization rate increases considerably as the electron temperature increases. Therefore in order to maintain equilibrium between plasma generation and particle losses to the walls, the flux of ions and electrons leaving the plasma must increase. The second mechanism responsible is the variation in the dimensions of the bulk plasma given by [49]

$$h_l = \frac{n_s}{n_o} \approx 0.86(3 + \frac{(l_o - 2s)}{2\lambda})^{-\frac{1}{2}}. \tag{2.6}$$

Where λ represents the ion mean free path, $(l_o - 2S_m)$ is the effective discharge length and l_o is the electrode separation. h_l relates the plasma densities at the plasma sheath boundary and the bulk plasma [10, 49]. The parameter h_l is dependent on both the dimensions of the plasma and also on the electron temperature. The ion current is then related to this parameter by

$$\Gamma_i = n u_b h_l. \tag{2.7}$$

The increasing sheath width results in the parameter h_l increasing. Thus, the ion current may remain constant even though the plasma density is decreasing. The independence of Γ_i with respect to V_{lf}, when the device is driven with a power source, can therefore only occur at small electrode separations, where the change in the sheath width is comparable to the width of the bulk plasma.

Neither of these mechanisms though, provide a completely satisfactory explanation as to the independent of the ion current. Even by taking these mechanisms into account, basic theory suggests that the current density onto the electrodes should decrease by a greater amount than is observed. Finding a proper mathematical description as to this independence is complicated by the non-Maxwellian distribution function that is observed.

2.2 Ion Distribution Function.

The characteristics of the sheath are usually considered to be resistive if $J_c \gg J_d$ and capacitive if $J_c \ll J_d$, where J_c is the conduction current density and J_d is the displacement current density [50]. For a plasma device operated with a single frequency in a resistive sheath regime; the plasma potential is non-sinusoidal even if the discharge is driven with a sinusoidal potential. The plasma potential under such conditions resembles a half-wave rectified signal clipped at the floating potential. Conversely, the plasma potential for a capacitive sheath is sinusoidal if the discharge is driven with a sinusoidal potential.

For a dual frequency plasma device, there is no clear distinction between the resistive and capacitive sheath regimes. Shown in figure 2.11 is the plasma potential as a function of phase. A similar variation in the sheath voltage with respect to phase is predicted by an analytical dual frequency sheath model that has recently been developed [16].

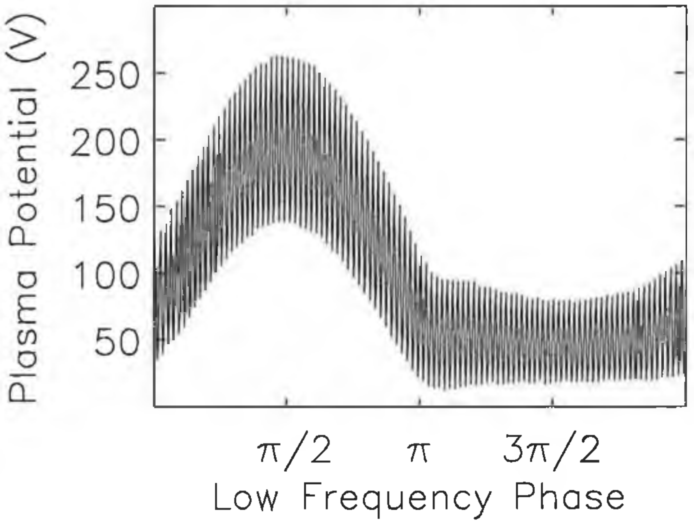

Figure 2.11: Instantaneous plasma potential within dual frequency plasma device as a function of low frequency phase. The low frequency voltage is 150 V. All other conditions as in figure 2.1

In a capacitively coupled plasma, the sheath is determined to be either capacitive or resistive depending on the ion transit time across the sheath in relation to the rf period, numerically this is expressed

$$\frac{\tau_{ion}}{\tau_{lf}} \lesssim 1. \tag{2.8}$$

Where $\tau_{ion} = 3s(M/(2e\bar{V}_s))^{\frac{1}{2}}$ and τ_{lf} are respectively the ion transit time through the sheath and the low frequency period, s and $\bar{V}_s$ are then the sheath width and time averaged sheath potential respectively. Thus if $\tau_{ion}/\tau_{lf} \gg 1$ the sheath tends to be a capacitive sheath, whereas, if $\tau_{ion}/\tau_{lf} \ll 1$, the sheath tends to be resistive. Under the condition being simulated here, the value of τ_{ion}/τ_{lf} is of the order of unity. This implies that the sheath described here is in neither a purely capacitive nor resistive regime.

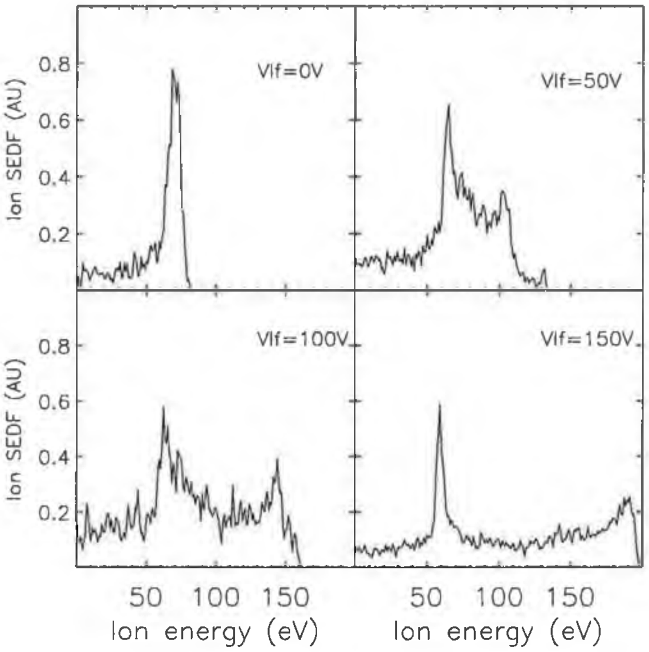

Figure 2.12: Ion distribution function at the electrodes for various low frequency voltages. Conditions correspond to those in figure 2.1

Since the IDF is one of the most important characteristics of an industrial plasma and has been studied extensively in a single frequency device [12, 51–55], we now examine the effect of operating a device with two separate frequencies on the IDF. The IDF's for various low frequency voltages are shown in figure 2.12. Figure 2.12(a) corresponds to the situation in which a device is operated with a single frequency power source at 100 MHz. At 100 MHz, the ion transit time across the sheath is significantly greater than the period of the operating frequency. Therefore, the ions traverse the sheath and experience only the time averaged sheath voltage. This results in the

IDF resembling a single peak centred about the time averaged sheath voltage. When V_{lf} is increased, the IDF loses its single peak structure and takes on the distinctive saddle shape seen in single frequency devices [51, 56, 57]. This results from the ion transit time through the sheath being significantly less than the lf period. The ions therefore experience the instantaneous lf voltage as they traverse the sheath, however the ions continue to experience the hf voltage. This results in there being a minimum peak in the IDF centred about the high frequency component of the sheath voltage; which is approximately 60 V under the conditions being simulated here. The dominance of the low energy peak, in for example figure 2.12(d), is a result of the resistive nature of the sheath that is seen in figure 2.11. The plasma potential is at a low energy for a greater proportion of a cycle than it is at a high voltage. This results in there being a greater proportion of ions entering the sheath when the voltage is at its minimum rather than at its maximum. This is a consequence of the sheath being resistive in nature.

The energy dispersion between the maximum and minimum energy peaks in the IDF was first calculated for a single frequency device by Benoit-Cattin *et al.* [40] and is given, in the notation of [50], by,

$$\frac{\Delta E_i}{e\bar{V}_s} = \frac{2\tilde{V}_s}{\bar{V}_s \omega s}(\frac{2e\bar{V}_s}{M})^{1/2}. \tag{2.9}$$

Since the ions respond only to the low frequency voltage and the time averaged high frequency voltage, then the sheath voltage for the ions can be approximated as $V = \bar{V}_s + \tilde{V}_s \sin(\omega_{lf} t)$. Where $\bar{V}_s$ is the time averaged sheath voltage and can be approximated as $\bar{V}_s \approx V_f + \frac{V_{lf}}{2} + \frac{V_{hf}}{2}$ and $\tilde{V}_s$ can be approximated as $\approx V_{lf}$, V_f is then the floating potential. It is found that by making this change, equation 2.9 provides a good approximation for the energy dispersion.

Importantly, equation 2.9 predicts that $\Delta E \propto \frac{1}{\omega}$. This has been verified,

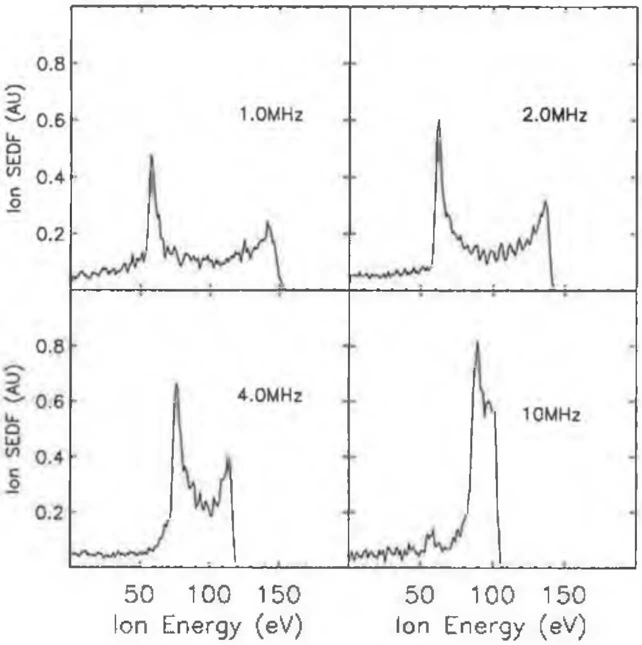

Figure 2.13: Ion distribution function at the electrodes for various low frequencies. The low frequency voltage is maintained at 100 V, all other conditions as in figure 2.1.

and is shown in figure 2.13 which shows that the energy dispersion decreases when ω_{lf} is increased. The IDF therefore changes from having a saddle structure, see at $\omega_{lf} = 1\ MHz$, to having an approximately single peak structure, seen at $\omega_{lf} = 10\ MHz$. Therefore, operating at a higher ω_{lf} can remove the energy dispersion, if this is desired. This solution may not be ideal since at very high frequencies electromagnetic effects become more prevalent [58].

2.3 Analytical Model

In order to better understand the dynamics of dual frequency plasma discharges, an analytical global model has been developed which can explain many of the characteristics observed in the simulations [59]. The assumption is that the total power being supplied by the combination of the two frequency sources is known. The sheath width and the resulting sheath voltages are then assumed to be as a result of only the lower frequency power source. This is a reasonable approximation to make if $\Phi_{lf} \gg \Phi_{hf}$, which will be the usual case within dual frequency discharges when $\omega_{hf} \gg \omega_{lf}$; which is the case for all results presented here. The sheath model of Lieberman [60], is then used to relate the sheath voltage and the sheath width. Within this global model the high frequency is used simply used as a source of power.

Using the Lieberman model, the maximum sheath width is given by the following equation,

$$\frac{s_m}{s_o} = \frac{5\pi}{12} H, \tag{2.10}$$

and the sheath voltage, Φ, by,

$$\frac{\Phi}{T_e} = \frac{9\pi^2}{32} H^2. \tag{2.11}$$

Where H is a dimensionless quantity given by

$$H = \frac{J_{lf}^2}{\pi n e \epsilon_o \omega_{lf}^2 T_e},$$

and S_o is an effective oscillation amplitude given by

$$S_o = \frac{J_{lf}}{n \omega_{lf} e}.$$

Using the notation of [10], the electron temperature is then given by a particle balance equation, see equation 2.5. Finally, the plasma density can be determined by the power balance equation,

$$n = \frac{P_{abs}}{A_{eff} e u_b \xi_t}. \tag{2.12}$$

Where ξ_t represents the energy loss mechanisms given by $\xi_t = \xi_c + \xi_e + \xi_i$ and is equal to the energy that is required to produce an ion-electron pair for a given discharge. The energy loss as a result of collisions is given by ξ_c and the energy lost by the electrons and ions to the walls is given by ξ_e and ξ_i respectively, where for a Maxwellian distribution $\xi_e = 2T_e$ and $\xi_i = \frac{1}{2}T_e + \Phi$.

Combining equations (2.10), (2.11), (2.12) and (2.5) results in a series of coupled nonlinear equations which can be solved to determine the sheath width, plasma density and electron temperature for a given power and sheath voltage. The resulting ion flux onto the electrodes is then given by equation (2.7).

These coupled equations are then solved numerically for a given set of parameters and the solutions are presented in figure 2.14. As can be seen from figure 2.14(a), the model predicts a sheath width which increases linearly as the sheath voltage is increased. This is in agreement with the simulations that have been performed. As a result of this increase in the sheath voltage, the plasma density decreases. This is predominately because the plasma density in equation 2.12 is a function of the sheath voltage, through the parameter

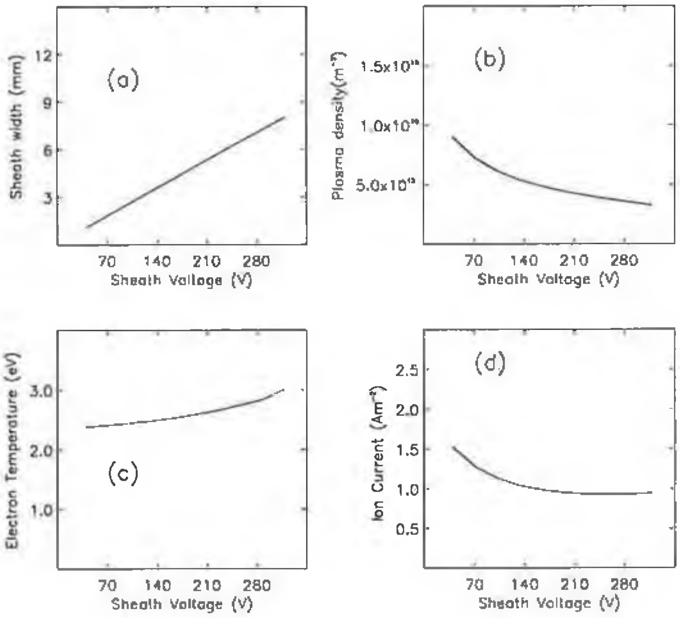

Figure 2.14: Analytical global model solution for the following conditions, electrode separation = 2.0cm and pressure 100mTorr. The high frequency power is then assumed to be 1 kWm^{-2}.

ξ_t, where the energy required to create an ion electron pair increases linearly with respect to sheath voltage. The resulting increase in the sheath width causes the effective width of the bulk plasma to decrease. This results in the electron temperature increasing as a result of the parameter pd_{eff} in figure 2.5 decreasing, see figure 2.14(c). The ion flux onto the electrodes is then given by equation 2.7 and is presented in figure 2.14(d). As can be seen, the flux initially decreases as the sheath voltage increases, although the decrease in the flux is less that the decrease in the plasma density. This is a result of the parameter h_l being dependent on the dimensions of the bulk plasma, through the term $(l_o - 2s_m)$ in equation 2.6. In the limit of large sheath widths the flux begins to saturate, whereas the plasma density continues to decrease for increasing sheath voltages. However, in order for this saturation of the ion flux to occur the expansion the sheath width must be comparable to the dimensions of the bulk plasma.

The main motivation for the above model is simply to provide insight into the underlying physics involved within dual frequency discharges. And although the above global model is quite simple and neglects a great deal of important physics, such as the precise characteristics of the sheath and heating mechanisms, it correctly predicts the general trends within dual frequency plasma discharges.

2.4 Limits on Operating Frequencies

For de-coupled operation between the ion energy and ion current density, it is found that there must be a sufficient separation between the operating frequencies. This is illustrated in figure 2.15 where we plot the normalised ion current density onto the electrodes as a function of the frequency ratio. Where the normalised ion current density is given by, $\Gamma_i = \Gamma_i(\omega_{lf}/\omega_{hf})/\Gamma_i(\omega_{lf}/\omega_{hf} = 0.01)$. Data in figure 2.15 is for a symmetric discharge in which ω_{hf} is held constant at 100 MHz and driven with a constant voltage of 100 V. The geometry of the device simulated here has been changed from the previous configuration for two reasons. Firstly, the electrode separation has been increased in order to reduce the effects of the increasing electron temperature. The second reason is to enable the device to be operated at greater low frequency voltages than that which was simulated in the previous section.

In these calculations ω_{lf} is varied and V_{lf} is held constant, the amplitude is as indicated in figure 2.15. For values of $\omega_{lf}/\omega_{hf} \lessapprox 0.1$, Γ_i is independent of both ω_{lf} and V_{lf}. That is, Γ_i is only dependent on the characteristics of the high frequency driving source. However, for $\omega_{lf}/\omega_{hf} \gtrapprox 0.1$, Γ_i becomes dependent on both ω_{lf} and V_{lf}. It should be noted though that even at large ratio's of the driving frequencies there remains substantial coupling between the two frequencies [16], the potential and sheath width remain strongly dependent on both the high and low frequency power sources.

The dependence of Γ_i on ω_{lf} can be explained as follows. The discharge current is proportional to the square of the operating frequency [25]. This causes $Z_{hf} \ll Z_{lf}$, where Z is the impedance. Therefore, P_{lf} predominately drives the discharge voltage, which couples into the ions and P_{hf} drives the discharge current which predominately couples into the electrons. Increasing ω_{lf}, as in figure 2.15, causes Z_{lf} to decrease. It therefore requires a greater J_{lf} to produce a given voltage, but the power coupled into the electrons is $\propto J^2$, as a consequence of equation (2.1). Therefore, increasing ω_{lf} results in an increased J_{lf}, this in turn causes a greater proportion of P_{lf} to be coupled into the electrons. The increased power being supplied to the electrons forces the electron density to increase. The flux onto the electrodes, being proportional to the plasma density, increases accordingly, as observed in figure 2.15. Although in figure 2.15 the high frequency is held constant at 100 MHz, similar characteristics are obtained if one uses different frequencies.

Figure 2.15, indicates that as one operates at greater values of the applied low frequency voltages, then a greater separation between the frequency ratio is needed in order to maintain the decoupled nature of the device. This may be of particular relevance to those working within industry, where the voltages that are simulated here are relatively low compared to what is sometimes used for applications; within industry voltages up to 1 kV are regularly used.

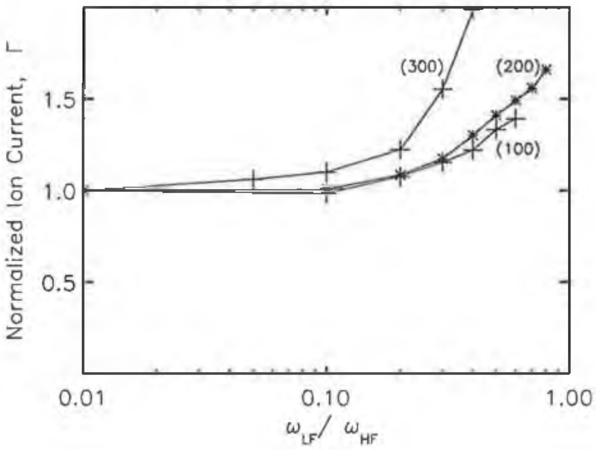

Figure 2.15: Dependence of normalised Γ_i on ω_{lf}. ω_{hf} is held constant at 100 MHz and an applied voltage of 100V, the low frequency is then varied. The inscription refers to the low frequency voltage amplitude. Data obtained for a symmetric discharge with an electrode separation of 3 cm.

2.5 Discussion

The results presented demonstrate, that the energy and flux of the ions bombarding the electrode surface can be controlled independently. There are regimes in which it is possible to achieve this. For large electrode separations, in which the increase in the sheath width is small compared to the electrode separation; the ion current can be controlled by varying total discharge current. Although in practice this is extremely difficult achieve within real devices. At smaller electrode separations, the increasing electron temperature maintains a constant ion flux. Although this results in the electron temperature increasing.

Within dual frequency discharges the structure of the IDF at the electrodes is substantially modified. The IDF resembles a single peak centred at V_{hf} when $V_{lf} = 0$. As the low frequency voltage is increased the IDF changes and takes on the distinctive bimodal structure seen in single frequency devices.

If the ratio of the high to low frequencies is sufficiently large, essentially independent control of the ion energy and flux is possible by manipulation of the externally controllable power sources. The system appears to maintain its decoupled nature, under conditions simulated here, for values of $\omega_{hf}/\omega_{lf} \gtrapprox 10$. When operating dual frequency devices at higher voltages than are being simulated here, it may be necessary that a greater ratio of the operating frequencies is needed in order for the device to maintain its decoupled nature. While the results presented here are for relatively low voltages and powers, it was found that the general trends can be extrapolated to much greater voltages.

CHAPTER 3

Collisionless Analytical Sheath Model

In order to better understand the highly non-linear sheath dynamics of a single frequency symmetrically driven (equal-area plates) device, various authors [49, 60–63] have developed sheath models in rf coupled discharges, where the electron dynamics are strongly non-linear. M. A. Lieberman developed the first self-consistent model for a collision-less sheath that can be employed to successfully describe these non-linear dynamics. To date, any attempt to model a dual frequency sheath in the small ion transit time regime has been unsuccessful (in [64], the lower frequency is below the inverse of the ion transit time). Here we present a collision-less sheath model for the case of a capacitively coupled plasma that is driven by two distinct power sources operating at two distinctly separate frequencies. A schematic of this design is shown in figure (3.1). In this model, the current density flowing through the plasma is the sum of two sinusoidal rf current densities oscillating at two different frequencies. Within this model, we obtain analytical expressions for the time average electric potential within the sheath, nonlinear motion of the electron sheath boundary and non-linear instantaneous sheath voltage. Note that the Lieberman's single frequency sheath model is retrieved if we set the high frequency current density to zero.

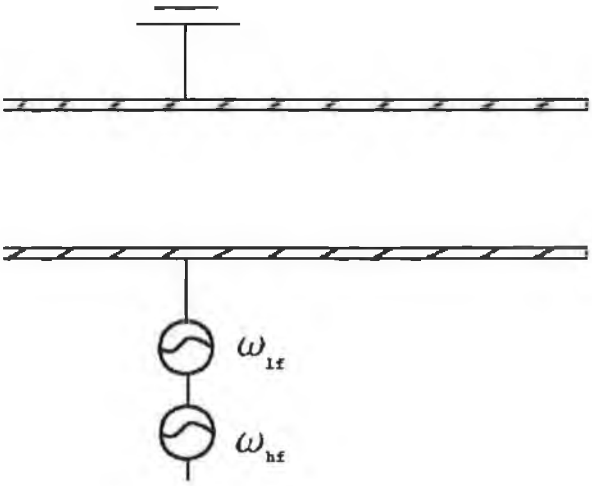

Figure 3.1: Schematic of a dual frequency excited rf plasma system.

In order to confirm the results of this model, the solutions have been compared to the Particle-in-Cell/Monte-Carlo collisions (PIC-MCC) simulation results. We have used a one dimensional simulation in order to perform our investigation. The electrodes are assumed to be perfectly absorbing, and no secondary electrons are emitted. The simulations have been performed using Argon as the background gas and three particle types are simulated, electrons, neutral Argon and singly charged Ar^+. Double frequency analytical expressions such as the sheath voltage and sheath width have been compared with simulation results, finding good agreement.

3.1 Model assumptions

The assumptions of the analysis are as follows: we make similar assumptions as for the single radio frequency sheath model. First, the ion motion within the sheath is entirely collisionless. The sheath width s_m, is typically of the order of a centimetre and the ion mean free path λ_i is approximately given by:

$$\left[\frac{\lambda_i}{\mathrm{cm}}\right] = \frac{1}{330}\left[\frac{\mathrm{Torr}}{p}\right] \tag{3.1}$$

When rf capacitive reactors operate at pressures less than 10 milliTorr, the ion mean free paths are on the order of the sheath width. Later in section 3.3 where the solutions are compared to PIC-MCC results, the simulations are performed at a pressure of 10 milliTorr. Secondly, because of their inertia, the ions do not respond instantaneously to the electric field. Then we make the assumption that the ions respond to only the *time averaged electric fields.* This assumption will be valid [50] if the strong inequalities $2\pi\tau_i^{-1} \ll \omega_{lf} \ll \omega_{hf}$ are satisfied where τ_i is the ion transit time across the sheath and $\omega_{lf,hf}$ are the low and high driving frequencies, respectively. This strong inequality means that the sheath studied here is capacitive. It should be noted that the inequality $2\pi\tau_i^{-1} \ll \omega_{lf}$ will not hold under all situations which are of practical interest. This is particularly true if light gases such as hydrogen or helium were to be used. Thirdly, the ion sheath boundary is assumed to be stationary and we apply the Bohm criterion, i.e. the ions enter the ion sheath edge with a velocity equal to the Bohm velocity: $u_b = (eT_e/m_i)^{1/2}$ where e is the electronic charge, T_e the electronic temperature expressed in volt and m_i is the ion mass [21]. As far as the electrons are concerned, we assume that the electron Debye length λ_d is much smaller than the ion sheath thickness s_m. Since $\lambda_d \ll s_m$ the electron density falls sharply from $n_e \approx n_i$

at the plasma side of the electron sheath boundary to $n_e = 0$ on the electrode side. With this approximation, the electron density profile is assumed to be represented by a step function at the electron sheath edge. This step model approximation is known to be reasonable for large sheath voltage [65, 66]. In contrast to the ions, the electrons respond to the instantaneous electric field because we assume that the electron plasma frequency greatly exceeds the two rf frequencies $\omega_{pe} \gg \omega_{hf} \gg \omega_{lf}$.

3.2 Analytical Model

The following derivation is similar to that used to derive the equations for the single frequency case. We consider the sheath structure depicted in figure (3.2). Ions cross the ion sheath edge at $x = 0$ with a velocity equal to u_b and strike the electrodes at $x = s_m$ with a energy equal to the time averaged sheath potential. We assume that the current density $J(t)$ passing through the sheath is the sum of two sinusoidal rf current densities

$$J(t) = J_{lf}\sin(\omega_{lf}t) + J_{hf}\sin(\omega_{hf}t) \tag{3.2}$$

where the labels lf and hf refer to the low and high frequency components of the rf current respectively. We have intensionally chosen the conditions so that there is no phase difference between the frequencies to reduce the mathematical difficulties involved.

In the dual frequency case, the electron sheath edge motion is no longer simply oscillating back and forth but is, as we will show in the following derivation, a complicated motion described by the instantaneous sheath position $s(t)$. We first consider the ion dynamics in the sheath. Since we assume that there is no ionization or recombination within the sheath, the ion flux

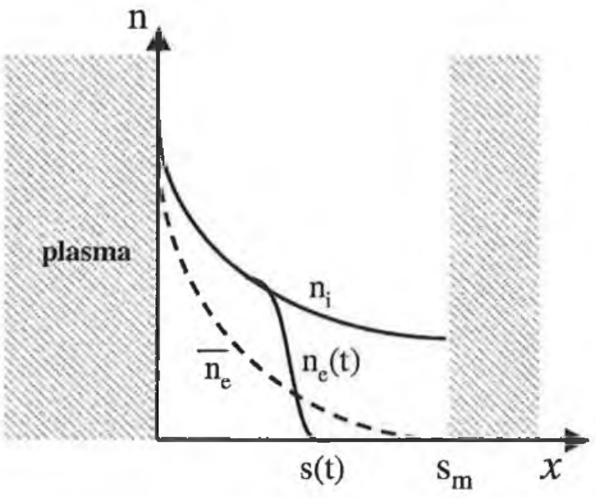

Figure 3.2: Structure of the rf capacitive sheath. $s(t)$ is the electron sheath edge position.

through the sheath is constant and equal to the Bohm flux

$$n_i(x)u_i(x) = n_o u_b \tag{3.3}$$

where n_o is the plasma density at the ion sheath edge and $n_i(x)$, $u_i(x)$ are respectively the ion density and ion velocity at point x. Next, for collisionless motion, conservation of ion energy requires that:

$$\frac{1}{2}m_i u_i^2(x) + e\bar{\Phi}(x) = \frac{1}{2}m_i u_b^2 \tag{3.4}$$

where $\bar{\Phi}(x)$ is the time averaged electric potential. This energy conservation equation is valid if the applied rf frequency is much higher than the inverse of ion transit time so that the ions are not able to adjust to the rapid change of the potential. The instantaneous electronic charge density $n_e(x,t)$ can be written as :

$$\begin{aligned} n_e(x,t) &= \quad 0 \qquad\qquad x > s(t) \\ &= n_i(x) \qquad\quad x < s(t). \end{aligned} \tag{3.5}$$

where we assume the instantaneous electron sheath edge is sharp, and $s(t)$ is the instantaneous electron sheath edge position. Hence the net charge density ρ is

$$\begin{aligned} \rho(x,t) &= n_i(x) - n_e(x,t) \\ &= n_i(x) \qquad x > s(t) \\ &= 0 \qquad x < s(t). \end{aligned} \tag{3.6}$$

The instantaneous electric field $E(x,t)$ is then given by the solution of Poissons equation

$$\begin{aligned} \frac{\partial E}{\partial x} &= \tfrac{e}{\varepsilon_o} n_i(x) \qquad x > s(t) \\ &= 0 \qquad x < s(t). \end{aligned} \tag{3.7}$$

where $\varepsilon_o = 8.85 \times 10^{-12}$ F.m^{-1} is the permittivity of free space. The instantaneous potential $\Phi(x,t)$ is defined by

$$\frac{\partial \Phi}{\partial x} = -E(x,t). \tag{3.8}$$

We now time average equations (3.7) and (3.8) to obtain the equations for the average electric field $\bar{E}(x)$ and for the average electric potential $\bar{\Phi}(x)$

$$\frac{d\bar{E}}{dx} = \frac{e}{\varepsilon_o}(n_i(x) - \bar{n}_e(x)) \tag{3.9}$$

and :

$$\frac{d\bar{\Phi}}{dx} = \bar{E}(x). \tag{3.10}$$

The time averaged electronic density $\bar{n}_e$ is defined as

$$\bar{n}_e(x) = \frac{\omega_{lf}}{2\pi} \int_{\frac{-\pi}{\omega_{lf}}}^{\frac{\pi}{\omega_{lf}}} n_e(x,t)dt. \tag{3.11}$$

In (3.11), we average over a low frequency (lf) period $2\pi/\omega_{lf}$ since this is the longer time scale. As opposed to the single frequency case where the integration in (3.11) can be performed without any approximations [48], the dual frequency case requires an additional assumption. When considering time-averaged quantities, we assume that the hf part of the electric field does not play a significant role because the current in the sheath is displacement current dominated. From charge conservation and Poissons equation, we note that the electric field scales as J/ω. Therefore, average sheath potential is predominantly affected by the lf part of the current. Since the average electron density is related to the average electric field through the averaged Poisson equation (see (3.9) and (3.10)), $\bar{n}_e$ is also weakly dependent on the hf component of the electric field. As a consequence, if $E_{lf} \sim J_{lf}/\omega_{lf} \gg E_{hf} \sim J_{hf}/\omega_{hf}$, we can introduce as in [60] the phase $\phi(x)$ such that the sheath position $s(t)$ is between 0 and x for $-\phi < \omega_{lf}t < \phi$. Therefore, the integrand in equation (3.11) is zero for $-\phi \leq \omega_{lf}t \leq +\phi$ and equation (3.11) reduces to:

$$\bar{n}_e(x) = n_i(x)\left(1 - \frac{\phi}{\pi}\right) \tag{3.12}$$

We now apply current conservation at the electron sheath edge to obtain a equation for the sheath edge motion. On the bulk plasma side of the electron sheath edge, the current is assumed to be entirely due to the conduction current. In the sheath, all the current is assumed to be displacement current. The contribution due to the ions and electron current within the sheath is neglected. Then, at the electron sheath boundary $x = s(t)$, conduction current and displacement current (3.2) must balance, giving

$$en_i(s)\frac{ds}{dt} = J_{lf}\sin(\omega_{lf}t) + J_{hf}\sin(\omega_{hf}t). \tag{3.13}$$

In the single frequency case $J_{hf} = 0$, the set of equations (3.20), (3.9), (3.10), (3.12) and (3.13) can be solved exactly for the unknown quantities n_i,$\bar{n}_e$,$\bar{\Phi}$,$\bar{E}$ and $s(t)$ [60]. However, for a dual frequency system, it is not possible unless we make a necessary simplification which is explained later. The instantaneous electric field $E(x,t)$ can be obtained by integrating equation (3.7)

$$\begin{aligned} E(x,t) &= \tfrac{e}{\epsilon_o}\textstyle\int_{s(t)}^{x} n_i(x')dx' && s(t) < x \\ &= 0 && s(t) > x \end{aligned} \qquad (3.14)$$

From equation (3.13), we can express the integral in equation (3.14) as

$$\tfrac{e}{\epsilon_o}\textstyle\int_{o}^{s(t)} n_i(x)dx = \tfrac{J_{lf}}{\epsilon_o\omega_{lf}}(1-\cos(\omega_{lf}t)) + \tfrac{J_{hf}}{\epsilon_o\omega_{hf}}(1-\cos(\omega_{hf}t)) \qquad (3.15)$$

where we have chosen the initial condition $s(0) = 0$. Now according to equations (3.14) and (3.15), we obtain the instantaneous electric field as follows

$$E(x,t) = \frac{e}{\epsilon_o}\int_0^x n_i(x)dx - \frac{J_{lf}}{\epsilon_o\omega_{lf}}(1-\cos(\omega_{lf}t)) - \frac{J_{hf}}{\epsilon_o\omega_{hf}}(1-\cos(\omega_{hf}t)) \quad (3.16)$$

for $s(t) < x$ and 0 otherwise. This equation follows from splitting the integral of the ion density from zero to x into two: zero to $s(t)$ and $s(t)$ to x. The result given then follows on substituting terms from (3.14) and (3.15). We must now time average the electric field over a low frequency rf cycle. The time averaged electric field is given by

$$\bar{E}(x) = \frac{\omega_{lf}}{2\pi}\int_{\frac{-\pi}{\omega_{lf}}}^{\frac{\pi}{\omega_{lf}}} E(x,t)dt. \qquad (3.17)$$

In a similar manner to the calculation of the average electronic densities, the integration in (3.17) can not be performed without approximation. Again, we use the assumption that the hf electric field, which is proportional to J_{hf}/ω_{hf}, is much smaller than the lf component, which is proportional to J_{lf}/ω_{lf}. Hence, we neglect the hf component to calculate the average electric field and we consider that the average electric field follows the same phase as the average electronic density. Then, it turns out that the mathematical difficulties of the problem can be greatly reduced, while still maintaining the physical content of the model. Thus, inserting (3.16) in (3.17) and neglecting the hf part of the electric field, we find the time averaged electric field:

$$\bar{E}(x) = \frac{J_{lf}}{\epsilon_o \pi \omega_{lf}}(\sin\phi - \phi\cos\phi). \tag{3.18}$$

We are now in a position to derive the two fundamental equations governing the dual frequency electron sheath edge motion. The two fundamental differential equations of the model can then easily be rewritten as the following. According to equations (3.8) and (3.18)

$$\frac{d\bar{\Phi}}{dx} = -\frac{J_{lf}}{\epsilon_o \pi \omega_{lf}}(\sin\phi - \phi\cos\phi), \tag{3.19}$$

which is the *first fundamental equation.* From (3.3) and (3.4), we obtain a representation of the ion density as a function of the time averaged potential:

$$n_i = n_o\left(1 - \frac{2\bar{\Phi}}{T_e}\right)^{-1/2}. \tag{3.20}$$

Next, inserting equation (3.20) in the current balance equation (3.13) and setting $s = x$ when $\phi = \omega_{lf}t$, we obtain the *second fundamental equation*

$$\frac{d\phi}{dx} = \frac{\left(1 - \frac{2\bar{\Phi}}{T_e}\right)^{-1/2}}{s_o(\sin(\phi) + \beta\sin(\alpha\phi))}, \tag{3.21}$$

where the effective oscillation motion amplitude s_o is defined as

$$s_o = \frac{J_{lf}}{e\omega_{lf}n_o}$$

Numerically :

$$\left[\frac{s_o}{\text{cm}}\right] = 0.06 \times \left[\frac{J_{lf}}{\text{A.m}^{-2}}\right]\left[\frac{\text{MHz}}{\omega_{lf}}\right]\left[\frac{10^{10}\text{cm}^{-3}}{n_o}\right]$$

. In equation (3.21) we have introduced the two parameters $\beta = \frac{J_{hf}}{J_{lf}}$, the hf/lf current ratio and $\alpha = \frac{\omega_{hf}}{\omega_{lf}}$ the hf/lf frequency ratio. Recasting the condition that the hf field is much smaller then the lf field in terms of the two parameters α and β,we obtain the condition $\beta/\alpha \ll 1$ under which the present model is valid. Thus, we have obtained a closed set of nonlinear equations, i.e. equations (3.19) and (3.21) which determine the spatial dependence of the sheath parameters such as the average potential and the ion density. It must be stressed that (3.19) is same as that for a single frequency case, the only difference is (3.21) where the additional term proportional to β describes the high frequency part of the instantaneous electronic sheath motion.

To calculate the potential as a function of the phase ϕ we divide (3.19) by (3.21) and obtain the following differential equation

$$\frac{d\bar{\Phi}/T_e}{d\phi} = H \times (1 - \frac{2\bar{\Phi}}{T_e})^{1/2}(\sin\phi - \phi\cos\phi)(\sin\phi + \beta\sin\alpha\phi) \qquad (3.22)$$

This first order differential equation (3.22) can be easily integrated with the following boundary conditions, $\bar{\Phi} = 0$ at $\phi = 0$, corresponding to a plasma potential equal to 0 ($\phi = 0$ is the phase at the maximum electronic sheath width $x = 0$). We obtain the following result

$$(1 - \frac{2\bar{\Phi}}{T_e})^{\frac{1}{2}} = 1 + H \times \int_0^{\phi} d\phi(\sin\phi - \phi\cos\phi)(\sin\phi + \beta\sin\alpha\phi) \qquad (3.23)$$

where we have introduced the parameter H defined as:

$$H = \frac{1}{\pi}\left(\frac{s_o}{\lambda_D}\right)^2 = \frac{J_{lf}^2}{en_o\pi\epsilon_o\omega_{lf}^2 T_e}$$

Numerically

$$H = 22.5\left[\frac{J_{lf}}{\mathrm{A.m^2}}\right]^2\left[\frac{\mathrm{MHz}}{\omega_{lf}}\right]^2\left[\frac{10^{10}\mathrm{cm}^3}{n_o}\right]\left[\frac{\mathrm{eV}}{T_e}\right]$$

Equation (3.23) gives the average potential and the ion density at the sheath edge as a function of the phase ϕ. In contrast to the single frequency case, $\bar{\Phi}$ is a nonlinear *oscillating* function because now the sheath edge motion oscillates at the frequency ω_{hf} around a given point x. Next, we solve (3.23) for $\bar{\Phi}$ and insert the average potential into the second fundamental equation (3.21). Integrating again with respect to the phase, we obtain the instantaneous electronic sheath motion as a function of phase

$$\frac{x}{s_o} = \int_o^{\phi} d\phi'(\sin\phi' + \beta\sin\alpha\phi')\Big(1 + H \times \int_0^{\phi'} d\phi''(\sin\phi'' - \phi''\cos\phi'')(\sin\phi'' + \beta\sin\alpha\phi'')\Big) \tag{3.24}$$

where we have choose the boundary condition $x = 0$ (corresponding to a sheath fully expanded) at $\phi = 0$. Note that closed form solutions in term of trigonometric functions, for the integrals (3.23) and (3.24) can be easily obtained. However, we do not report the explicit calculation of these integrals since they involve a large number of terms and for this reason are not very illuminating. The two main results of this study are given by the equation (3.24) and (3.23). Starting from these two equations, we can calculate for a given set of parameters the average and instantaneous sheath width and potential. It is also possible to obtain the charge and electronic densities. In the context of our study, we focus in the following section on the dependence of the sheath parameters with respect to the frequency ratio α and current ratio β.

It is noted, that analytical approximations for equations (3.23) and (3.24) have been developed in [67] reproduce well the results obtained here.

3.3 Analytical model and PIC Comparison

We now present some solutions to the above analytical model and compare them to PIC simulation results. We first consider the electron sheath motion. We integrate equation (3.24) for a typical set of parameters, the solution to this equation is shown in figure (3.3) for half a cycle. It can be seen that the sheath shows a strongly nonlinear oscillating behaviour. Also, we note that the amplitude of the hf part of the electron sheath motion is much greater close to the electrode rather than at the point where the sheath is fully developed, $\phi = 0$. This nonlinearity in the sheath motion is found to be strongly dependent on the values of the parameters α, β and H. Next figure (3.4) shows the electron sheath motion obtained this time from the PIC code. To determine the sheath edge from the PIC data, we choose the point where the quasi-neutrality condition fails. Comparison between figures (3.3) and (3.4) shows good agreement.

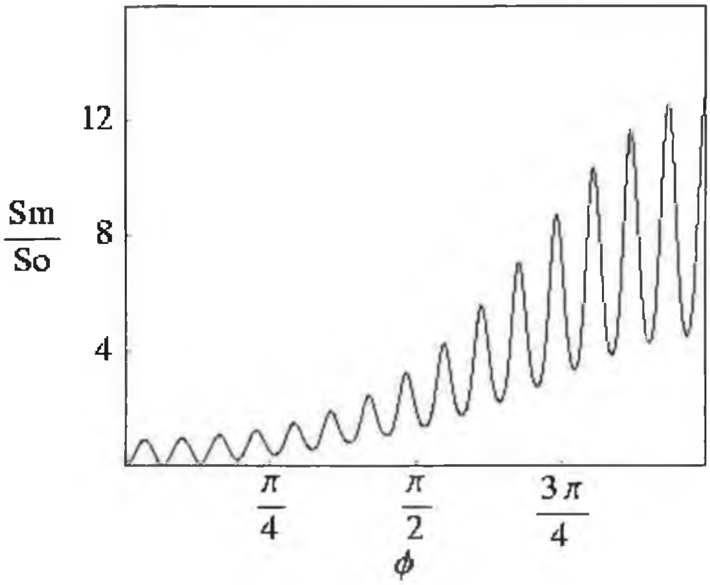

Figure 3.3: Instantaneous electron sheath motion versus phase obtained from the analytical model, $\phi = \omega_{lf} t$, for the following parameters : current ratio $\beta = 14$, frequency ratio $\alpha = 31$ and for $H = 3.5$. The plasma sheath interface is at position zero.

We now consider the instantaneous sheath voltage. By solving equation

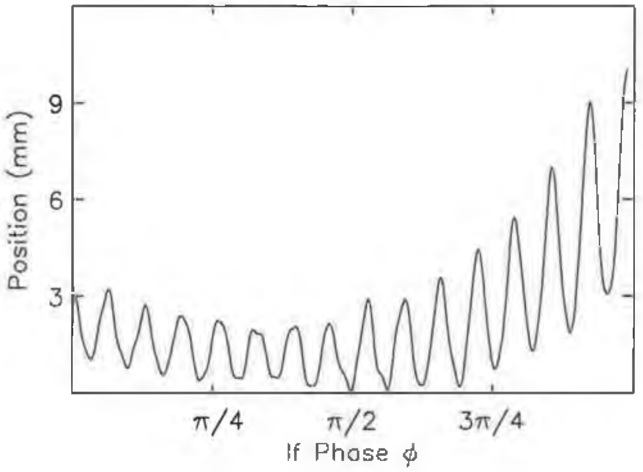

Figure 3.4: Instantaneous electron sheath motion versus phase obtained from the PIC code, $\phi = \omega_{lf}t$, for the following parameters : $\beta = 14$, $\alpha = 30$. Conditions are as follows: $J_{lf} = 3.5$, A.m^{-2}, $\omega_{lf} = 6.28$ Mrad.s^{-1}; the resulting value of H is 3.5 as in figure (3.3).

(3.23), we obtain the potential as a function of phase. This solution is shown in figure (3.5) for a given set of parameters. As expected, the nonlinearity of the electron sheath motion results in an extremely nonlinear instantaneous sheath potential. It is observed that for approximately half of the lf cycle, there is essentially no potential across the sheath and therefore no power being supplied to the sheath.

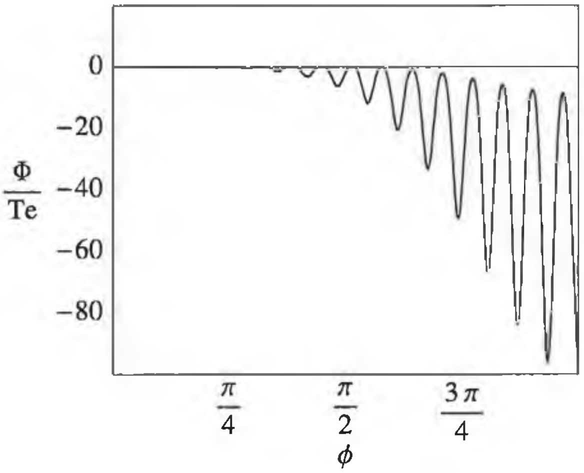

Figure 3.5: Normalised sheath potential as a function of phase, $\alpha = 30, \beta = 14, H = 3.5$.

We see on figure (3.3) and figure (3.5) that many values of the phase give rise to the same value of the instantaneous electronic sheath width and instantaneous sheath voltage. This is a result of the hf motion. However, as expected, a given sheath width results in a unique charge density and therefore a given sheath potential. Hence, if we plot the instantaneous potential as a function of the electron sheath position, we obtain the time average potential experienced by the ion. This plot is given in figure (3.6).

We define the sheath width as the electron sheath position at the time corresponding to $\phi = \pi$. Note that any definition of the sheath width is

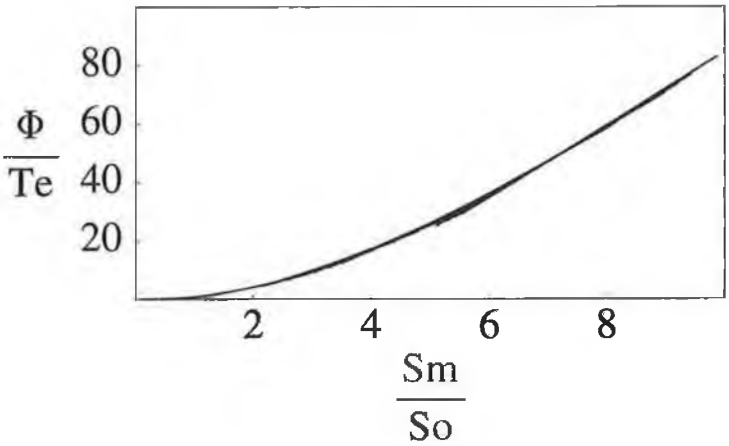

Figure 3.6: Normalised time averaged sheath potential as a function of position. Where the conditions are as follows $\alpha = 101, \beta = 20$ and $H = 4.0$.

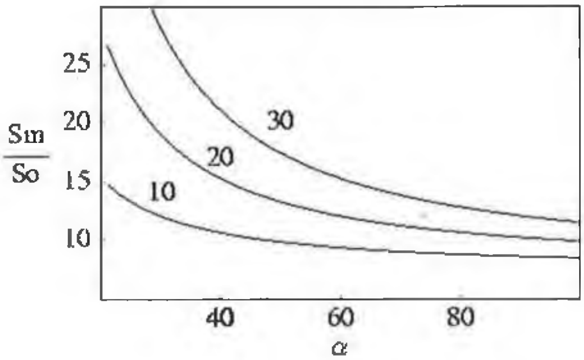

Figure 3.7: Analytical maximum sheath width versus frequency ratio α for three different values of the current ratio $\beta = 10, 20, 30$ and H is equal to 4.

arbitrary. However this definition gives a reasonable estimate of the sheath thickness. Figure (3.7) shows the normalised sheath width versus the frequency ratio α for three different typical values of current ratio β and for a value of H equal to 4. The sheath width is seen to be significantly dependent on α with a stronger dependence at relatively small values of α ($\alpha < 40$). The normalised sheath voltage (Φ/T_e) is also pictured on figure (3.8) versus α for the same values of β.

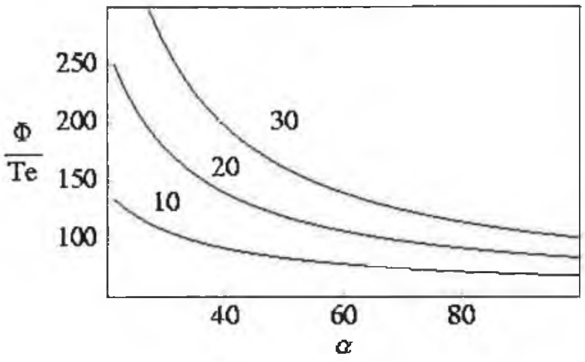

Figure 3.8: Analytical maximum sheath voltage versus frequency ratio α for three different values of the current ratio $\beta = 10, 20, 30$ and H is equal to 4.

On figure (3.9) is shown a comparison between the sheath width obtained from the analytical model and from the PIC simulations as a function of α. At each point, the value of H and s_o have been calculated from the physical quantities obtained from the code. The effect of varying the ratio of the frequencies, α, is that there is an approximately inverse relationship between sheath potential and α. This is understandable, since the high frequency has the effect of reducing the sheath width and therefore reducing the sheath potential. As can be seen, there is good quantitative agreement between the two approaches. The absolute value of the sheath widths agrees to within 20%, and the comparison in the general trends is much better. Much of the

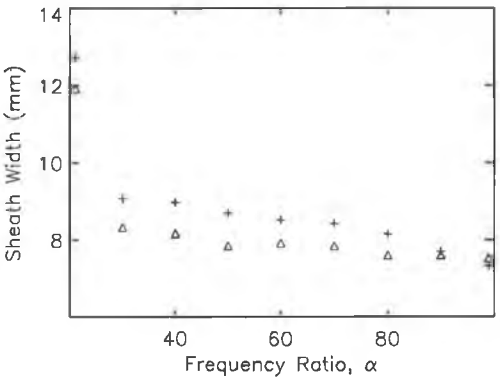

Figure 3.9: Comparison of sheath width predicted by the analytical model and PIC-MCC simulations. Conditions are as follows: $J_{lf} = 3.5$ A.m^{-2} , $\omega_{lf} = 6.28$ Mrad.s^{-1} and $\beta = 20$. + represents the PIC Simulations, $\diamondsuit$ represent the analytical model. α is the ratio of the high frequency to the low frequency

difference in absolute value may be attributed to the fact that the parameter H extracted from the code depends strongly on the electron temperature T_e. For a significant deviation of the electron energy distribution function from a Maxwellian distribution, the value of T_e is questionable, which is the case within the PIC simulations. As a consequence, the resulting calculated analytical sheath width deviates from the simulation results. Then shown in figure (3.10) is the dependence of the sheath width on the parameter β. Again the comparison between the two methods is good.

Very closely related to the sheath width is the potential drop across the sheath. In figures (3.11) and (3.12) are the dependence of the sheath potential on the parameters α and β, for the same conditions as in figures (3.11) and (3.12). It is found that the sheath potential decreases approximately linearly as the parameter α increases. The comparison between the two models is

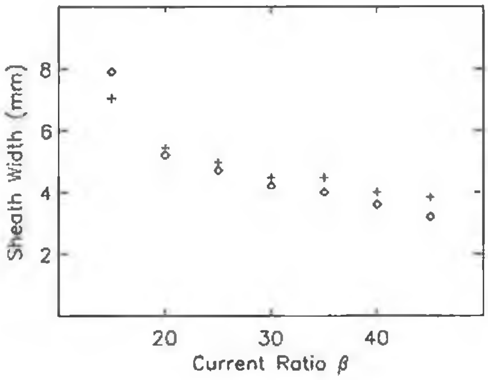

Figure 3.10: Comparison of PIC simulations of sheath width vs β (the ratio of the high frequency current to the low frequency current) with the sheath width predicted by analytical model for the same conditions as in the previous figure. α is held constant at 100. + represents the PIC Simulations, $\Diamond$ represent the analytical model.

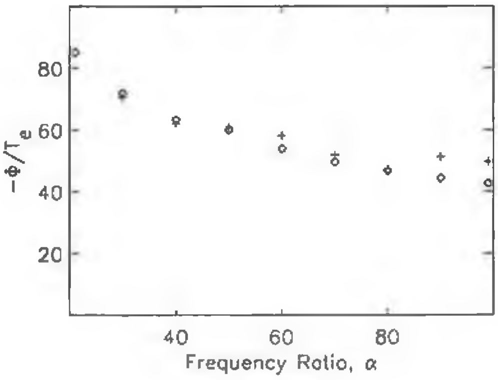

Figure 3.11: Normalised sheath potential as a function of α, the ratio of the two driving frequencies. Conditions are the same as in previous figure. The current ratio is fixed at $\beta = 20$, + represents the PIC Simulations, $\Diamond$ represent the analytical model.

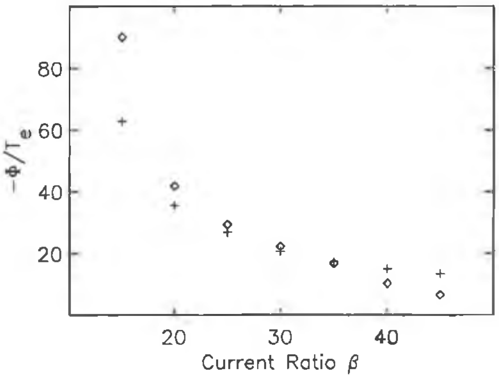

Figure 3.12: Normalised sheath voltage as a function of β, the ratio of the driving currents, for the following conditions, $\alpha = 100$. All others conditions are the same as in previous figure.

extremely good. The comparison between the PIC and analytical model when the parameter β varies is also good. Although at high and low values of β there is a small difference between the two methods.

3.4 Discussion

We have presented a sheath model for the case where the electrode is driven with two separate current sources at different frequencies. The model has been derived under the approximations that the hf electric field is much smaller than the lf counterpart. We have obtained important sheath parameters such as the instantaneous electron sheath motion and sheath potential. The analytical results have been compared to PIC simulations results. We have found both good quantitative agreement between the two approaches. In particular, both numerical and analytical models predict an increase in the hf component of the electron sheath edge motion in the vicinity of the electrode. The model predicts also the frequency ratio and current ratio dependence of both the sheath width and sheath potential. An important point predicted by the model and confirmed by the PIC-MCC results is that although the hf field is much smaller the lf field in typical dual frequency operating regime, the hf field significantly modifies the sheath parameters such as the sheath width and the dc sheath voltage drop.

CHAPTER 4

Variable Pressure Sheath Model

In the previous chapter we presented an analytical sheath model which accurately describes the nonlinear dynamics of a dual frequency sheath. However, this model is valid only in the low pressure regime, around a few milliTorr, where the ion mean free path is larger than the sheath width; higher pressures are required in typical material processing. Therefore, a collisional model is needed to determine the sheath properties. The purpose of this chapter is to extent the validity of the collisionless sheath model, obtained in the previous chapter, to higher pressures where collisional processes take place [68]. At low pressure, the ion motion within the sheath is collisionless and a dual frequency sheath solution has been obtained in the limit where the ions fall through the sheath and gain an energy equal to the time averaged voltage drop.

At higher pressures, competition between collisional drag and acceleration by the sheath electric field results in an ion drift motion within the sheath. In this case the sheath properties depends on the ion drift velocity. In this collisional case, it can be shown that the mobility scaling law depends only on the reduced electric field E/p, where E is the electric field and p is the background gas pressure. In the high E/p regime of interest here (the so-called strong field regime [69]), the drift velocity scales as $(E/p)^{1/2}$. This mobility scaling law leads to a pressure dependent ion dynamics within the sheath and therefore to a different sheath solution than that obtained in the low pressure regime.

Using this ion mobility law, we have obtained analytical expressions for the time average electric potential within the sheath, nonlinear motion of the electron sheath boundary and instantaneous sheath voltage in the moderate range of pressures. Moreover, the Lieberman's collisional single frequency sheath model [70] is regained if we set the high frequency current density to zero.

This chapter is organised as follows: In the next section, we present the two ion transport regimes and the basic model assumptions. In Sec. 4.1, we present, study and solve the analytical model for a dual frequency sheath and obtain the sheath parameters such as the sheath voltage and the electron sheath motion. Finally, in Sec. 3.3, we present solutions of the derived model and compare their solutions and we give our conclusions.

4.1 Basic assumptions and Ion transport regimes

In this section, we discuss the assumptions of the model and the different pressure regimes where different ion dynamics apply in the sheath region. We assume that the transition from the quasi neutral plasma to the zone free of electrons, the instantaneous sheath, occurs on a length on the order of the Debye length, λ_d. Therefore, since for typical conditions the Debye length is much smaller than the sheath width, s_m, we represent the electron density profile by a step function: the electron density falls sharply from $n_e \approx n_i$ at the plasma side of the electron sheath boundary to $n_e = 0$ on the electrode side. With this approximation, the electron density profile is represented by a step function at the electron sheath edge. This step model approximation is known to be reasonably accurate for large sheath voltages [65, 66].

It is then assumed that the electrons respond to the instantaneous electric fields, this is a result of the assumption that the electron plasma frequency greatly exceeds the two RF frequencies $\omega_{pe} \gg \omega_{hf} \gg \omega_{lf}$. This condition is usually valid for dual frequency discharges, since the electron plasma frequency is usually in the gigaHertz range.

In the long ion transit time approximation $2\pi\tau_i^{-1} \ll \omega_{lf} \ll \omega_{hf}$, the ions do not respond instantaneously to the electric field but to the *time averaged electric field* $\bar{E}(x)$ [50]. This strong inequality means that the sheath studied here is capacitive. It should be noted though, as with the collisionless model, that the inequality $2\pi\tau_i^{-1} \ll \omega_{lf}$ will not hold for all situations which are of practical interest. This is particularly true within gases which have low masses, such as hydrogen or helium. Besides these classical assumptions, we now have to discuss the nature of the ion transport within the sheath.

Assuming no recombination or ionization within the sheath, ion particle conservation gives,

$$n_i(x)u_i(x) = n_o u_b, \tag{4.1}$$

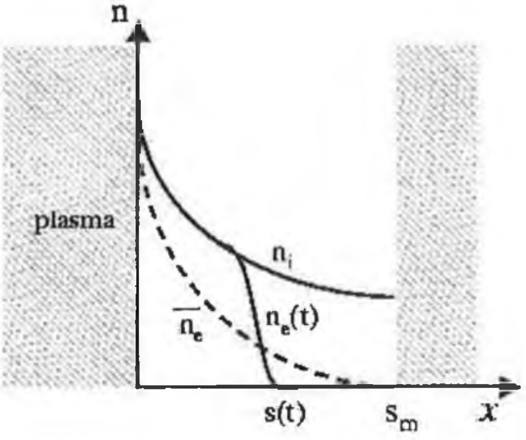

Figure 4.1: Structure of the rf capacitive sheath. $s(t)$ is the electron sheath edge position.

and the momentum conservation equation gives,

$$m_i u_i(x)\frac{du_i}{dx} = e\bar{E}(x) - m_i \sum_p \nu_i^{(p)}(u_i)u_i, \tag{4.2}$$

where, $u_i(x)$ is the ion velocity, $\bar{E}(x)$ the time averaged electric field and $\nu_i^{(p)}(u_i)$ is a *momentum transfer collision frequency* associated with a certain collision processes (p) between the ions and the background gas. In Eq. (4.2), the sum is to be taken over all collisional processes between ions and the background gas which result in momentum transfer. From Eq. (4.2), we can formally identify three regimes: (i) the collisionless case, (ii) the *constant mean free path* case and (iii) the *constant mean collision frequency* case.

At low pressures (referred to Case **I**), when the ion mean free path is large compared to the sheath width, the ion transport is collisionless ("free fall"). In this case, the last term on the right hand side of Eq.(4.2) can be neglected and the equation of motion for the ion reduces to the ion energy conservation equation in the sheath,

$$\frac{1}{2}m_i u_i^2(x) + e\bar{\Phi}(x) = \frac{1}{2}m_i u_b^2, \tag{4.3}$$

where $\bar{E}(x) = -\frac{d\bar{\Phi}}{dx}$ and we have set the value of the electric potential at the Bohm point to zero.

At higher pressure when collisions between ions and the background gas take place, we must consider ion-atom interaction that we shall now discuss in a short digression. For atomic species, ions and atoms interact through three forces: (i) gas kinetic repulsion described by hard elastic sphere collisions, (ii) polarisation attraction, described by a charge-dipole interaction and (iii) a "symmetry" force due to a resonant interaction between ions and atoms. This latter force corresponds to the charge exchange process.

The relative magnitude of these three forces depends on the velocity in the centre of mass frame, v, (here $v \sim u_i$) of the colliding ion and atom. However, it is well established that gas kinetic and charge exchange cross section are independent of this velocity and that the cross section for polarisation interaction is inversely proportional to v. The different behaviour of the cross sections with respect to v lead to different ion dynamics within the sheath.

In principle though, the drift velocity of the ions in the sheath depends not only on of all these processes, but also on the exact shape of the ion distribution function, which can only be obtained through a full kinetic treatment. However, it is possible to identify two limiting cases.

In the intermediate pressure range or high field regime (case **II**), when the energy gained between two subsequent ion-neutral collisions is larger than the ion thermal energy $\sim k_B T_i$, the dominant momentum transfer process is due to charge exchange (cx) and gas kinetic type collisions (k) with the parent gas having a cross section σ_{cx} and σ_k virtually independent of the ion velocity u_i [69]. These two cross sections are usually incorporated into a constant single hard spheres cross section $\sigma = \sigma_{cx} + \sigma_k$. A *constant mean free path model* is therefore appropriate. From Eq.(4.2) and neglecting the inertial term on the left hand side, we obtain the ion velocity as a function of the electric field,

$$u_i(x) = \sqrt{\frac{2e\lambda_i \bar{E}(x)}{\pi m_i}}, \tag{4.4}$$

where the ion mean free path is given by $\lambda_i = (n_g \sigma)^{-1}$. The additional factor $(\pi/2)^{1/2}$ comes from an average over the ion free path distribution [71].

This model is also known as the *variable mobility model* since if we define the mobility as u_i/E, the ion mobility, μ_i, is itself a function of the ion drift velocity u_i,

$$\mu_i(u_i) = \frac{2e\lambda_i}{\pi m_i u_i}. \tag{4.5}$$

For argon, the cross section for charge exchange and kinetic repulsion are equal to $\sigma_{cx} = 5.10^{-15}\text{cm}^2$ and $\sigma_k = 4.2.10^{-15}\text{cm}^2$ so that the ion mean free path is $\lambda_i(\text{cm}) = (300\,\text{p(Torr)})^{-1}$. Note that using this value for the charge exchange collision process in Eq. (4.4) gives rise to a similar value for the drift velocity obtained in [72] and the one calculated with the fit reported in [73].

Finally, we note that a third case could be formally identified at higher pressures (case **III**) when the ion energy gained between two ion neutral collisions is small compared to $k_B T_i$. In this case the dominant collision process is polarisation scattering with a cross section σ_L, know as the *Langevin* or capture cross section [69], which is inversely proportional to the ion neutral relative velocity v. This leads to a *constant collision frequency model* and therefore to a constant ion mobility. The ion drift velocity is then given by,

$$u_i(x) = \frac{e\bar{E}(x)}{m_i \nu_i}, \tag{4.6}$$

where the momentum transfer collision frequency for polarisation is given by [69],

$$\nu_i = n_g \sigma_L u_i = \frac{p}{k_b T_g} \sqrt{\frac{\pi \alpha_p e^2}{\epsilon_o m_i}}, \tag{4.7}$$

where α_p is the polarisability of the argon atom. For argon $\alpha_p = 11.08$ [69], so that the collision frequency is $\nu_i = 2.510^7 \mathrm{p}\ \mathrm{s}^{-1}$ where p is in Torr.

To estimate the pressure range where these three ion dynamics apply, we first compare the ion mean free path to the sheath width. For the case of argon, which we consider here, the ion mean free path is approximately given by $\lambda_i(\mathrm{cm}) = 1/(300\ p(\mathrm{Torr}))$, the collisionless theory is valid when $p\, s_m \lesssim 3.3$ mTorr.cm. The transition between the *constant mean free path model* where $u_i \propto (E/p)^{1/2}$ and the *constant collision frequency model* where $u_i \propto E/p$ is gradual [69, 73]. A critical reduced electric field delimiting these high and low field regimes is obtained by balancing the work done by the electric force between two collisions $eE(x)\lambda_i$ to the ion thermal energy $k_b T_i$, we obtain,

$$\left|\frac{E}{p}\right|_{crit} = \frac{\sigma_{cx} + \sigma_k}{e} \sim 100\ \mathrm{V.cm^{-1}.Torr^{-1}}. \tag{4.8}$$

For typical conditions, the electric field in the sheath can reach value of the order of $10 - 100$ V.cm^{-1} and the transition between the intermediate and high pressure regimes occurs around 200 mTorr. Figure 4.2 summarises, in the (p,E) plane, the validity domain of the three distinct ion dynamic regimes discussed below.

To conclude this section, at low pressure, the ion dynamics are collisionless, whereas above about 10mTorr charge exchange and elastic collisions takes place. Two distinct collisional regimes can be defined: (i) for E/p above $|E/p|_{crit}$, a constant mean free path model applies and the ion drift velocity scales as $(E/p)^{1/2}$; (ii) for moderate E/p below $|E/p|_{crit}$, a variable

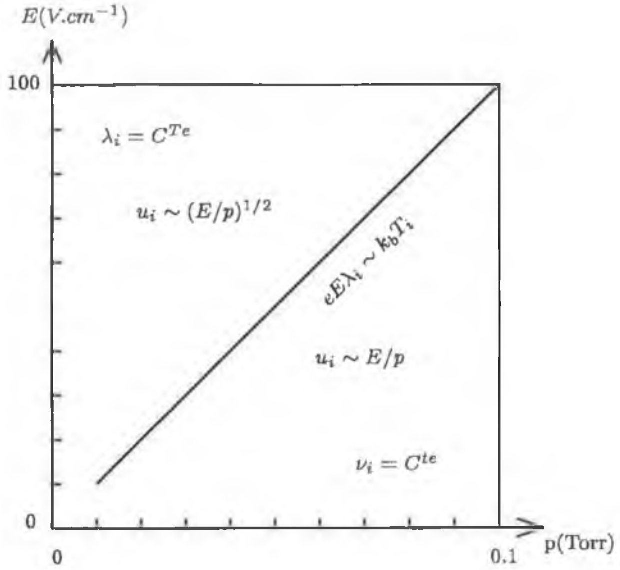

Figure 4.2: Ion transport regime in (p,E) plan

mobility model is valid and the ion velocity scales as E/p. For typical material processing, a variable mobility model is appropriate and we will consider further only the constant mean free path case. Eqs. (4.3) and (4.4) give us the ion dynamic within the sheath for the two pressure regimes considered in this chapter.

4.2 Analytical Model

The derivation which follows in this section is similar to that which was given in the previous chapter, but is outlined here again for the sake of completeness. The sheath structure as depicted in figure (4.1). The electron sheath edge motion is a strongly non linear function of time and is described by the instantaneous sheath position $s(t)$. Ions reach the sheath edge at $x = 0$ with the Bohm velocity u_b and hit the electrodes at $x = s_m$.

The current density, $J(t)$, passing through the sheath is the superposition of two sinusoidal RF current densities,

$$J(t) = J_{lf}\sin(\omega_{lf}t) + J_{hf}\sin(\omega_{hf}t). \tag{4.9}$$

We first consider the ion dynamics in the sheath. The instantaneous electronic charge density, $n_e(x,t)$, can be written as,

$$\begin{aligned} n_e(x,t) &= 0 && x > s(t) \\ &= n_i(x) && x < s(t). \end{aligned} \tag{4.10}$$

such that the charge density is equal to the ion density $n_i(x)$ for $x > s(t)$ and zero elsewhere. The instantaneous electric field $E(x,t)$ is then given by the solution of Poissons equation,

$$\begin{aligned} \frac{\partial E}{\partial x} &= \tfrac{e}{\varepsilon_o} n_i(x) && x > s(t) \\ &= 0 && x < s(t). \end{aligned} \tag{4.11}$$

The instantaneous potential $\Phi(x,t)$ is defined by,

$$\frac{\partial \Phi}{\partial x} = -E(x,t). \tag{4.12}$$

We now time average equations (4.11) and (4.12) to obtain the equation for the time averaged electric field $\bar{E}(x)$,

$$\frac{d\bar{E}}{dx} = \frac{e}{\varepsilon_o}(n_i(x) - \bar{n}_e(x)) \tag{4.13}$$

and the time averaged potential $\bar{\Phi}(x)$,

$$\frac{d\bar{\Phi}}{dx} = -\bar{E}(x), \tag{4.14}$$

where we have defined the time averaged electron density $\bar{n}_e(x)$ as,

$$\bar{n}_e(x) = \frac{\omega_{lf}}{2\pi}\int_{\frac{-\pi}{\omega_{lf}}}^{\frac{\pi}{\omega_{lf}}} n_e(x,t)dt. \tag{4.15}$$

In (4.15), we averaged over a complete low frequency cycle $2\pi/\omega_{lf}$, since this is the longer of the two time scales. As opposed to the single frequency case where the integration in (4.15) can be performed without any approximations [10], the dual frequency case requires an additional assumption. When considering time-averaged quantities, we assume that the HF part of the electric field is small compared to the lf part, because the current in the sheath is displacement current dominated. From charge conservation and Poissons equation, we note that the electric field scales as J/ω. Therefore, the average sheath potential is predominantly affected by the LF part of the current. Since the average electron density is related to the average electric field through the averaged Poisson equation (see (4.13) and (4.14)), $\bar{n}_e$ is also weakly dependent on the HF component of the electric field. As a consequence, if $E_{lf} \sim J_{lf}/\omega_{lf} \gg E_{hf} \sim J_{hf}/\omega_{hf}$, we can introduce as in [60] the phase $\phi(x)$ such that the sheath position $s(t)$ is between 0 and x for $-\phi < \omega_{lf}t < \phi$. Therefore, the integrand in equation (4.15) is zero for $-\phi \leq \omega_{lf}t \leq +\phi$ and equation (4.15) reduces to,

$$\bar{n}_e(x) = n_i(x)\left(1 - \frac{\phi}{\pi}\right). \tag{4.16}$$

To derive an equation for the instantaneous electron sheath motion, we now consider current conservation at the electron sheath edge. In the zone free of electrons, the current is created by the time variation of the electric field (the displacement current) and is equal to the total RF current, Eq.(4.9), whereas in the quasi neutral zone, the current is carried by the motion of the electrons. At the sheath edge $x = s(t)$, this conduction current is nothing other than the ion density $n_i(s)$ times the velocity of the sheath front ds/dt. By balancing the displacement current to the conduction current at the sheath edge, we obtain,

$$en_i(s)\frac{ds}{dt} = J_{lf}\sin(\omega_{lf}t) + J_{hf}\sin(\omega_{hf}t). \tag{4.17}$$

In the single frequency case where $J_{hf} = 0$, the set of equations (4.24), (4.13), (4.14), (4.16) and (4.17) can be solved exactly for the unknown quantities n_i, $\bar{n}_e$, $\bar{\Phi}$, $\bar{E}$ and $s(t)$ [60]. However, for a dual frequency system this is not possible unless we make a simplification, which is explained later. The instantaneous electric field $E(x,t)$ can be obtained by integrating equation (4.11)

$$\begin{aligned} E(x,t) &= \tfrac{e}{\epsilon_o}\textstyle\int_{s(t)}^{x} n_i(x')dx' \qquad && s(t) < x \\ &= 0 && s(t) > x. \end{aligned} \tag{4.18}$$

From equation (4.17), we can then express the integral in equation (4.18) as,

$$\tfrac{e}{\epsilon_o}\textstyle\int_{o}^{s(t)} n_i(x)dx = \tfrac{J_{lf}}{\epsilon_o\omega_{lf}}(1-\cos(\omega_{lf}t)) + \tfrac{J_{hf}}{\epsilon_o\omega_{hf}}(1-\cos(\omega_{hf}t)) \tag{4.19}$$

where we have choose the initial condition $s(0) = 0$. Now according to the equations (4.18) and (4.19), we obtain the instantaneous electric field as follow,

$$E(x,t) = \frac{e}{\epsilon_o}\int_0^x n_i(x)dx - \frac{J_{lf}}{\epsilon_o\omega_{lf}}(1-\cos(\omega_{lf}t)) - \frac{J_{hf}}{\epsilon_o\omega_{hf}}(1-\cos(\omega_{hf}t)), \tag{4.20}$$

for $s(t) < x$ and 0 otherwise. This equation follows from splitting the integral of the ion density from zero to x into two: zero to $s(t)$ and $s(t)$ to x. The result given then follows by substituting terms from (4.18) and (4.19). We must now time average the electric field over a low frequency RF cycle. The time averaged electric field is given by,

$$\bar{E}(x) = \frac{\omega_{lf}}{2\pi}\int_{\frac{-\pi}{\omega_{lf}}}^{\frac{\pi}{\omega_{lf}}} E(x,t)dt. \tag{4.21}$$

In a similar manner to the calculation of the average electronic densities, the integral in Eq. (4.21) can not be performed without approximation. Again, we use the assumption that the HF electric field, which is proportional to J_{hf}/ω_{hf}, is much smaller than the LF component, which is proportional to J_{lf}/ω_{lf}. Hence, we neglect the HF component to calculate the averaged electric field and we consider that the averaged electric field follows the same phase as the averaged electron density. Then, it turns out that the mathematical difficulties of the problem can be greatly reduced while still maintaining the physical content of the model. Thus, inserting (4.20) into (4.21) and neglecting the HF part of the electric field, we find the time averaged electric field,

$$\bar{E}(x) = \frac{J_{lf}}{\epsilon_o \pi \omega_{lf}}(\sin\phi - \phi\cos\phi). \tag{4.22}$$

According to equations (4.12) and (4.22), the average electric field is given by,

$$-\bar{E}(x) = \frac{d\bar{\Phi}}{dx} = -\frac{J_{lf}}{\epsilon_o \pi \omega_{lf}}(\sin\phi - \phi\cos\phi). \tag{4.23}$$

At this stage, we need a representation of the ion density profile as a function of the electric potential. From (4.1) and (4.4) we obtain the ion density as a function of the time averaged potential,

$$n_i(x) = n_o u_b \sqrt{\frac{\pi m_i}{2e\lambda_i \bar{E}(x)}}. \tag{4.24}$$

By substituting these expressions for the ion density profile into (4.17) and set $s = x$ when $\phi = \omega_{lf} t$ (by definition of the phase ϕ), we obtain the following differential equation for the electron sheath motion,

$$\frac{d\phi}{dx} = \frac{u_b}{s_o}\left(\frac{\pi m}{2e\lambda_i}\right)^{1/2} \frac{1}{\bar{E}^{1/2}(\sin\phi + \beta\sin\alpha\phi)}. \tag{4.25}$$

Where we have again introduced an effective oscillation motion amplitude, s_o defined as,

$$s_o = \frac{J_{lf}}{e\omega_{lf} n_o}.$$

The equations (4.23) and (4.25) give us the time evolution of the potential and the sheath edge as a function of the plasma parameters T_e, n_0, the pressure p and the external driving parameters. These two equations can be integrated to determine the sheath potential and the sheath width. It must be stressed out that (4.23) is same as that for a single frequency case, the only difference is in equation (4.25) where the additional terms are proportional to β and describe the high frequency part of the instantaneous electronic sheath motion.

To obtain the sheath motion, we insert the average electric field (4.23) into equation (4.25). After integration, the instantaneous sheath motion is written,

$$\frac{x_{\rm II}}{s_o} = H_{\rm II} \int_o^{\phi} (\sin\xi - \xi\cos\xi)^{1/2} (\sin\xi + \beta\sin\alpha\xi) d\xi, \tag{4.26}$$

where we have used the boundary condition $x(\phi = 0) = 0$ (corresponding to a sheath fully expanded) and we have introduced the following dimensionless parameter $\mathrm{H}_{\rm II}$,

$$H_{\rm II} = \sqrt{\frac{2}{\pi^2} \frac{\lambda_i s_o}{\lambda_D^2}} \tag{4.27}$$

The integral in eq. (4.26) is easily calculated and we have reported in Tab. 4.1 for typical values of α and β. To simplify the discussion in the final section, we recall here the result we obtained in the collisionless approximation,

$$\frac{x_{\rm I}}{s_o} = \int_o^{\phi} d\phi' (\sin\phi'\beta + \sin\alpha\phi') \Bigg(1 + H_{\rm I} \times \tag{4.28}$$
$$\int_0^{\phi'} d\phi'' (\sin\phi'' - \phi''\cos\phi'')(\sin\phi'' + \beta\sin\alpha\phi'') \Bigg),$$

where the parameter $\mathrm{H}_{\rm I}$ is given by,

$$H_{\rm I} = \frac{1}{\pi} \left(\frac{s_o}{\lambda_D} \right)^2$$

Recasting the condition that the HF field is much smaller then the LF field

Table 4.1: Value of the integral in Eq. (4.26)

β α	10	20	30	40	50	60	70	80	90	100
10	3.55									
20	2.79	3.63								
30	2.52	3.09	3.66							
40	2.38	2.81	3.24	3.68						
50	2.30	2.64	2.99	3.34	3.69					
60	2.24	2.53	2.82	3.11	3.40	3.69				
70	2.19	2.45	2.70	2.94	3.19	3.45	3.70			
80	2.17	2.39	2.61	2.82	3.04	3.26	3.48	3.70		
90	2.14	2.34	2.53	2.73	2.92	3.12	3.31	3.51	3.70	
100	2.12	2.30	2.48	2.65	2.83	3.00	3.18	3.35	3.53	3.70

in terms of the two parameters α and β, we obtain the condition $\beta/\alpha \ll 1$ under which the present model is valid.

The time averaged potential, $\bar{\Phi}$, is calculated by dividing eq. (4.23) by eq. (4.25). Using the boundary condition $\bar{\Phi}(x=0)=0$ and integrating over the phase, the time average potential is written as,

$$\frac{\bar{\Phi}}{T_e} = -H_{\mathrm{I}}H_{\mathrm{II}}\int_o^{\phi}(\sin\xi - \xi\cos\xi)^{3/2}(\sin\xi + \beta\sin\alpha\xi)d\xi. \tag{4.29}$$

We obtained previously the same quantity in the collisionless regime,

$$(1-\frac{2\bar{\Phi}}{T_e})^{\frac{1}{2}} = 1 + H_{\mathrm{I}} \times \int_0^{\phi} d\phi(\sin\phi - \phi\cos\phi)(\sin\phi + \beta\sin\alpha\phi). \tag{4.30}$$

As with the integral in eq.(4.26), the integral in eq. (4.29) is easily calculated and we have reported in Tab. II the resulting values for typical α and β.

Equations (4.26) and (4.29) are the two main results of this study and express the electron sheath motion and the time average electric potential

Table 4.2: Value of the integral in Eq. (4.29)

α \ β	10	20	30	40	50	60	70	80	90	100
10	8.28									
20	5.81	8.47								
30	4.95	6.75	8.55							
40	4.51	5.87	7.23	8.59						
50	4.25	5.34	6.43	7.52	8.62					
60	4.07	4.98	5.89	6.81	7.72	8.63				
70	3.94	4.72	5.51	6.29	7.08	7.86	8.64			
80	3.84	4.53	5.22	5.90	6.59	7.28	7.97	8.65		
90	3.76	4.38	4.99	5.60	6.21	6.82	7.44	8.05	8.66	
100	3.70	4.26	4.81	5.36	5.91	6.46	7.01	7.56	8.12	8.67

as a function of the operating conditions (current and frequency of the two driving sources), of the plasma parameters T_e and n_0 and of the gas pressure p. An explicit expression exists for the collisionless solution but contains a large number of terms. For the collisional solution, there is no closed form solution, but a numerical integration is easily achieved with any standard scientific software.

R. N. Franklin found a useful approximate solution [67] for the sheath width and the voltage drop in the collisionless regime. His approach relies on an expansion of the integrand in (4.29) and (4.30) with respect to the frequency ratio α. However, in the collisional regime considered here, such an approach is intractable because of the non-integer power involved in the integrals of (4.26) and (4.29) respectively.

We now consider the two quantities of interest for a global model of a capacitively coupled plasma devices. The sheath width, s_m, and the potential drop, Φ_m, correspond to the maximum values of the two expressions. Depending on the parity of the frequency ratio α, these two quantities are obtained by setting the phase ϕ to π when α is an even number and to a value close to $\pi(1-1/\alpha)$ when α is an odd number. In the final section below, we will consider even frequency ratio to avoid complications when determining s_m and Φ_m.

4.3 Discussion

We have depicted in figures 4.3(a) and 4.3(b) the instantaneous sheath width $x(\phi)$ versus half a low frequency cycle for the collisionless and collisional case, respectively for the following operating conditions: $\omega_{lf}/2\pi = 1\,\mathrm{MHz}$, $\omega_{hf}/2\pi = 51\,\mathrm{MHz}$, $J_{lf} = 2\,\mathrm{A.m^{-2}}$ and $J_{hf} = 20\,\mathrm{A.m^{-2}}$. Plasma parameters are $T_e = 3\,\mathrm{eV}$ and $n_0 = 2.10^{15}\,\mathrm{m^{-3}}$ and the background gas density is 100 mTorr. We observe the same qualitative behaviour for both curves; that is a non linear low frequency sheath edge motion modulated by the high frequency part of the electron oscillation. However, we observe that ion-neutral collisions in the sheath leads to a smaller sheath thickness $s_m = x(\pi)$: at 100 mTorr, the sheath width is about 2.5 mm, about one third of the sheath width predicted by the collisionless model.

Figures 4.4 compare the sheath width s_m as a function of the edge density n_0 obtained by the collisional model (dotted line) and the collisional solution (solid line) for 1, 10 and 100 mTorr, respectively. We see that at 1 mTorr for which the ion mean free path is about 3 cm, the collisional solution (solid curve) overestimates the sheath thickness obtained from the collisionless model (dotted curve). This overestimation is easily understood

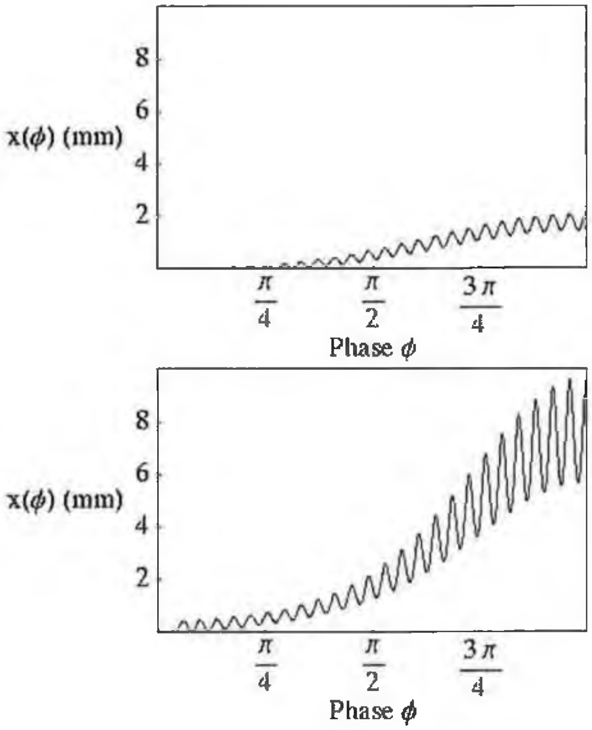

Figure 4.3: Instantaneous sheath motion versus phase. Parameters are as follows: $\alpha = 51$, $\beta = 10$, $J_{lf} = 2\text{A.m}^{-2}$, $T_e = 3\text{eV}$ and $n = 2.10^{15}\text{m}^{-3}$; Upper figure is the collisionless solution and bottom figure is for the collisional solution with $p = 100\text{mTorr}$

if we note that the sheath width scales as the minus half power of the pressure (4.27). When we increase the pressure, both solutions are closer to each other. Finally at a higher pressure $p = 100\,\mathrm{mTorr}$, the collisionless solution overestimates the collisional solution by about an order of magnitude.

Figures 4.5 display the potential drop, Φ_m, for the same operating and plasma conditions. We observe the same conclusion as for the sheath width: as the pressure increase from 1 to 100 mTorr, the collisionless solution overestimates the potential drop. For example, at 100 mTorr and for a plasma edge density equal to 2.10^{15} m^{-3}, the collisionless model predicts 256 V for the potential drop, about ten time larger than the value predicted by the collisional model 23 V (we have set T_e to 3 eV).

As a matter of example, we have plotted on figures (4.6) and (4.7) respectively the sheath width and the sheath potential in the collisional case, versus the edge plasma density at 100 mTorr for three values of the frequency ratio $\alpha = 21, 51$ and 81. The decreasing behaviour of these two quantities with respect to the edge density reflects the fact that as the edge density increase, a smaller potential drop is required to balance the electron flux and the ion flux. More interesting is the behaviour of s_m and Φ_m with respect to the frequency ratio α. A perfect HF/LF decoupling would result in a single curve since in this case the voltage drop is independent of the high frequency drive. We see that as the frequency ratio increases, both the sheath width and the potential drop tends to a limiting curve. Indeed, curves corresponding to $\alpha =$ 51 and 81 are close together. We also note the sheath width and the potential drop for the case of $\alpha = 21$ differs by about a few tens of percent rather than those obtained at $\alpha = 51$ and 81.

Therefore, we conclude that as for the collisionless capacitive DF sheath the high frequency modulation of the sheath motion leads to some significant

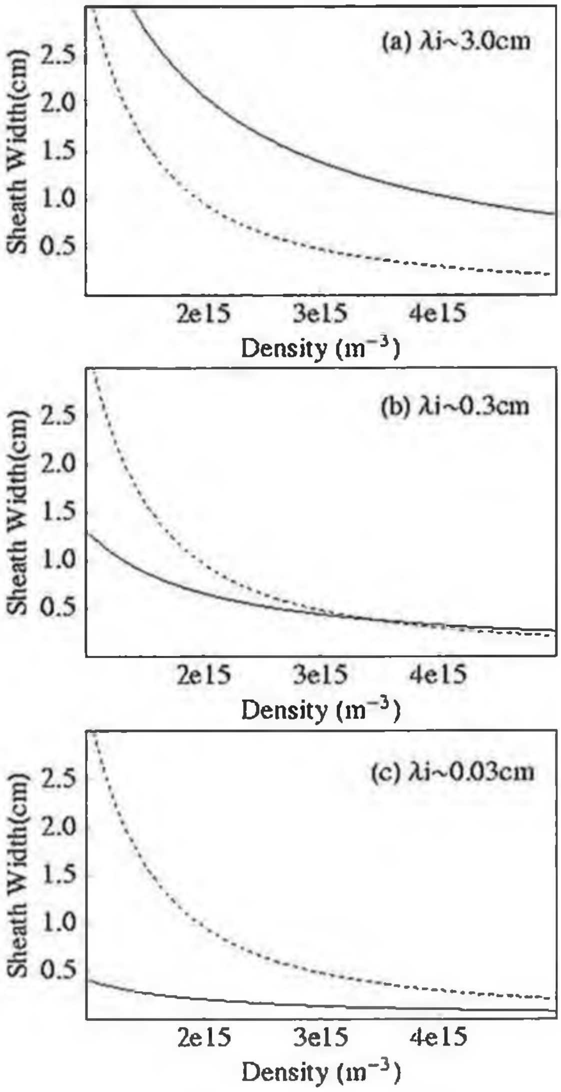

Figure 4.4: Sheath width s_m (in mm) versus plasma density for three pressures, 1 mTorr, 10 mTorr and 100 mTorr. Solid curve correspond to the collisional solution and dotted curve to the collisionless solution.

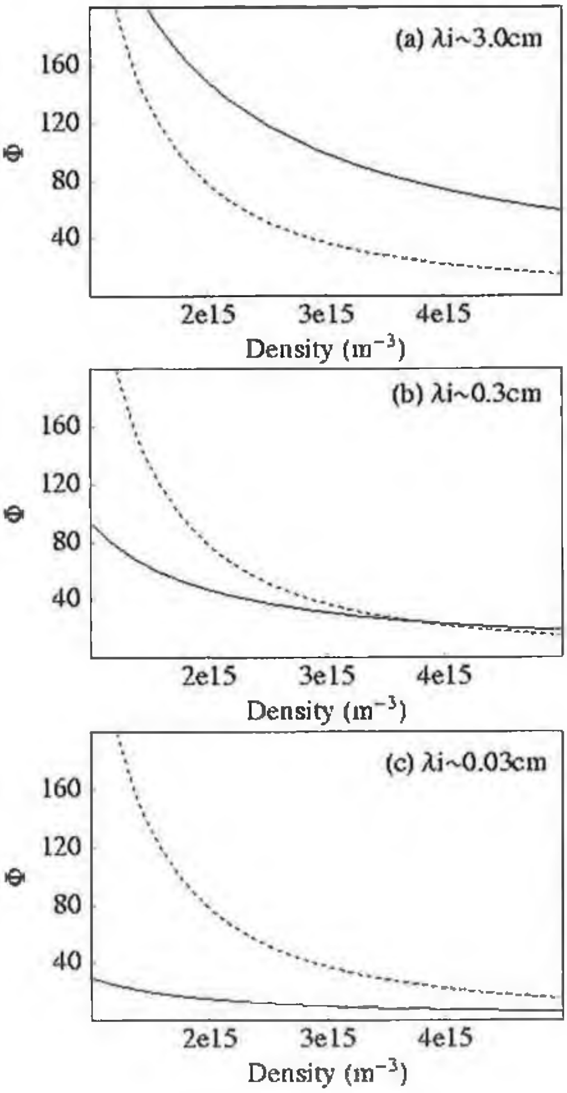

Figure 4.5: Potential drop Φ_m (normalised to T_e) versus plasma density for three pressures, 1 mTorr, 10 mTorr and 100 mTorr. Solid curve correspond to the collisional solution and dotted curve to the collisionless solution.

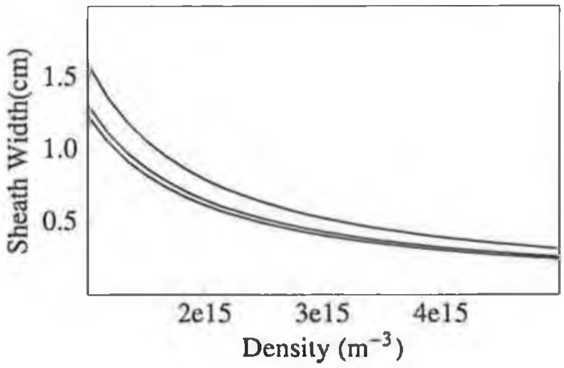

Figure 4.6: The sheath width versus the *peak* density at 10 mTorr for the following parameters $\beta = 10$, $J_{lf} = 2\,\text{A.m}^{-2}$, $T_e = 3\,\text{eV}$. Upper, intermediate and lower curves correspond to a frequency ratio equal to 21, 51 and 81, respectively

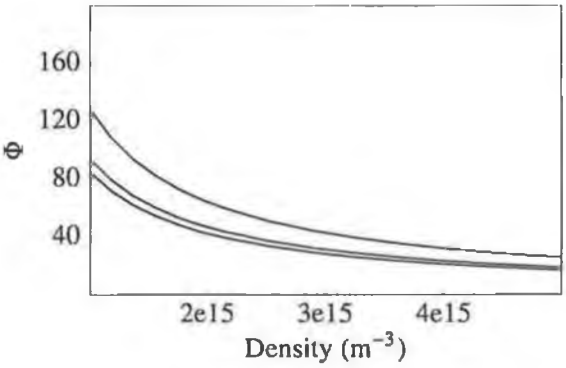

Figure 4.7: Potential drop Φ_m versus the *peak* density at 10 mTorr for the following parameters $\beta = 10$, $J_{lf} = 2\,\text{A.m}^{-2}$, $T_e = 3\,\text{eV}$. Upper, intermediate and lower curves correspond to a frequency ratio equal to 21, 51 and 81, respectively

deviation from a perfect HF/LF decoupling when the frequency ratio is not large enough. This model predicts the frequency ratio and current ratio dependence of both the sheath width and sheath potential. This model has been then compared to a previously developed dual frequency sheath model, which is valid in the collisionless regime, finding as expected, significant deviation between the two models. Expression (4.26) and (4.29) give the maximum sheath width and sheath voltage and could provide some useful values for a global modelling of the dual frequency capacitive discharges.

CHAPTER 5

Two dimensional Electromagnetic PIC

Motivated by a recently developed theoretical model which indicates that Magnetic effects within plasma devices may be more important than was perhaps previously thought [58], and also experimental evidence that the radial uniformity of the plasma density varies significantly when a device is operated with two separate frequencies [13, 14] as a result of electromagnetic effects [58, 74]; a two dimensional Electromagnetic PIC simulation has been developed in order to study these characteristics. The implementation of the PIC algorithm which is described here is that of a two dimensional Electromagnetic scheme. The geometry of the device is shown in figure 5.1. The simulated device is asymmetric, meaning that the area of the powered and grounded electrodes are not equal.

The complete set of Maxwells equations are solved so that the equation

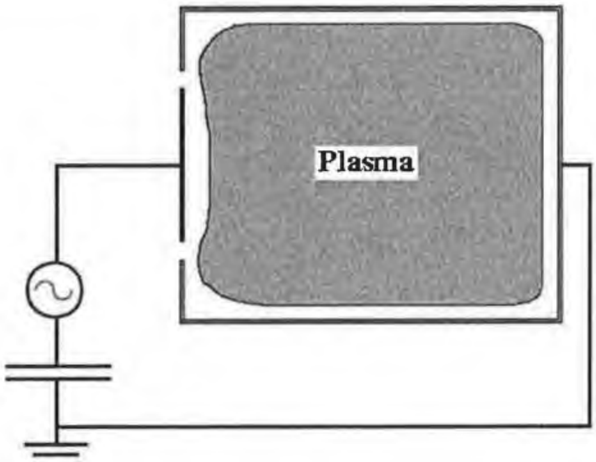

Figure 5.1: PIC Geometry

of motion for the i^{th} particle is given by Lorentz's equation,

$$m\frac{d^2x_i}{dt^2} = q(\mathbf{E} + \mathbf{v} \times \frac{\mathbf{B}}{c}). \tag{5.1}$$

Where **E**, **B** and **v** represent the Electric field, Magnetic field and the particle velocity respectively. It should be noted that, for simplicity, in this chapter we have expressed Maxwells equations in Heaviside-Lorentz units. For an Electrostatic PIC simulation the following two stability conditions apply, if the equations are finite differentiated explicitly, in order for the algorithm to be stable and produce physically accurate results,

$$\omega_{pe}\Delta t < 2, \tag{5.2}$$

$$\frac{\Delta x}{\lambda_d} < 2. \tag{5.3}$$

If either of these two conditions is violated then the equations become unstable and results in non-physical heating of the electrons within the plasma, with the outcome that the algorithm will not produced reliable results [37]. Within an Electromagnetic simulation there is a third stability condition that must be adhered to, this is the Courant condition, given by,

$$\frac{c\Delta t}{\Delta x} < 1. \tag{5.4}$$

This condition essentially states that the velocity of light must be resolved within a single spatial cell. If this condition is not fulfilled, then there results in non-physical Electromagnetic waves being generated within the plasma making the simulation unstable and the results are unreliable. Within Electromagnetic simulations, the third of these conditions is by far the most stringent. It can be approximately two orders of magnitude more stringent than the other two. It should be noted that these stability conditions are valid only for equations which are explicitly finite differenced.

These stability conditions may be removed by differentiating the field equations implicitly. When this is done only the following accuracy condition remains,

$$\frac{v_t \Delta_t}{\Delta_x} \lessapprox 2. \tag{5.5}$$

Where, v_t is the thermal velocity of the electrons given by, $\sqrt{k_b T_e / m_e}$. This condition reasonably states that most of the particles must not move a greater distance that the dimensions of a single spatial cell within a single time step. Although implicit particle codes have the advantage that there are no stability conditions, they are not ideal. Implicit codes suffer from the disadvantage that they may have extremely complex boundary conditions. This stems from the particle dynamics and the field equations being solved simultaneously. For example, particle deletion or emission at a surface depends on the electric field, so therefore the particle boundary conditions enter into the field equations.

The fundamental differences between an implicit and explicit method of solving the equations can be summarised as follows. In an explicit algorithm one can be certain that the results obtained are physically correct. In order to achieve this certainty, one must adhear to strict stability conditions. Whereas in an implicit algorithm, one can not be certain the the results are physically correct but there are no restrictive stability conditions.

Because of these reasons we have implemented a semi-implicit method of solving the field and particle equations. The field equations are solved implicitly and then the equations of motion are solved explicitly. This has the effect of removing the third stability condition, equation 5.4, whereas the first two stability conditions remain. It also has the advantage of removing the difficulty of including the particle boundary conditions within the field solver which occurs in purely implicit codes.

5.1 Particle Weighting

Within a PIC code, the real particles are replaced by weighted super particles. Each of these super particles represents in a two dimensional code on the order of 10^4 to 10^5 real particles, with all physical properties scaled appropriately. The precise value of the particle weighting is a variable that is chosen to be large enough to reduce computational expense while at the same time being small enough to minimise computational noise. It is found that an average of 100 super particles per spatial cell is a good trade off between accuracy and expense. For a quite modest grid size of 100×100, this requires approximately one million super particles to be simulated. Each of these super particles have two positional coordinates and three velocity components. This means that the simulation is what is often called a $2d - 3v$ implementation. These super particles are then, initially, randomly distributed throughout the spatial grid with a Maxwellian velocity distribution at an appropriate temperature.

5.1.1 Particle Weighting

Once all the particle positions and velocities have been calculated it is necessary to transfer the particle weights onto a spatial grid. The weight from each particle is distributed onto the grid in the following manner

$$X_{i,j} = \sum_{s} Q(x_{i,j}). \tag{5.6}$$

Where, s is the summation index over the super-particles and Q is the weighting kernel given by

$$Q(X_{i,j}) = \begin{cases} x_{i,j} & = & r_x r_y \\ x_{i+1,j} & = & (1 - r_x) r_y \\ x_{i,j+1} & = & r_x (1 - r_y) \\ x_{i+1,j+1} & = & (1 - r_x)(1 - r_y) \end{cases}$$

Where, $r_{x,y}$ represent the fractional part of the particle position in both coordinates. From this kernel it is evident that the particle densities are weighted at the corner of the grid cells as is illustrated in figure 5.2. The weighting kernel described here essentially ascribes the density linearly to the next four nearest grid points. This smoothes the particle density at each point and results in the particle densities being less noisy. It is possible to use other weighting schemes; although it is considered that a linear weighting results in the best trade of between computational expense and accuracy [37].

5.1.2 Charge Assignment

Once the particle densities have been assigned to the grid points it is then necessary to obtain the charge densities at each of the cell points. The charge

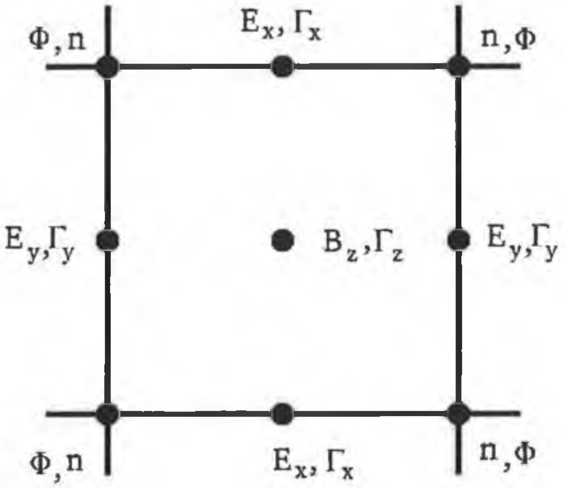

Figure 5.2: Spatial layout of the particle and field quantities on a yee mesh.

density at each grid point is given by

$$\rho_{i,j} = \sum_{s,k} q_s X_{i,j}. \tag{5.7}$$

Where, s is the summation index for particle species and k is the summation index for super-particles. $X_{i,j}$ then gives the position of each particles. The charge density is allocated to the grid with a zeroth order weighting kernel, this is because the density has already been allocated by a linear weighting kernel to the next four nearest grid points linearly. This charge density is then used to calculate the electric potential throughout the plasma.

5.1.3 Current Assignment

Maxwells equations are coupled to the particle dynamics through the charge density and the current density in equations (5.9), and (5.12) respectively. It is therefore necessary to calculate the current densities from the particles.

The current at a given point is given by

$$J_{i,j}^{n+\frac{1}{2}} = \Sigma_{s,k}\tilde{q_s}\tilde{n_s}v(i,j)_k^{n+\frac{1}{2}}, \tag{5.8}$$

where $\tilde{q}$ and $\tilde{n}$ represents the weighted particle charge and particle number respectively, the superscript then enumerates the time level.

5.2 Solution of the Field Equations

The complete set of Maxwells equations is given by the following,

$$\begin{aligned} \nabla \cdot E &= \rho, & (5.9)\\ \nabla \cdot B &= 0, & (5.10)\\ \nabla \times E &= -\frac{1}{c}\frac{\partial B}{\partial t}, & (5.11)\\ \nabla \times B &= \frac{J}{c} + \frac{1}{c}\frac{\partial E}{\partial t}. & (5.12) \end{aligned}$$

At this stage in our algorithm we have calculated the charge and current densities throughout the spatial grid. We now come to the solution of the field equations. In order to calculate the fields we solve the complete set of Maxwell equations. Our stratagem for solving these equations is to separate the field equations into two distinct sections. First, we calculate out the electric field, from the charge densities, by solving equation 5.9. We then use the Electric fields just obtained by solving Poissons equation as a first guess to the actual fields obtained by solving equations 5.11 and 5.12.

In principle only two of the four Maxwell equations need be solved subsequent to having solve Poissons equation initially, those being the curl equations. This of course assumes that the system is in a static situation initially. Since it can easily be shown that if they are satisfied at an initial time, then they are satisfied at all subsequent times, i.e. Maxwells equations are time independent. In practice this is not true since we are solving a finite differenced approximation to the differential equations. It is therefore necessary to correct the electric fields after each time step in order to ensure that Gauss' law is enforced, the method used to achieve this described later.

5.2.1 Poissons Equation

As a first guess for the electric fields in the complete solution of Maxwells equations and also within the divergence correction algorithm, described later, we calculate out the solution of Poissons equation, given by,

$$\nabla^2 \Phi = -\rho, \tag{5.13}$$

in order to obtain the electric potential. In two dimensions this equation is explicitly finite differenced into the following form,

$$\frac{u_{i+1,j} - 2u_{i,j} + u_{i-1,j}}{\Delta x^2} + \frac{u_{i,j+1} - 2u_{i,j} + u_{i,j-1}}{\Delta y^2} = -\rho_{i,j}. \tag{5.14}$$

In order to solve this, we again employ an Alternating Direction Implicit method (ADI). The precise algorithm is called the 'Peaceman-Rachford method' [75]; although this is not the most efficient method of solving two dimensional elliptical equations, it is a good trade off between complexity and efficiency. ADI methods also have the advantage that there are no restrictions on the number of cell points that are required, such as occur in more efficient methods. For example, in the Buneman cyclic reduction method and the related FACR method [76], which are the most efficient methods, the number of cell points has to be a power of 2. This greater flexibility on choosing the number of spatial cells can actually reduce the total computational time necessary to reach a steady state under many conditions.

Poissons equation is then rewritten in the form, $L\phi = \bar{\rho}$, where L is a matrix representing the finite differenced operator, ∇^2 and $\bar{\rho} = \rho\Delta^2_{x,y}$, where the subscript means either x or y. Thus, to obtain a solution of Poissons equation, the following equations are iterated until the solution is obtained to the desired accuracy.

$$[\nabla_y^2 + r_1\mathbf{1}]\Phi^{n+\frac{1}{2}} = -[\nabla_x^2 - r_1\mathbf{1}]\Phi^n + \rho, \tag{5.15}$$

$$[\nabla_x^2 + r_2\mathbf{1}]\Phi^{n+1} = -[\nabla_y^2 - r_2\mathbf{1}]\Phi^{n+\frac{1}{2}} + \rho. \tag{5.16}$$

Where r_1 and r_2 are the ADI time steps.

Once the electric potential has been calculated, the necessary electric fields are obtained as follows,

$$E_{x_{i+\frac{1}{2},j}} = \frac{\Phi_{i-1,j} - \Phi_{i+1,j}}{2\Delta_x}, \tag{5.17}$$

$$E_{y_{i,j+\frac{1}{2}}} = \frac{\Phi_{i,j-1} - \Phi_{i,j+1}}{2\Delta_y}. \tag{5.18}$$

This is a second order accurate method of obtaining the electric fields. It should be noted, that obtaining the Electric fields in this manner results in the grid dimensions of the two electric field components being different. The dimension for the Electric field in the x direction is $(N-1) \times N$ and in the y direction is $N \times (N-1)$, where N is the number of spatial cells in each direction, see figure 5.2.

5.2.2 Solution of Electromagnetic Equations

Having just obtained the electric fields we now proceed to solving the two Maxwell curl equations, although we solve a slightly modified set of curl equations. In order to control the creation of high frequency radiation caused by simulation noise, it was proposed that the set of Maxwells equations be modified to damp the high frequency radiation modes that develop [77]. Motivated by the equation for exponential decay $f + \tau df/dt = g$, the following modifications to the curl equations are implemented:

$$\nabla \times [(1+\tau_1\frac{\partial}{\partial t})E] = -\frac{1}{c}\frac{\partial B}{\partial t}, \tag{5.19}$$

$$\nabla \times [(1+\tau_2\frac{\partial}{\partial t})B] = \frac{1}{c}J + \frac{1}{c}\frac{\partial E}{\partial t}. \tag{5.20}$$

Where, $\tau_{1,2}$ are damping coefficients chosen to obtain the desired noise reduction properties. This modification has the advantage of being trivial to implement when the equations are implicitly finite differenced, as will be seen later. In order to solve these equations we employ an Alternating Direction Implicit method (ADI). The idea behind the ADI method is that an operator, L, can be split into two parts

$$L = L_x + L_y.$$

The ADI algorithm first solves for the quantities in one given direction, such as for L_x, then solves for quantities in the other direction using quantities just obtained from the solution of L_x. Once this is done, a convergence test is applied to the solution and if the solution is within a given tolerance then the algorithm is stopped, otherwise the algorithm is repeated.

As mentioned earlier, we wish to avoid the constraints of the Courant condition, therefore using the Crank-Nicholas method,[1] the modified curl equations are implicitly finite differenced into the following matrix form,

$$[\hat{1} + M_+]\begin{bmatrix} Ex \\ Ey \\ Bz \end{bmatrix}^{n+1} = [\hat{1} - M_-]\begin{bmatrix} Ex \\ Ey \\ Bz \end{bmatrix}^{n} - \frac{\Delta t}{\epsilon}\begin{bmatrix} Jx \\ Jy \\ 0 \end{bmatrix}^{n+\frac{1}{2}} . \tag{5.21}$$

---

[1] The Crank-Nicholas implicit method of finite differencing is described in numerous texts, such as Numerical Recipes [78].

Where, $\hat{1}$ is the identity matrix and $M_{\pm}$ is a matrix given by

$$M_{\pm} = \begin{bmatrix} 0 & 0 & -\frac{c\Delta t}{2\Delta_y}(1 \pm 2d_2)\hat{\partial}_y \\ 0 & 0 & \frac{c\Delta t}{2\Delta_x}(1 \pm 2d_2)\hat{\partial}_x \\ -\frac{c\Delta t}{2\Delta_y}(1 \pm 2d_1)\hat{\partial}_y & \frac{c\Delta t}{2\Delta_x}(1 \pm 2d_1)\hat{\partial}_x & 0 \end{bmatrix}. \tag{5.22}$$

And where $\hat{\partial_{x,y}}$ represent the finite differencing of the field quantity in the direction indicated by the subscript and $d_{1,2} = \tau_{1,2}/\Delta t$. For $d_1 = d_2 = d = \frac{1}{2}$ the method is equivalent to a full implicit differentiation of the unmodified Maxwells equations, $d = -\frac{1}{2}$ represents an explicit differentiation of the unmodified equations.

In order to solve equation 5.21 we again employ an ADI scheme. In the 2-d Cartesian model, the problem may be expressed as:

$$[\hat{A}_x + \hat{A}_y] \begin{bmatrix} Ex \\ Ey \\ Bz \end{bmatrix} = \begin{bmatrix} Sx \\ Sy \\ Sz \end{bmatrix} \tag{5.23}$$

or more compactly as:

$$[\hat{A}_x + \hat{A}_y][\Psi] = [S]. \tag{5.24}$$

Where S corresponds to the rhs of equation 5.21 and represents the solution of the field equations at the previous time step and $\hat{A}_x$ and $\hat{A}_y$ are given by,

$$\hat{A}_x = \frac{1}{2} \begin{bmatrix} 1 & 0 & 0 \\ 0 & 1 & \frac{c\Delta t}{2\Delta_x}(1 \pm 2d_2)\hat{\partial}_x \\ -\frac{c\Delta t}{2\Delta_y}(1 \pm 2d_1)\hat{\partial}_y & & 1 \end{bmatrix}, \tag{5.25}$$

and

$$\hat{A}_y = \frac{1}{2} \begin{bmatrix} 1 & 0 & -\frac{c\Delta t}{2\Delta_y}(1 \pm 2d_2)\hat{\partial}_y \\ 0 & 1 & 0 \\ -\frac{c\Delta t}{2\Delta_y}(1 \pm 2d_1)\hat{\partial}_y & 0 & 1 \end{bmatrix}. \tag{5.26}$$

The ADI algorithm them performs the following iteration until Ψ converges

- Compute $Q1 = (\hat{1} - r\hat{A}_y)\Psi + rS$
- Solve $(\hat{1} + r\hat{A}_x)\Psi = Q1$
- Compute $Q2 = (\hat{1} - r\hat{A}_x)\Psi + rS$
- Solve $(\hat{1} + r\hat{A}_y)\Psi = Q2$.

Where in the above r represents the ADI iteration time step. The ADI algorithm for the solution of the field quantities Ψ is then as in figure 5.3.

When an electric field with the correct divergence is supplied as the initial guess for the real electric field by solving Poissons equations, the above ADI algorithm usually solves to a desired accuracy within two iterations.

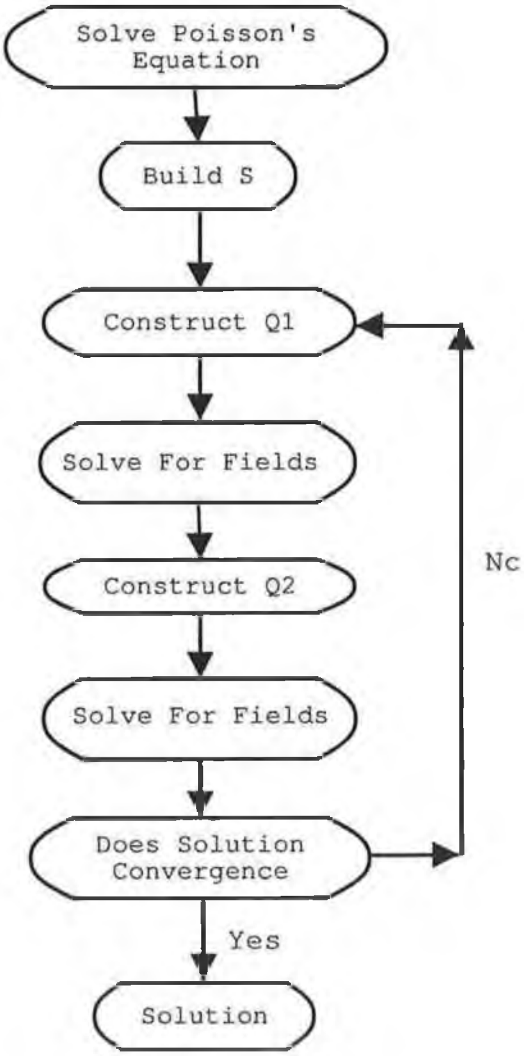

Figure 5.3: ADI Algorithm for the solution of the field quantities given by Ψ.

5.2.3 Divergence Correction

As mentioned above, Maxwells equations are time independent, that is, once they are solve initially then they are valid at all subsequent times. It is unnecessary to solve the two elliptical equations subsequently. While this is true in principle if the equations are solved exactly, using the method discussed above does not solve the equations exactly, but a finite differenced approximation to the exact solution. This results from microscopic inconsistencies between the current density and the charge density due to the use of the mesh and weights. With the consequence that Gauss' law $\nabla \cdot \mathbf{E} = \rho$ may not be satisfied. It is therefore necessary to implement a method which solves Maxwells curl equations while at the same time ensuring that the divergence of the electric field remains correct.

In order to satisfy Gauss' law we implement a correction to the electric field of the form

$$\mathbf{E'} = \mathbf{E} - \nabla\delta\phi.$$

Such that

$$\nabla \cdot \mathbf{E'} = \rho,$$

which means that

$$\nabla \cdot (\mathbf{E} - \nabla\delta\phi) = \rho.$$

Thus we require a Poisson solution for $\delta\phi$ which can be found by solving

$$\nabla^2\delta\phi = \nabla \cdot \mathbf{E} - \rho. \tag{5.27}$$

This correction, due to Boris [79], is computationally convenient since under these conditions, i.e, a square grid, Poissons equation can be rapidly solved. The method used to solve Poissons equation is described next.

5.3 Moving Particles

In order to calculate the acceleration of the particles caused by the Electromagnetic fields, the Lorentz equation is solved,

$$m\frac{d\mathbf{v}}{dt} = q(\mathbf{E} + \mathbf{v} \times \frac{\mathbf{B}}{c}) \tag{5.28}$$

This equation is then explicitly time centred differenced into the following form,

$$\frac{v_{t+\Delta t/2} - v_{t-\Delta t/2}}{\Delta t} = \frac{q}{m}(\mathbf{E} + \frac{\mathbf{v}_{t+\Delta t/2} - \mathbf{v}_{t+\Delta t/2}}{2} \times \frac{\mathbf{B}}{c}). \tag{5.29}$$

In order to solve this equation, we employ the Boris push method [80, 81]. The procedure for solving this equation is as follows, First one half of the Electric impulse is applied to the particle and v^- is calculated,

$$v_{t-\Delta t/2} = v^- - \frac{qE}{m}\frac{\Delta t}{2}. \tag{5.30}$$

Then the rotation caused by the Magnetic field is calculated by finding v^+,

$$\frac{v^+ - v^-}{\Delta t} = \frac{q}{2m}(v^+ + v^-) \times B/c. \tag{5.31}$$

Once the rotation is calculated, the final half of the electric impulse is added to the initial velocity to determine $v_{t+\Delta t/2}$,

$$v_{t+\Delta t/2} = v^+ + \frac{qE}{m}\frac{\Delta t}{2}. \tag{5.32}$$

Once $v_{t+\Delta t/2}$ has been calculated, the particles are moved into their new positions.

5.4 Monte Carlo Collisions

The plasma chemistry may be of extreme importance with a given discharge. However within PIC simulations it is extremely difficult to model the plasma chemistry efficiently. The reasons for this are twofold. The first is that integration of the full plasma chemistry into a PIC simulation would radically increase the number of simulated species, this would result in the computational expense being prohibitively high. The reason for this increase is predominately due to the vast increase in the number of super particles that are required. This is because there should be a minimum number of super particles per cell in order for the algorithm to reproduce reliable results. The number of particles per cell should be > 50 of each species. Less that this number of particles results in the calculated quantities being excessively noisy. The second problem with modelling the plasma chemistry is more fundamental. A great deal of the information that is required in order to simulate the chemistry is simply not available, such as collisional cross sections and decay rates.

In order to attempt to overcome these problems, various restrictions to the type of plasmas which are simulated must be adhered to. First we only attempt to simulate noble Gases, in this case argon, for these gases don't form molecules and therefore the number of species is limited. For example, an Argon discharge can be realistically simulated by using as few as three species. We also limit our attempt to simulate the plasma by restricting ourselves to the particle reactions that have the greatest cross-sections. For the results presented throughout this thesis, three types of particles are simulated, electrons, singly positively charged Ar ions and the neutral background gas. An additional reason for simulating Argon is that the collisional cross sections are extremely well known for this gas. The complete list of collisional mechanisms that are taken into account are given in the following table.

Mechanism	Process	Threshold Energy (eV)
Elastic	$e + Ar \rightarrow e + Ar$	0
Inelastic	$e + Ar \rightarrow e + Ar*$	11.6
Inelastic	$e + Ar \rightarrow e + Ar*$	13.1
Ionisation	$e + Ar \rightarrow e + Ar^+ + e$	16.0
Elastic	$Ar^+ + Ar \rightarrow Ar^+ + Ar$	0.0
Charge Exchange	$Ar^+ + Ar \rightarrow Ar + Ar^+$	0.0
Inelastic	$Ar^+ + Ar \rightarrow Ar^+ + Ar*$	23.6

The cross-section for these process are then shown in figure 5.4 and figure 5.5 and are taken from [82–84].

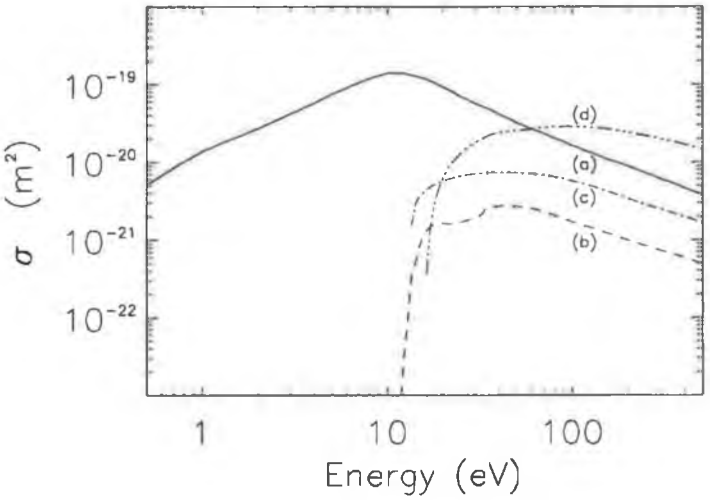

Figure 5.4: Cross-section data for Electron - Neutral collisions. a,b,c and d refer to elastic, inelastic(11.6), inelastic(13.1) and ionisation cross-sections respectively.

After the particles are pushed, as described in the previous section, a certain number of the particles are chosen to undergo a collision through

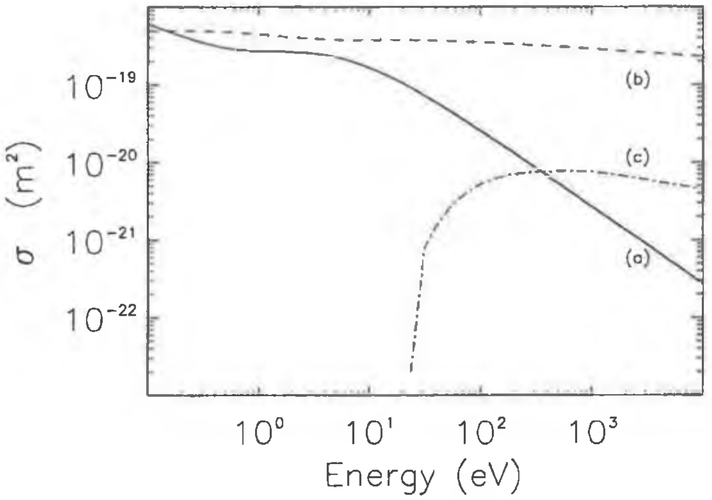

Figure 5.5: Cross-section data for Ion - Neutral collisions. a,b and c refer to elastic, charge exchange and inelastic cross-sections respectively.

the application of a Monte Carlo Collision algorithm. Firstly, a cumulative collisional probability is calculated for each of the reactant species depending on their velocities and their collisional cross-sections. This cumulative collisional probability is taken as the sum over all the collision probabilities for all the collision processes. Then a random number is produced, if the random number is less than the collision probability then there occurs a collision; if not then no collision occurs and the particle is unaffected.

Once it has been determined that a particle will experience a collision, then the type of collision must be chosen. To do this we produce a weighted random number, weighted to the cumulative collision probability. We then determine which collision cross-section is nearest to this random number. This collision process in then chosen to occur. Upon the collision, the particles velocity is modified appropriately and additional particles are either added or removed depending on the collision process [85]. For anisotropic collision processes, the scattering angles of Simko are used [86].

5.5 Boundary Conditions

Here we describe the boundary conditions that must be applied to the field equations and boundary conditions for particle interactions with the surfaces.

5.5.1 Electrode

The necessary Maxwell equations for the fields on the electrode are given by

$$\frac{1}{c}\frac{\partial B_z}{\partial t} = \frac{\partial E_x}{\partial y}, \tag{5.33}$$

$$\frac{1}{c}\frac{\partial E_x}{\partial t} = \frac{\partial B_z}{\partial y} - \frac{1}{c}J_x, \tag{5.34}$$

$$\frac{\partial E_x}{\partial x} = \rho. \tag{5.35}$$

These equations are valid if we assume a perfectly conducting electrode, which is reasonably valid if the electrode is made from metal. The first two of these equations are then Crank-Nicholas finite differenced into the following form,

$$B^{n+1}_{z_{i+\frac{1}{2}}} - B^{n}_{z_{i+\frac{1}{2}}} = K\left[(E^n_i - E^n_{i+1}) + (E^{n+1}_i - E^{n+1}_{i+1})\right], \tag{5.36}$$

$$E^{n+1}_i - E^n_i = K\left[(B^n_{z_{i-\frac{1}{2}}} - B^n_{z_{i+\frac{1}{2}}}) + (B^{n+1}_{z_{i-\frac{1}{2}}} - B^{n+1}_{z_{i+\frac{1}{2}}})\right] - \Delta t J, \tag{5.37}$$

where,

$$K = \frac{c\Delta t}{2\Delta y}. \tag{5.38}$$

The first two of these field equations can then be easily solved simultaneously when rewritten as a single tridiagonal matrix.

One is then left with the problem of imposing Gauss' law on the solution. It is though, impossible to implement a divergence correction algorithm as was done for the equations for the bulk plasma. This is because it is necessary to obtain the electric field on the boundary before solving the equations for the bulk plasma. But the equations written above for the electrode are themselves coupled to the equations for the interior of the bulk plasma through Gauss' law.

In order to overcome this problem of having a correct divergence of the electric field on the electrode it would be necessary to solve the equations for both the electrode and the bulk plasma simultaneously. While it would be technically possible to achieve this, it would be prohibitively expensive computationally to do so. There is also a second problem with solving the field equations for the electrode, particularly concerning the charge density on the electrode. Any charged particles that impact and get absorbed by the electrode, affects the local surface charge density on the electrode. In order to take into account the distribution of this charge density on the electrode it would be necessary to self consistently solve for the dynamics of these particles within the electrode. This is itself a non-trivial task. Because of these difficulties it was decided to make the assumption that the electric potential across the electrode should be uniformly distributed. In order to do so the method of Vahedi et. al. was implemented [87, 88].

The equation we solve for the voltage on the electrode is

$$\sigma = \frac{1}{\Delta x}(\phi_0 - \phi_1) = \rho_0 \frac{\Delta_x}{2}. \tag{5.39}$$

The surface charge density is then related to the discharge current by

$$\frac{d\sigma}{dt} = J. \tag{5.40}$$

The above equation can not be solved as it is currently written, since the voltage on the electrode is related to the potential produced by the charge density in the plasma itself. It would be necessary to iterate the above equations with the solution of Poissons for the bulk plasma. It is possible though to decouple the above equations from Poissons equation which eliminates the necessity to iteratively solve the equations. To do this we rewrite Poissons equation as

$$\phi_{i,j} = \phi_{p_{i,j}} + V\phi_{NL_{i,j}}.$$

Where, ϕ_p is the solution of Poissons equation with all boundary values set to a zero voltage. Then the boundary fields are produced by $V\phi_{NL}$, which is the solution of a normalised Laplace equation, with V being the voltage on the boundaries. It is then possible to solve equation 5.39 without the need for any iteration.

The solution of the above field equations on the electrode should result in electromagnetic waves propagating through the electrode. For parallel plate electrodes in vacuum, the solution is the well-known zero order Bessel function of the first kind for the vertical electric field intensity, see [89, 90] and references therein for more on this. By assuming that the voltage is uniform across the electrode, these effects will not be taken into account. Despite this, the assumption of a uniform voltage is a reasonable one to make. Since the nature of the PIC algorithm forces one to model relatively small chambers in which standing wave effects should be negligible except at unrealistly high frequencies.

5.5.2 Poissons Equation

The geometry of the device which is simulated is shown in figure 5.1. In order to solve Poissons equation we need to know what type of boundary conditions to apply on the equations. For our geometry and operating conditions we can solve Poissons equation. We assume that the grounded electrode is at a constant uniform voltage and for convenience chose it is voltage to be zero. This implies that we have a Dirichlet boundary condition on the grounded electrode. On the powered electrode we have a uniform voltage distribution. This implies that we may also use a Dirichlet boundary condition there. This is sufficient information in order to solve Poissons equation over the simulated area.

5.5.3 Boundary conditions on Electromagnetic equations

The boundary conditions for the Electromagnetic component of the field solver are significantly less complicated than the boundary conditions on Poissons equation. For the time integration of Maxwells equations we need only the boundary conditions on the tangential components of **E**, no additional boundary conditions are necessary [36]. These conditions are sufficient to obtain closure of the finite differenced Maxwell curl equations. With the Maxwell equations differenced in the interior as described in section 5.2, the fluxes of tangential components of **B** are conserved exactly; in addition, the magnetic flux through any surface is constant and equal to zero. An additional boundary condition may be applied on **B** if there is an externally applied magnetic field, although this is not necessary in order to close the system of equations and is not implemented here.

5.5.4 Particle Boundary Conditions

The boundary conditions for particles interacting with the surfaces are quite simple. All the particles that impact on the surfaces are assumed to be perfectly absorbed. These particles are then removed from the simulation and have no further effect. When a particle impacts on a surface a secondary particle can be emitted with a desired secondary emission coefficient. For the powered electrode it is necessary to take into account the surface charge density on that electrode. In order to do so we assume that the charge density is uniformly distributed throughout the electrode. It should be noted though, that in reality this may not be the case.

5.6 Discussion

We have presented the outline of a two dimensional electromagnetic particle-in-cell simulation. The implementation of this PIC is that of a semi-implicit scheme, that is the field equations are solved implicitly and the particle push is handled with an explicit algorithm. This has the effect of removing the Courant stability condition from the field equations without the complexity of developing a fully implicit scheme. This simulation method is suitable for the study of electromagnetic effects within capacitively coupled plasma devices.

CHAPTER 6

Two dimensional Effects in Plasma devices.

Within this chapter we present results which have been obtained from the two dimensional PIC code described in the previous chapter. While two dimensional electrostatic plasma simulations have been in existence for some time, see for example [87], to date, an electromagnetic PIC code has never been used to describe a device which has a geometry similar to that which is being employed here, as far as the author is aware. Within this chapter we simulate a two dimensional plasma discharge using both a two dimensional electrostatic PIC code and also a full electromagnetic variant. We then compare the results between the two simulation methods. We do this in order to asses the validity of simulating a plasma device, whose geometry is similar to that which is of interest here, through the use of Poissons equation only and not the full set of Maxwells equations, i.e. statics vs dynamics.

This chapter is divided into two sections, the first section involves a comparison between the two variants of the PIC code described in the previous chapter. The second section then involves simulating a plasma device at higher frequencies than the industrial standard of $13.56MHz$ to investigate the changes that occur to the profile of the radial plasma density. Within this chapter, all results are presented in the usual SI system of units.

6.1 Comparison between Electromagnetic and Electrostatic PIC codes.

In this section we attempt to ascertain the validity of simulating a plasma device through the use of Poissons equation only, rather that the full set of Maxwells equations for the electromagnetic fields. To do this we simulate a plasma under identical conditions by the two methods and compare the results, the precise conditions which are simulated are listed in the table.

As a consequence of the stability conditions (5.2) and (5.2), in particular the condition which states that the Debye length must be spatially resolved, we are forced to simulate a plasma device in which the electron density is relatively low ($\lesssim 10^{15}m^{-3}$). In principle, it is possible to simulate plasma devices in which the density is arbitrarily high, though to simulate a device in which the number of spatial cells are greater than 100 becomes prohibitively high in computational expense. As a consequence of this, we may be loosing some of the electro-dynamical effects; since for example, the skin effect is dependent of the electron density.

Quantity	Value
Electrode separation	$2cm$
Axial dimensions	$6cm$
Current	$30Am^{-2}$
Frequency	$27.12MHz$
Pressure	200 mTorr
Gas	Argon

Table 6.1: Conditions of Simulated Reactor.

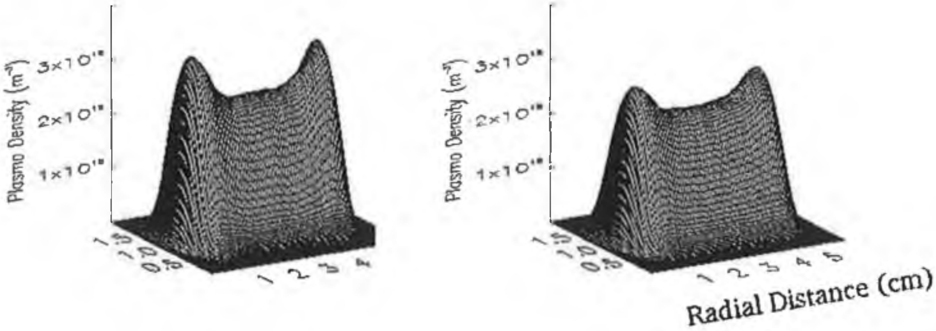

Figure 6.1: Comparison between time averaged plasma densities in the electrostatic (right) and electromagnetic (left) situations.

Plasma Density

In figure 6.1 we present three dimensional plots of the time averaged electron density for both the electrostatic and the electromagnetic situations. While the general density profile between the two situations is similar there are some immediately noticeable differences within the profile of the plasma density. It is found that under the conditions being simulated, that there exists peaks in the plasma density near the radial edge of the plasma. These peaks in the density are observed in both the electrostatic and electromagnetic situations, the peaks though are found to be more pronounced in the electromagnetic situation. This difference can be more readily seen in the cross section of the plasma density presented in figure 6.1.

The increase in the amplitude of these density peaks which is observed in the electromagnetic situation is believed to be as a result of a slight magnetic confinement which occurs as a result of a DC magnetic field within the simulated device. The nature of this magnetic field is described below. The precise nature of these peaks we shall discuss later also, since here we are only interested in describing the quantitive differences that exist between the simulation methods.

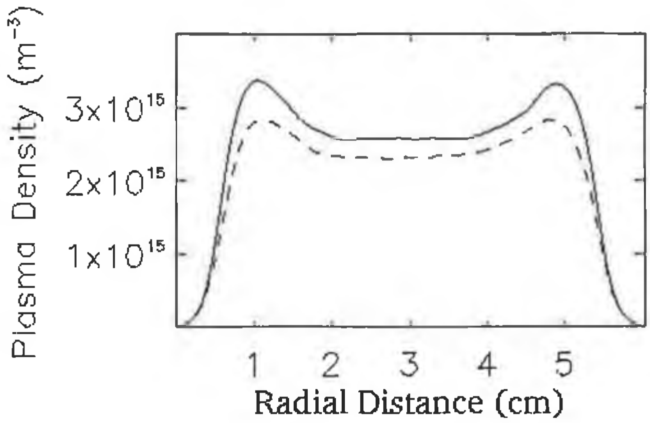

Figure 6.2: Time averaged electron density parallel to the electrode. Profile is taken through the centre of the discharge at $x = 1cm$. The solid line represents the electromagnetic situation, the dashed line the electrostatic result.

In figure 6.1 the cross section of the plasma density through the centre of the discharge. It is found that, as should be expected, the plasma is symmetric in the radial direction. Apart from the change in the density which is seen between the two simulation methods, there are no significant differences between the two. Finally in regard to the plasma density, in figure 6.1 we show a cross section of the plasma density in the direction perpendicular to the electrode, i.e along the discharge. For the density perpendicular to the electrode there is slight difference between the two profiles. The peak of the plasma density is displaced away from the centre of the discharge. Again there is no quantitive difference between the two simulation methods.

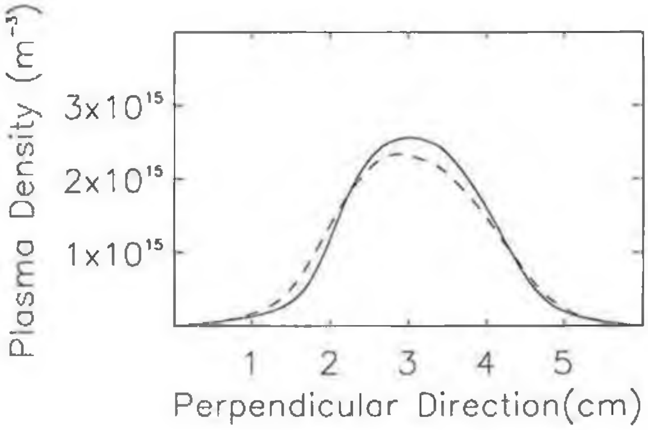

Figure 6.3: Time averaged electron density perpendicular to the electrode. The dashed line is the electrostatic situation and the solid line is the electromagnetic case.

Electromagnetic Fields.

In figure 6.1 we show the time averaged plasma potential profile within the simulated device. Only the profile for the electromagnetic situation is presented since visually they are almost indistinguishable. The dc bias on the powered electrode between the two simulation methods is different though. In the electrostatic situation, there develops a dc bias of approximately $-45V$, whereas for the electromagnetic situation there results in a -52 volt potential drop. This difference is believed to be related to the shift in the position of the maximum of the plasma density seen in figure 6.1. This is because the potential drop across the sheath is nothing other than the integral of the charge density within the sheath. A change in the charge density profile throughout the sheath will therefore result in a different potential drop.

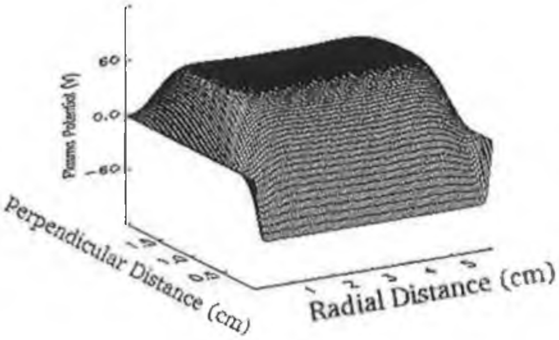

Figure 6.4: as a function of positionTime averaged plasma potential (V) as a function of position.

We then present in figures (6.1) and (6.1) a comparison between the perpendicular and parallel components of the electric field for both the electromagnetic and electrostatic situations. It is observed that the differences between the two situations are negligible. There is only a slight difference in the profile of the fields in the vicinity of the corners of the electrode. This is true for both components of the electric field.

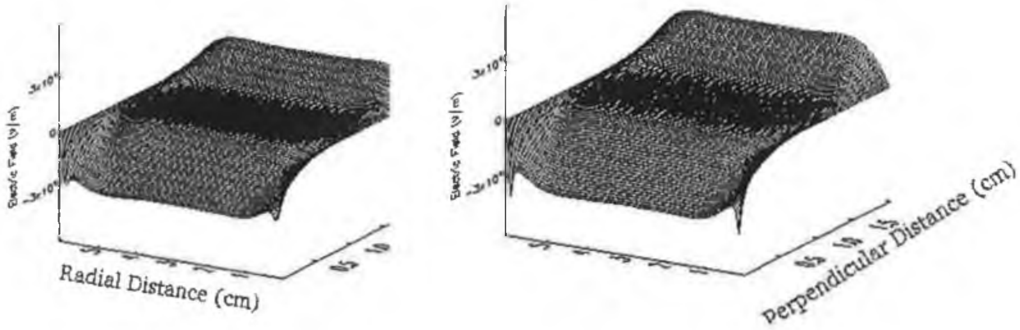

Figure 6.5: Electric Field profile Perpendicular to Electrode ($V\ m^{-1}$). Left and right diagrams are the electromagnetic and electrostatic diagrams respectively.

To enable the differences between the two simulation methods to become more evident, we have plotted cross sections of the electric field components in figures (6.1) and (6.1). Within these plots it is clearly shown that the electric field components are to a good approximation described by a solution of Poissons equation. The only noticeable difference is in the amplitude of the electric field components. It is believed that this difference in the field amplitude can be attributed to the difference in the plasma density, seen in figure 6.1.

We now come to the fundamental difference between the two simulation methods, the induced magnetic field. Shown in figure 6.1 is the magnetic induction perpendicular to the simulated plane. We observe that there exists a time averaged magnetic field throughout the device. This magnetic field is particularly strong in the vicinity of the edge of the electrode. While there

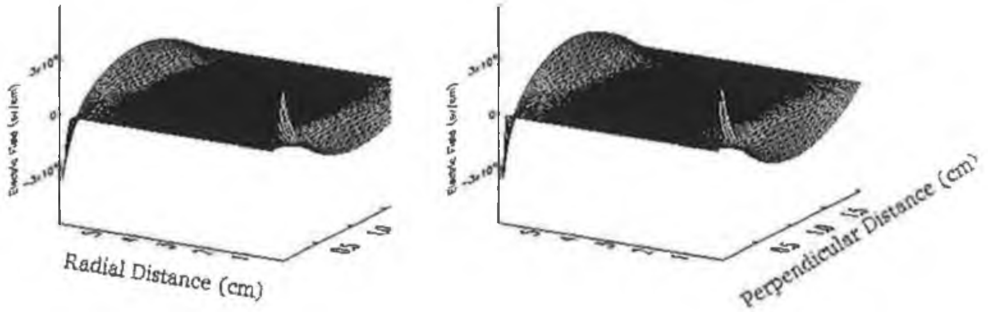

Figure 6.6: Electric Field profile parallel to Electrode ($V\ m^{-1}$). Left and right diagrams are the electromagnetic and electrostatic diagrams respectively.

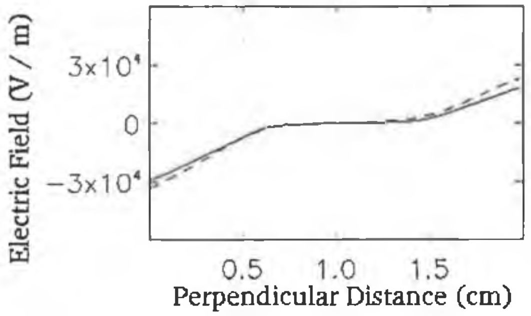

Figure 6.7: Electric Field profile perpendicular to Electrode ($V\ m^{-1}$). Solid line represents electromagnetic situation, dashed line electrostatic.

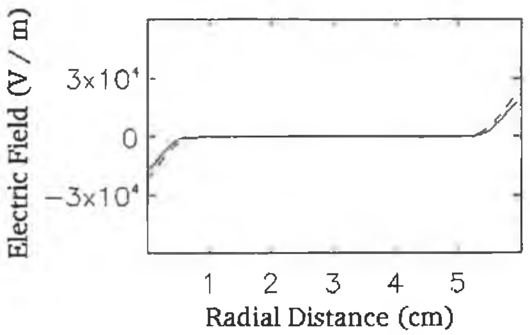

Figure 6.8: Electric Field profile parallel to Electrode ($V\ m^{-1}$). Solid line represents electromagnetic situation, dashed line electrostatic.

is a time averaged magnetic field throughout the plasma, this is consistent with Maxwells equations. For the time independent situation, Maxwells curl equation for the magnetic field reduces to Amperes law, written as

$$\nabla \times B = \frac{4\pi}{c} J$$

This can be transformed into a surface integral for the current density through a closed curve C, Amperes law can therefore be written in the form:

$$\oint_c B \cdot dl = \frac{4\pi}{c} I.$$

In the situation which we simulate here, we have a zero net dc current, since we operate the device with a sinusoidal rf current. This requirement for zero net dc current therefore reduces Amperes equation further into the following simple expression

$$\oint_c B \cdot dl = 0.$$

Under the conditions which are being simulated here, this equation states that the integral of the magnetic field over the surface of the chamber must

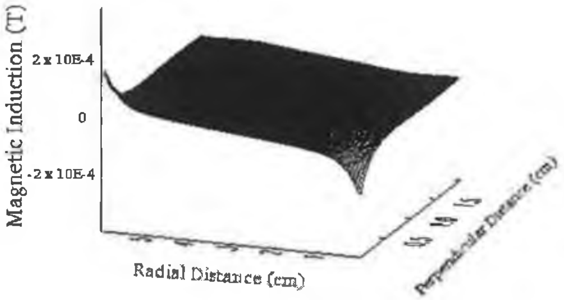

Figure 6.9: Time averaged magnetic field.

be zero, but not that the field at any point is zero; which is what is observed in figure 6.1.

The magnetic induction phase resolved on the electrode is then shown in figure 6.1. The magnetic field at the edge of the electrode is found to get comparatively strong. The precise reason for this magnetic field to be produced can be found from examining the following one of Maxwells equations,

$$\nabla \times E = -\frac{1}{c}\frac{\partial B}{\partial t},$$

in Cartesian coordinates for the system being modelled here, this is expanded as

$$\frac{\partial E_x}{\partial y} - \frac{\partial E_y}{\partial x} = -\frac{1}{c}\frac{\partial B_z}{\partial t}.$$

Because there will always be a much greater potential drop from the electrode to the grounded chamber wall in the direction parallel to the electrode than perpendicular to it. The absolute value of the terms on the left hand side of the above equation will always be different. Hence a non zero magnetic field will always be produced for the type of device which is being simulated here. This is the source of the observed magnetic field which is observed in figures (6.1) and (6.1).

Within experimental devices, the grounded chamber is usually a significantly greater distance away from the powered electrode than in the simulated chamber. Therefore, within most experimental reactors one should not expect this magnetic field to be as pronounced in the vicinity of the electrode edge.

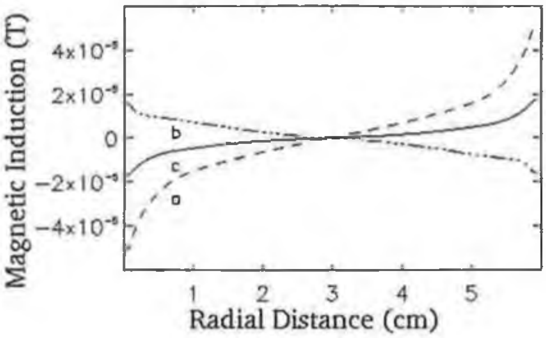

Figure 6.10: Instantaneous magnetic field on the electrode for three different times within the rf phase: times a, b and c represent a phase of $\phi = 0$, $\phi = \pi/2$ and $\phi = \phi$ respectively.

Distributions

In figure 6.1 is the electron energy distribution function for both the electrostatic and electromagnetic situations. The EEDF indicates that the average temperature of the electrons is approximately 3 eV. While both of the curves are quantitively similar there are some notable characteristics. Both of the curves can be approximated as a distribution with two species of electrons at different temperatures. The populations of electrons changes from hotter low energy electrons to that of a colder high energy electrons. This change in temperature occurs at approximately 13 eV. As can be seen in figure 5.4 this is the approximate energy of the inelastic scattering thresholds for electron-neutral collisions. The change in the temperature of the electrons which is observed at ≈ 13 eV can therefore be attributed to inelastic collision mechanisms. The temperatures of these two different species of electrons are slightly different in electromagnetic and electrostatic situations. In the electromagnetic situation, the low energy electrons are cooler and the high energy species electrons are hotter than the situation in the electrostatic situation.

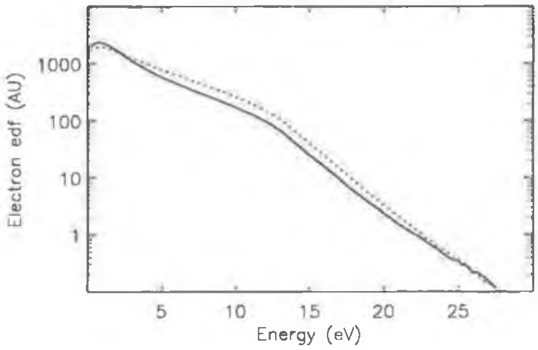

Figure 6.11: Time averaged electron distribution function for both electrostatic (dots) and electromagnetic algorithms (solid) .

Discussion

By comparing the graphs in the preceding section we find that there are no significant quantitive differences between the electrostatic and electromagnetic algorithms presented above under these conditions. This indicates that under the present conditions it is reasonable to model a plasma device through the solution of Poissons equation for the fields only. There is no obvious reason to implement the additional complexity of adding in magnetic effects resulting from Maxwells curl equations.

6.2 Plasma density Profile

The theme of this thesis is the study of plasma devices which are operated with two separate frequencies. One of these frequencies being significantly greater than the industrial standard of $13.56MHz$. Because of this it is of interest to investigate, and understand, the effect of operating a device with higher frequencies has on the plasma; specifically on the two dimensional structure of the plasma. The two dimensional structure of the plasma is particularly important since this determines the uniformity of the ion flux onto the electrode; hence affecting the uniformity of the ion etch rates on any semiconductor wafer placed on the electrode. The two dimensional structure of a plasma has been studied previously through the use of experimental optical techniques [1, 13, 14]. Kitajima et. al. found that the radial uniformity of the plasma density profile increased as the frequency was increased from the standard industrial frequency to much greater values.

We now present the radial profile of the electron plasma density from the two dimensional electromagnetic PIC code. In figure 6.2 we show the radial density profile for two frequencies, at the standard $13.56MHz$ and also at $81.36MHz$. We observe that the radial uniformity of the electron plasma density profile increases significantly as the operating frequency is increased. Whereas at lower frequencies there develops peaks in the plasma density near the edge of the plasma, at higher frequencies these peaks no longer appear; the radial density profile appears almost completely flat at the higher frequency.

In order to understand the mechanism which results in a greater uniformity in the plasma density, we must first explain the creation of the peaks in the density. Within capacitively coupled plasma devices it is well known that the ionization rate is at it's maximum in the vicinity of the plasma sheath

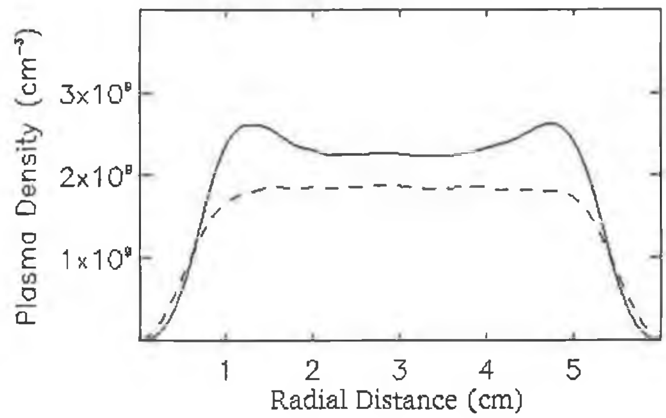

Figure 6.12: Radial electron density for two operating frequencies, 13.56Mhz (solid) and 81.36Mhz (dashed) all other parameters as in table (6.1).

[34, 35]. This maximum in the ionization is due to the fast electrons accelerated by the sheath as it expands away from the boundary [42, 45, 85, 91]. It is this maximum in the ionization rate near the sheath that is believed responsible for the peaks in the plasma density which are observed. Under the geometry that is being simulated here there is a sheath on each side of the chamber; this is a situation which usually does not occur in experimental devices. This has the result that near the radial edge of the plasma there are two plasma sheaths. This leads to the ordinary peak in the ionization rate near the electrodes being increased by almost a factor of two at the radial edge. The effect is particularly strong in the device simulated here as a result of the proximity of the powered and grounded electrode. Since this results in the field being unusually strong in the radial direction. To illustrate this we present the time averaged ionization rate within the simulated device in figure 6.2. We observe that there are substantial peaks in the ionization rate near the radial edge of the plasma, which creates the peaks in the plasma

density.

This increase in the plasma density near the radial edge of the plasma is believed to be only possible when one operates a device at relatively high gas pressures. As the pressure is increased both the ion mobility and the ion diffusion constants decrease, resulting in the plasma being almost confined at the radial edge. At lower pressures the plasma is more free to diffusion into the centre of the chamber. Thereby resulting in a greater uniformity of the plasma at low pressures.

Kitajima et. al [14] have taken, experimentally, two dimensional images of a plasma discharge using optical diagnostics in which the net excitation rate was measured. Within these experimentally obtained images, there were observed peaks in the net excitation rate near the radial edge of the plasma at lower frequencies, reproduced in figure 6.2. We believe that the peaks in the plasma density which are observed in the above graphs correspond to the same phenomena which was observed in the experiment of [14]. The peaks which were observed by Kitajima et. al. were not as pronounced as those which are observed in the simulation though. This is not believed to be particularly surprising though, since in the experiment there was effectively no sheath in the radial direction. In the experiment there was a $50cm$ gap between the electrode and the grounded chamber; there was though a grounded shield surrounding the powered electrode which may have caused the peak in the excitation rate observed. The majority of the electrons that were produced as a result of this peak in the ionization were therefore free to diffuse away from the plasma to the chamber wall in the radial direction in the experiment. Whereas, in the simulation the majority of the electrons are confined within the plasma as a result of the plasma sheath at the radial edge. Only the most energetic electrons are free to escape to the wall.

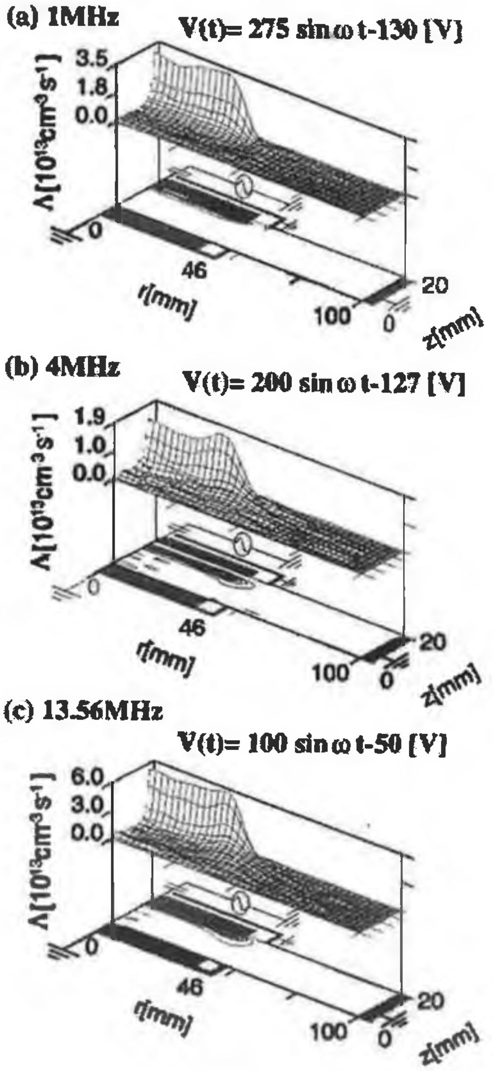

Figure 6.13: Time averaged 2D profile of the net excitation rate of Ar($3p_5$) for 1.0 Torr and 8 W at various operating frequencies, diagram taken from [1]

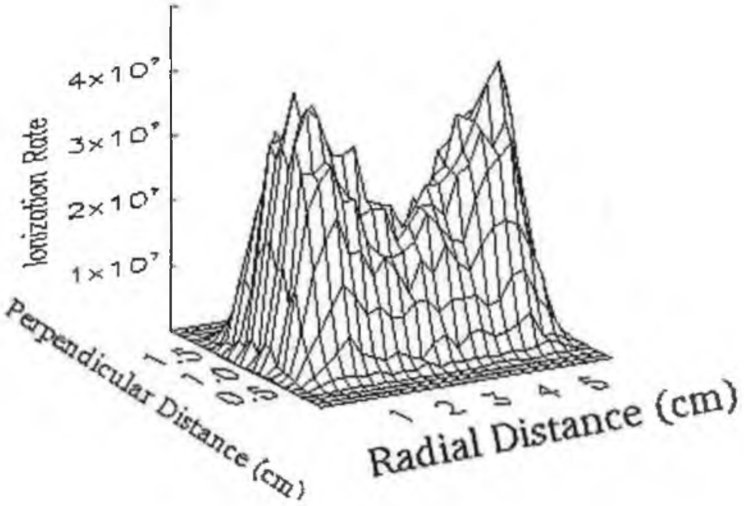

Figure 6.14: Time averaged ionization rate as a function of spatial dimensions.

The increase in the uniformity can therefore be explained as follows. As the frequency is increased, the width of the sheath and the sheath potential decrease considerably. In the case of the lower frequency, the sheath width is comparable to, or even greater than, the distance between the edge of the rf electrode and the outer grounded chamber. This results in the electric field diverging strongly in the radial direction, see figure 6.1. The sheath width may be greater in the perpendicular direction than in the radial direction. This divergence of the electric field also depends on the magnitude of the dc voltage on the electrode. Since the voltage decreases as the frequency is increased, the inductive electric field becomes weaker in the radial direction. This has the effect of reducing the ionization rate near the radial edge of the plasma. With the radial density profile becoming flatter as a result.

Thus, at higher pressures it can be expected that there will be a peak in the ionization rate near the radial edge of the plasma when ever the field in the radial direction is comparable to, or greater that the electric field in the perpendicular direction. This means that the effect will be strongly dependent on the geometry of the device. The peak in the density will occur regardless of the operating conditions, provided that the pressure and voltage are high enough for a given geometry.

CHAPTER 7

Conclusions

The results presented in this thesis demonstrate, that the energy and flux of the ions bombarding the electrode surface can be controlled independently within a limited range of parameter space. There are two regimes in which it is possible to achieve this. For large electrode separations, in which the increase in the sheath width is small compared to the electrode separation, the ion current can be controlled by varying the total discharge current. In practice though, it is extremely difficult to create a current source with the desired properties within a real physical device. At smaller electrode separations, the ion current may be controlled by the use of a constant high frequency power source. The precise reason why a high frequency power maintains a constant ion current is uncertain, since the plasma density decreases under these conditions, although the increasing electron temperature is believed to play an important role. It should be noted that the use of two distinct frequencies will not in general provide independent control of the ion current and energy; it is only within a restricted area of parameter space that this independence is realised. In general, it is *not* possible to obtain the desired independence of ion energy and flux onto the substrates within these reactors.

Within dual frequency discharges the structure of the IDF at the electrodes is substantially modified. The IDF resembles a single peak centred at V_{hf} when $V_{lf} = 0$, since the operating frequency is greater than the ion plasma frequency. As the low frequency voltage is increased the IDF changes and takes on the distinctive bimodal structure which is well known in single frequency devices.

If the ratio of the high and low frequencies is sufficiently large, the simulations indicate that a limited independents of the control of the ion energy and flux is possible by manipulation of the externally controllable power sources. The system appears to maintain its decoupled nature, under conditions simulated here, for values of $\omega_{lf}/\omega_{hf} \lessapprox 0.1$. When operating dual frequency devices at higher voltages than those being simulated here, it may be necessary to use a greater ratio of the operating frequencies in order for the device to maintain it is decoupled nature.

A consequence of the use of a second, low frequency, is that the sheath width increases. This results in the width of the bulk plasma being reduced thereby increasing the electron temperature. This will have considerable consequences for the plasma chemistry of a device operated with two separate frequencies. Although this only occurs when the change in the sheath width is comparable to the plasma extent. When operating a device with a reasonably large electrode separation this increase in the sheath width will not be a major concern; meaning that the electron temperature will not change significantly.

We have then developed a sheath model for the case where the electrode is driven with two separate current sources at different frequencies. The model has been derived under the approximations that the hf electric field is much smaller than the lf counterpart. We have obtained important sheath parameters such as the instantaneous electron sheath motion and sheath potential. The analytical results have been compared to PIC simulations results. Where we have found good quantitative and qualitative agreement between the two approaches. In particular, both numerical and analytical models predict an increase in the hf component of the electron sheath edge motion in the vicinity of the electrode. The model predicts also, the frequency ratio and current ration dependence of both the sheath width and sheath potential. An important point predicted by the model, and confirmed by the PIC-MCC results, is that although the hf field is much smaller the lf field in typical dual frequency operating regime, the hf field significantly modifies the sheath parameters such as the sheath width and the dc sheath voltage drop.

A dual frequency sheath model was then developed to investigate the sheath within the intermediate pressure regime. This model has been then compared to a previously developed dual frequency sheath model, which is valid in the collisionless regime, finding as expected, significant deviation between the two models. The deviations between the two models are particularly evident at larger pressures ($\gtrsim 20mTorr$).

A two dimensional PIC code was then developed and used to investigate the two dimensional profile of the plasma density within capacitively coupled devices. Using this simulation method we discovered an anomalous profile of the plasma density at low frequencies and relatively high pressures. There develops peaks in the plasma density near the radial edge of the plasma.

These peaks in the plasma density result form the particular geometry which was simulated, in which the grounded chamber is close to the powered electrode. This results in a strong field being produced in the radial direction, which does not usually exist in an experimental apparatus.

Bibliography

[1] T. Kitajima, Y. Takeo, and T. Makabe. Effects of frequency on the two-dimensional structure of capacitively couples plasma in ar. *J. Appl. Phys.*, 84(11):5928–5936, Dec 1998.

[2] D. M. Manos and D. L. Flamm. *Plasma Etching, An introduction.* Academic Press, San Diego, CA, 1988.

[3] T. Tatsumi, M. Matsui, M. Okigawa, and M. Sekine. Control of surface reactions in high-performances sio_2 etching. *J. Vac. Sci. Technol. B*, 18 (4):1897–1902, July 2000.

[4] Lewi Tonks and Irving Langmuir. A general theory of the plasma of an arc. *Phys. Rev.*, 34:876–922, September 1929.

[5] J. J. Thompson. The electrodeless discharge through gases. *Phil. Mag.*, 4:1128–1160, 1927.

[6] Irving Langmuir. The interaction of electron and positive ion space charges in cathode sheaths. *Phys. Rev.*, 33:954–989, June 1929.

[7] H-B. Valentini and E. Glauche. Sheath formation in low pressure discharges. *Plasma Sources Sci. Technol.*, 9:574–582, 2000.

[8] W. J. Goedheer. Lecture notes on radio-frequency discharges, dc potentials, ion and electron energy distributions. *Plasma Sources Sci. Technol.*, 9(4):507–516, November 2000.

[9] G. Gozadinos. *Collisionless heating and particle dynamics in radio-frequency capacitive plasma sheaths.* Dublin City University, 2001.

[10] Michael A. Lieberman and Allan J. Lichtenberg. *Principles of Plasma Discharges and Materials Processing.* Wiley, New York, 1994.

[11] Brian Chapman. *Glow Discharge Processes.* Wiley, New York, 1980.

[12] L. Martinu, Klemberg-Sapieha J, E, O.M. Kuttel, A. Raveh, and M. R. Wertheimer. Critical ion energy and ion flux in the growth of films by plasma-enhanced chemical-vapor deposition. *J. Vac. Sci. Technol. A*, 12(4):1360–1364, July 1994.

[13] T. Kitajima, Y. Takeo, Z. Lj. Petrovic, and T. Makabe. Functional separation of biasing and sustaining voltages in two-frequency capacitively coupled plasma. *Appl. Phys. Lett.*, 77(4):489–491, July 2000.

[14] T. Kitajima, Y. Takeo, and T. Makabe. Two-dimensional ct images of two-frequency capacitively coupled plasma. *J. Vac. Sci. Technol. A*, 17 (5):2510–2516, September 1999.

[15] Haruhiro H. Goto, Hans-Dirk Lowe, and Tadahiro Ohmi. Dual excitation reactive ion etcher for low energy plasma processing. *J. Vac. Sci. Technol. A*, 10(5):3048–3054, September 1992.

[16] J. Robiche and P. C. Boyle et. al. Analytical model of a dual frequency capacitive sheath. *J. Phys. D: Appl. Phys.*, 36(15), August 2003.

[17] P. C. Boyle et. al. Independent control of ion current and ion impact energy onto electrodes in dual frequency plasma devices. *J. Phys. D: Appl. Phys.*, 37(5):697–701, February 2004.

[18] H. C. Kim and V. I. Manosiouthakis. Dually driven radio frequency plasma simulation with a three moment model. *J. Vac. Sci. Technol. A*, 16(4):2162–2172, July 1998.

[19] H. H. Goto, H. D. Lowe, and T. Ohmi. Independent control of ion density and ion bombardment energy in a dual rf excitation plasma. *IEEE Trans. Semi. Man.*, 6(1):58–64, February 1993.

[20] T. Denda, U. Miyoshi, U. Komukai, T. Goto, Z. Lj. Petrovic, and T. Makabe. Functional separation in two frequency operation of an inductively coupled plasma. *J. Appl. Phys.*, 95(3):870–876, 2004.

[21] D. Bohm. Minimum ionic kinetic energy for a stable sheath. In A. Guthry and R. K. Wakerling, editors, *The Characteristics of Electrical Discharges in Magnetic Fields*, chapter 3, pages 77–86. MacGraw-Hill, New York, 1949.

[22] K-U Riemann. The bohm criterion and sheath formation. *J. Phys. D: Appl. Phys.*, 24:493–518, 1991.

[23] R. N. Franklin. What significance does the bohm criterion have in an active collisional plasma-sheath. *J. Phys. D: Appl. Phys.*, 35:2270–2273, September 2002.

[24] R. N. Franklin. The plasma-sheath transition with a constant mean freee path model and the applicability of the bohm criterion. *Phys. Plasmas*, 8(2):643–647, February 2001.

[25] M. Surendra and D. B. Graves. Capacitively coupled glow discharges at frequencies above $13.56 mhz$. *Appl. Phys. Lett.*, 59(17):2091–2093, May 1991.

[26] M. J. Colgan, M. Meyyappan, and D. E. Murnick. Very high-frequency capacitively coupled argon discharges. *Plasma Sources Sci. Technol.*, 3: 181–189, 1994.

[27] E. Amanatides and D. Mataras. Frequency variation under constant power conditions in hydrogen radio frequency discharges. *J. Appl. Phys.*, 89(3):1556–1566, Feb 2001.

[28] T. Novikova, B.Kalache, P. Bulkin, K. Hassouni, W. Morscheidt, and P. Roca I Cabarrocas. Numerical modeling of capacitively coupled hydrogen plasmas: Effects of frequency and pressure. *J. Appl. Phys.*, 93 (6):3198–3206, March 2003.

[29] T. Kitamura, N. Nakano, T. Makabe, and Y. Yamaguchi. A computational investigation of the rf plasma sturctures and their production efficiency in the frequency range from hf to vhf. *Plasma Sources Sci. Technol.*, 2(1):40–45, August 1999.

[30] V. A. Godyak, R. B. Piejak, and B. M. Alexandrovich. Electrical characteristics of parallel-plate rf discharges in argon. *IEEE Trans. Plasma Sci.*, 42(4):2299–2312, August 1990.

[31] Hans-Dirk Lowe, Haruhiro, and Tadahiro Ohmi. Control of ion energy

and flux in a dual frequency excitation magnetron sputtering discharge. *J. Vac. Sci. Technol. A*, 9(6):3090–3099, November 1991.

[32] U. Kortshagen, C. Busch, and L. D. Tsendi. On simplifying approaches to the solution of the boltzmann equation in spatially inhomogeneous plasmas. *Plasma Sources Sci. Technol.*, 5(1):1–17, 1996.

[33] A. Santos and M. H. Ernst. Esact stedy-state solution of the boltzmann equation: A driven one-dimensional inelastic mazwell gas. *Phy. Rev. E*, 68:011305, July 2003.

[34] M. Surendra and D. B. Graves. Particle simulations of radio-frequency glow discharges. *IEEE Trans. Plasma Sci.*, 19(2):144–157, April 1991.

[35] David Vender and Rod W. Boswell. Numerical modeling of low-pressure rf plasmas. *IEEE Trans. Plasma Sci.*, 18(4):725–732, August 1990.

[36] C. K. Birdsall and A. B. Langdon. *Plasma Physics via Computer Simulation*. Adam Hilger, Bristol, 1991.

[37] C. K. Birdsall. Particle-in-cell charged-particle simulations, plus Monte Carlo collisions with neutral atoms, PIC-MCC. *IEEE Trans. Plasma Sci.*, 19(2):65–85, April 1991.

[38] M. J. Kushner. Monty carlo simulation of electron properties in rf parallel plate capacitive discharges. *J. Appl. Phys.*, 45(9):4958–4965, 1983.

[39] Charles K. Birdsall, Emi Kawamura, and Vahid Vahedi. Particle simulation methods for glow discharges: Past, present, and future, with applications. In U. Kortshagen and L. D. Tsendin, editors, *Electron kinetics and applications of glow discharges*, New York, 1998. Plenum Press.

[40] P. Benoit-Cattin and L. Bernard. Anomalies of the energy of positive ions extracted from high-frequency ion sources, a theoretical study. *J. Appl. Phys.*, 39(12):5723–5727, November 1968.

[41] P. C. Boyle et. al. Electrostatic modelling of dual frequency rf plasma discharges. *Plasma Sources Sci. Technol.*, 13(3), August 2004.

[42] G. Gozadinos, M. M. Turner, and D. Vender. Collisionless electron heating by capacitive rf sheaths. *Phys. Rev. Lett.*, 87(13):135004, September 2001.

[43] M. M. Turner. Pressure heating of electrons in capacitively-coupled rf discharges. *Phys. Rev. Lett.*, 75(7):1312–1315, August 1995.

[44] V. A. Godyak. Statistical heating of electrons at an oscillating plasma boundary. *Sov. Phys. - Tech. Phys.*, 16(7):1073–1076, January 1972.

[45] M. A. Lieberman and S. E. Savas. Bias voltage in finite length, cylindrical and coazial radio-frequency discharges. *J. Vac. Sci. Technol. A*, 8(3):1632–1641, May 1989.

[46] M. V. Alves, M. A. Lieberman, and C. K. Birdsall. Sheath voltage ratio for asymmetric rf discharges. *J. Appl. Phys.*, 69(7):3823–3829, Apr 1991.

[47] P. M. Meijer and W. J. Goedheer. Calculation of the auto-bias voltage for rf frequencies well above thio ion-plasma frequency. *IEEE Trans. Plasma Sci.*, 19(2):170–175, April 1997.

[48] M. A. Lieberman. Spherical shell model of an asymmetric rf discharge. *J. Appl. Phys.*, 65(11):4186–4191, June 1989.

[49] Valery A. Godyak. *Soviet Radio Frequency Discharge Research*. Delphic Associates, Falls Church, VA, 1986.

[50] E. Kawamura, V. Vahedi, M. A. Lieberman, and C. K. Birdsall. Ion energy distributions in rf sheaths; review, analysis and simulation. *Plasma Sources Sci. Technol.*, 8(2):R45–R64, August 1999.

[51] K. Kohler, J. W. Coburn, D. E. Horne, and E. Kay. Plasma potentials of 13.56-mhz rf argon glow discharges in a planar system. *J. Appl. Phys.*, 57(1):59–66, January 1985.

[52] P. Reinke, S. Bureau, J.E. Klemberg-Sapieha, and L.Martinu. Ion energy distributions in dual- and single-mode microwave/ radio-frequency plasma. *J. Appl. Phys.*, 78(8):4855–4858, October 1995.

[53] A. Hallil, O. Zabeida, M. R. Wertheimer, and L. Martinu. Mass-resolved ion energy distributions in continuous dual mode microwave/radio frequency plasmas in argon and nitrogen. *J. Vac. Sci. Technol. A*, 18(3): 882–890, May 2000.

[54] K-U Riemann, U. Ehlemann, and K. Wiesemann. The ion energy distribution function in front of a negative wall. *J. Phys. D: Appl. Phys.*, 25:620–633, 1992.

[55] U. Flender and K. Wiesemann. Ion distribution function behind an rf sheath. *J. Phys. D: Appl. Phys.*, 27:509–521, 1994.

[56] J. Liu, G.L. Huppert, and H.H. Sawin. Ion bombardment in rf plasmas. *J. Phys. A: Math. Gen.*, 68(8):3916–3934, October 1990.

[57] J.K. Olthoff and R.J. Van Brunt. Ion kinetic-energy distributions in argon rf glow discharges. *J. Appl. Phys.*, 72(10):4566–4574, November 1992.

[58] M. A. Lieberman, J.P. Booth, P. Chabert, J. M. Rax, and M. M. Turner. Standing wave and skin effects in large-area, high-frequency capacitive discharges. *Plasma Sources Sci. Technol.*, 11(3):283–293, August 2002.

[59] P. C. Boyle et. al. Global model of dual frequency plasma discharges. *ICPIG Procedings*, 2003.

[60] M. A. Lieberman. Analytical solution for capacitive rf sheath. *IEEE Trans. Plasma Sci.*, 16(6):638–644, December 1988.

[61] V. A. Godyak and N. Sternberg. Dynamic model of the electrode sheaths in symmetrically driven rf discharges. *Phy. Rev. A*, 42(4):3455–3460, March 1991.

[62] P. A. Miller and M. E. Riley. Dynamics of collisionless rf plasma sheaths. *J. Appl. Phys.*, 82(8):3689–3709, October 1997.

[63] T. Panagopoulous and D. J. Economou. Plasma sheath model and ion energy distribution for all radio frequencies. *J. Appl. Phys.*, 85(7):3435–3443, 1999.

[64] F. R. Myers and T. S. Cale. A dual frequency plasma sheath model. *J. Electrochem. Soc.*, 139(12):3587–3595, December 1992.

[65] J. Gierling and K-U Riemann. Comparison of a consistent theory of radio frequency sheaths with step models. *J. Appl. Phys.*, 83(7):3521–3528, 1998.

[66] J. E. Allen and M. A. Skorik. The Bohm criterion in the presence of radio-frequency fields. *J. Plasma Physics*, 50(2):243–249, 1993.

[67] R. N. Franklin. The dual frequency radio-frequency sheath revisited. *J. Phys. D: Appl. Phys.*, 36(21):2660–2661, November 2003.

[68] P. C. Boyle, J. Robiche, and M.M Turner. Modelling of a dual frequency capacitive sheath in the low and intermediate pressure regimes. *J. Phys. D: Appl. Phys.*, 37:1451–1458, April 2004.

[69] Rayzer Y. P. *Gas Discharge Physics.* Springer-Verlag, 1987.

[70] M. A. Lieberman. Dynamics of a collisional, capacitive rf sheath. *IEEE Trans. Plasma Sci.*, 17(2):338–341, December 1988.

[71] Smirnov B. M. *Physics of ionised gases.* Wiley, New York, 2001.

[72] A. Hornbeck J. *Phys. Rev.*, 4(84):615–620, 1951.

[73] Boeuf J. P. and Pichforf L. C. *Phy. Rev. E*, 51:1376, 1951.

[74] A. Perret, P. Chabert, J. P. Booth, J. Jolly, J. Guillon, and Ph. Auvray. Ion flux nonuniformities in large-area high-frequency capacitive discharges. *Appl. Phys. Lett.*, 83(2):243–245, July 2003.

[75] L. A. Hageman and D. M. Young. *Applied Iterative Methods.* Academic Press, London, 1981.

[76] R. W. Hockney and J. W. Eastwood. *Computer Simulation using Particles.* MacGraw-Hill, New York, 1981.

[77] K. J. Bowers. *High Frequency Electron Resonances and Surface Waves in Unmagnitized Bounded Plasmas.* University of California, Berkeley, 2001.

[78] W. H. Press, S. A. Teukolsky, and W. T. Vetterling. *Numerical Recipes in C.* Cambridge University Press, New York, 1992.

[79] J. P. Boris. The acceleration calculation from a scalar potential. *Plasma Physics Laboratory, Princeton University MATT-152*, March 1970.

[80] O. Buneman. Time reversible difference procedures. *J. Comp. Phys.*, 1 (67):517–535, June 1967.

[81] J. P. Boris. Relativistic plasma simulation-optimization of a hybrid code. *Proc. Fourth Conf. Num. Sim. Plasma.*, 3(67), November 1970.

[82] J. L. Pack, R. E. Voshall, A. V. Phelps, and L. E. Kline. Longitudinal electron diffusion coefficients in gases: Noble gases. *J. Appl. Phys.*, 71 (11):5363–5371, June 1992.

[83] A. V. Phelps. *J. Chem. Phys. Ref. Data*, 20(3):557–573, 1991.

[84] A. V. Phelps. The application of scattering cross sections to ion flux models in discharge sheaths. *J. Appl. Phys.*, 76(2):747–753, February 1994.

[85] M. Surendra, D. B. Graves, and I. J. Morey. Electron heating in low pressure rf glow discharges. *Appl. Phys. Lett.*, 56(12):1022–1024, March 1990.

[86] T. Simko, V. Martisovits, J. Bretagne, and G. Gousset. Computer simulations of h^+ and h_3^+ transport parameters in hydrogen drift tubes. *Phy. Rev. E*, 56(5):5908, 1997.

[87] Vahid Vahedi and G. DiPeso. Simultaneous potential and circuit solution for two-dimensional bounded plasa simulation codes. *J. Comp. Phys.*, 131:149–163, 1997.

[88] J. P. Verboncoeur, M. V. Alves, V. Vahedi, and C. K. Birdsall. Simultaneous potential and circuit solution for 1d bounded plasma particle simulation codes. *J. Comp. Phys.*, 104:321–328, 1993.

[89] L. Sansonnens, A. Pletzer, D. Magni, A. A. Howling, Ch. Hollenstein, and J. P. M. Schmitt. A voltage uniformity study in large-area reactors for rf plasma deposition. *Plasma Sources Sci. Technol.*, 6(2):170–178, 1997.

[90] L. Sansonnens and J. Schmitt. Shaped electrode and lens for a uniform radio-frequency capacitive plasma. *Appl. Phys. Lett.*, 82(2):1831–1834, January 2003.

[91] G. Gozadinos, D. Vender, M. M. Turner, and M. A. Lieberman. Collisionless electron heating by capacitive radio-frequency plasma sheaths. *Plasma Sources Sci. Technol.*, 10(2):117–124, May 2001.